ELASTOHYDRODYNAMIC MODEL OF RECIPROCATING HYDRAULIC ROD SEALS

A Ph.D. Dissertation
Presented to
The Academic Faculty

by

Bo Yang

In Partial Fulfillment
of the Requirements for the Degree
Doctor of Philosophy in the
George W. Woodruff School of Mechanical Engineering

Georgia Institute of Technology
August, 2010

ELASTOHYDRODYNAMIC MODEL OF RECIPROCATING HYDRAULIC ROD SEALS

Approved by:

Dr. Richard F. Salant, Advisor
School of Mechanical Engineering
Georgia Institute of Technology

Dr. Laurence J. Jacobs
School of Civil & Environmental Engineering
Georgia Institute of Technology

Dr. Marc K. Smith
School of Mechanical Engineering
Georgia Institute of Technology

Dr. Jeffrey L. Streator
School of Mechanical Engineering
Georgia Institute of Technology

Dr. Gerhard Poll

University of Hannover, Germany

Date Approved: April 15, 2010

I dedicate this work to my parents,
YANG Hongyi and YANG Yingmin.
Without their endless love and support,
the completion of this work would not have been possible.

ACKNOWLEDGEMENTS

I would like to express my sincere appreciation to my advisor, Dr. Richard F. Salant, for his guidance and support throughout my graduate study. I thank Dr Salant's kindness, trust and patience; his devotion to research will be the model for me to follow in my whole life. I also would like to thank my thesis committee for their valuable suggestions and help. I would like to acknowledge my colleague Azam Thatte for his help in my research. I thank my parents for their support and guidance through my growth. Finally, I wish to acknowledge the financial support from the National Science Foundation and the Fluid Power Industry through the NSF Engineering Research Center for Compact and Efficient Fluid Power.

TABLE OF CONTENTS

LIST OF TABLES

Page

LIST OF FIGURES

Page

NOMENCLATURE

d	separation of the contacting surfaces
E	elastic modulus
F	cavitation index
f	friction coefficient
$f(\delta)$	probability density function of surface heights
H	dimensionless average film thickness, h/σ
H_s	static undeformed film thickness, h_s/σ
H_T	dimensionless average truncated film thickness, h_T/σ
I_1	influence coefficient for normal (radial) deformation
L	length of solution domain in x-direction
P	dimensionless pressure, p/p_a
p_a	ambient pressure
P_c	contact pressure
p_{sealed}	dimensionless sealed pressured, p_{sealed}/p_a
$\hat{q}$	dimensionless flow rate per unit circumferential length, $12\mu_0 qL/[(p_a)\sigma^3]$
R	asperity radius
U	surface speed of rod
$\hat{x}$	dimensionless axial coordinate, x/L
$\hat{\alpha}$	dimensionless pressure-viscosity coefficient, αp_a
ϕ	fluid pressure/density function
$\phi_f, \phi_{fss}, \phi_{fpp}$	shear stress factors
$\phi_{s.c.x}$	shear flow factor

ϕ_{xx}	pressure flow factor
μ_0	viscosity at atmospheric pressure
$\hat{\rho}$	dimensionless density, ρ / ρ_l
ρ_l	liquid density
$\hat{\sigma}$	dimensionless rms roughness of sealing element surface, $\sigma R^{1/3} \eta^{2/3}$
$\hat{\tau}_{avg}$	average dimensionless viscous shear stress in the x-direction, τ_{avg} / E
$\hat{\tau}_c$	dimensionless shear stress due to contacting asperities, τ_c / E
$[\hat{\tau}_{avg}]_t$	total shear stress, $\hat{\tau}_{avg} + \hat{\tau}_c$
υ	Poisson's ratio
ξ	$R^{1/3} \eta^{2/3} EL / p_a$
ζ	dimensionless rod speed, $(\mu_0 UL)/[(p_a)\sigma^2]$
η	asperity density

SUMMARY

Reciprocating rod seals are widely used in hydraulic systems to prevent the hydraulic fluid from leaking into and polluting the environment. In this research an elastohydrodynamic model of a generalized reciprocating hydraulic rod seal, including mixed lubrication and surface roughness, has been successfully developed. This model consists of coupled fluid mechanics, contact mechanics, thermal analysis and deformation analyses.

Such model is capable of predicting the key seal performance characteristics, especially net leakage and friction force. This allows evaluation of potential seal designs and serves as design tools. Also as this model has been developed, the basic physics of seal operation has been clarified, which stimulates the development of innovative seal concepts, such as seals with engineered sealing surfaces.

The results of this study indicate that in general, hydraulic rod seals operate in the mixed lubrication regime, although under certain conditions full film lubrication may occur over a portion of the sealing zone. The roughness of the seal surface and the rod speeds play important roles in determining whether or not a seal will leak. Cavitation during the outstroke and partial full film lubrication during the instroke tend to prevent net leakage. The behavior of a reciprocating hydraulic rod seal with a double lip or two seals in tandem arrangement can be very different from that of a similar seal with a single lip. For the double lip seal, the secondary lip can strongly affect the behavior of the primary lip by producing an elevated pressure in the interlip region. The same seal

characteristics that promote effective sealing in a single lip seal and, in addition structural decoupling of multiple lips, are found to promote effective sealing in a multiple lip seal.

The model is validated through comparisons of model predictions with experimental measurements and observations by industry partners. The results have shown the predicted leakage and friction force for various seal and operation conditions are consistent with the measurements.

A seal with micro-pattern on the sealing surface also has been investigated. The results indicate that an elaborately designed pattern can improve the sealing characteristics of the seal, without significantly affecting the friction force.

In the end, the selection of the rod seal for a specific application using this analytical model is demonstrated. The best design can be picked up before a prototype being built.

CHAPTER 1

INTRODUCTION

1.1 Problem Description

A serious potential problem in hydraulic systems is the leakage of hydraulic fluid from the cylinders past the reciprocating rod seals. Not only can this leakage affect the system performance but, more importantly, it can lead to environmental pollution since such leakage directly enters the natural surroundings. Thus, the rod seal is one of the most critical components in hydraulic systems.

At the present time, although much has been learned about such seals from experimental studies, their basic behavior is still poorly understood. Consequently, the seal designer has virtually no analytical tools, beyond finite element structural analysis [1]-[4], with which to predict the behavior of potential seal designs or interpret test results. Neither does he/she have a conceptual framework upon which to base a design. Thus, current seal design is almost completely an empirical process.

1.2 Objective of the Research

The objective of this research is the development of a numerical model of a generalized reciprocating hydraulic rod seal, including mixed lubrication and surface roughness. Such a model would be capable of predicting the key seal performance characteristics, such as leakage and friction.

A successful numerical rod seal model would allow evaluation of potential seal designs before any hardware is built. It could therefore be used to screen potential designs and select only the most promising ones to be prototyped and tested. As testing proceeds, it could be used to guide the test program by determining the strategy for making design modifications.

In addition, such a seal model would stimulate the development of innovative seal concepts, such as seals with engineered sealing surfaces. Through development of the model, the basic physics of seal operation would become clarified, leading to new ideas for more effective sealing. These concepts can then be explored through simulations, using the model.

A sketch of a typical hydraulic rod seal is shown in Figure 1.1. The region where the seal lip appears to meet the rod is termed the sealing zone; it is where the sealing action takes place. Figure 1.2 shows how the sealing zone has been represented by most previous models: the surfaces of the rod and seal are assumed perfectly smooth and completely separated by a continuous film of hydraulic fluid, i.e. full film lubrication.

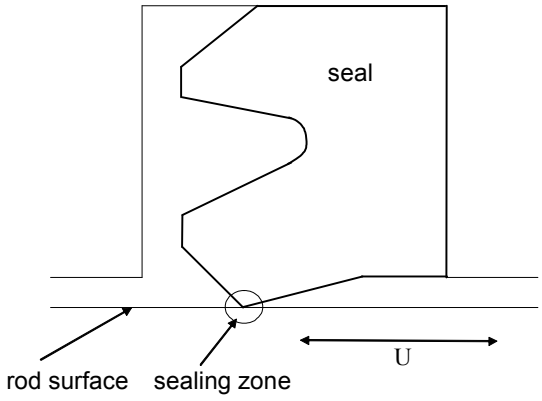

Figure 1.1: Typical hydraulic rod seal.

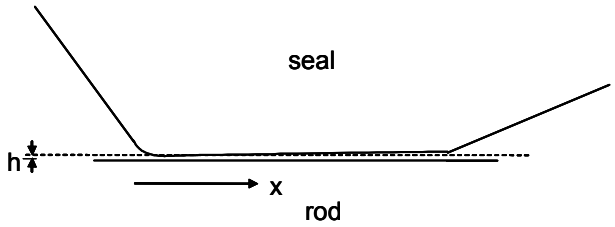

Figure 1.2: Sealing zone, as represented in previous models.

The analysis of the seal behavior is a problem in soft elastohydrodynamics, since the fluid pressure distribution in the sealing zone deforms the seal and affects the film thickness distribution, while the film thickness distribution affects the fluid mechanics and determines the fluid pressure distribution. In the previous models, the neglect of roughness and the assumption of full film lubrication have been shown through experiment to be unrealistic [5]-[7], and have led to erroneous predictions. For example, some studies predict that a seal which produces a static contact pressure distribution with a steep slope near the liquid side of the sealing zone and a gradual slope near the air side, will not leak provided the ratio of the outstroke rod speed to the contact pressure slope on the liquid side is less than the ratio of the instroke rod speed to the contact pressure slope on the air side [8]. Experience has shown that this is not necessarily true.

In the present study, the assumptions of zero roughness and full film lubrication have been eliminated. It should be noted that a recent series of papers also takes account of surface roughness and mixed lubrication, but is limited to a special class of seals, those with a rectangular cross-section [9]-[11].

1.3 Brief Summary of Each Chapter

Chapter 1 contains a brief description of the problem and the objective of the research.

Chapter 2 focuses on the research background of modeling and simulation of rod seals. This part summarizes the limitations of previous work and introduces the new coupled model which considers mixed lubrication and surface roughness.

Chapter 3 is the theoretical focus of the thesis. Using the single lip seal as an example, all the methodology is elaborated in this chapter.

Chapter 4 introduces the double lip seal and tandem seal. The advantages and disadvantages between them and single lip seal are discussed.

Chapter 5 introduces the step seal. Its performance is compared with the double lip seal for various operation conditions.

Chapter 6 analyzes a seal with a micro-scale surface pattern. It is shown that a properly designed pattern is effective in improving the leakage characteristics of hydraulic seals.

Chapter 7 compares the performance of a U-cup seal and O-ring for a micro actuator application.

Chapter 8 is a summary of the model development.

CHAPTER 2

RESEARCH BACKGROUND

A significant amount of research on reciprocating hydraulic seals, both experimental and theoretical has been performed in the last eighty years and is described in a recent review [12]. Theoretical modeling work dates back to at least 1964 [13]. Since that time many studies have been performed, but these have not had a significant impact on the practical aspects of seal design, as implied above (in the Introduction section). The reason for this will be discussed below.

2.1 Experimental Studies

Experimental research on hydraulic seals has made steady progress as experimental techniques developed. From using counting cups for leakage measurements to the high speed CCD camera filming of the contacting surface, there has been a long journey to the success of custom built measurement and observation techniques. The leakage rate, the seal frictional force, the contact film thickness and the contact pressure distribution are the four most important characteristics in all of those studies.

Collecting the fluid leaked out of a cylinder using a counting cup and weighing the mass is the oldest and the most popular method for the measurement of leakage of reciprocating seals [14]-[20]. This is also the standard method used in industry. If the leaked fluid is so little that all of it evaporates and can't be collected, the seal is considered to be leakless. Some other more precise and real-time techniques like

measuring the electrical capacitance of leaked oil layers using electrodes also have been used by researchers [21].

Most of the experimental studies include the measurement of friction force exerted on the rod by the reciprocating seals. The friction force itself can be very easily measured by force transducer [22]-[24]. There mostly lie two problems. First is the suspension of housing or rod, which may introduce non-negligible contributions to total friction; different techniques were used to minimize or measure that part. Second is the separation of the measurements for the outstroke and instroke friction. Mainly four schemes have been developed. White and Denny [25] in 1947 designed the basic concepts of friction measurement, which has two seals at the two ends of the housing. Cheyney, Muller and Duval [26] in 1950 designed a test rig to determine separate outstroke and instroke friction, which has a seal at one end of housing and a clearance at the other end. Rod with a closed housing technique is developed by Lawrie and O'Donoghue [27] in 1964. The concepts of a divided rod, two rods are connected by a force transducer, was used by Gawrys and Kollek [28] in 1984.

The techniques used for the measurement of static contact pressure distributions include strain gauge, piezoelectric force transducer, photo elastic method, as well as inductive transducer. Most of these methods are developed in 1970s to 1980s by Olssen, Molari, Austin, Kawahara and more [16], [18], [29]-[39].

The measurement of the contact film thickness using optical interferometry has been discussed since at least the 1960s. However, from the early works of Blok and Koens [40] in 1965 and Roberts and Tabor [41] a few years later, to recent studies of Kanzaki and Kaneta [42]-[44], in order to solve the problem of poor reflectivity of rubber

surfaces (due to surface roughness and dark color), the specimen either is specially molded to improve its smoothness or covered by an external thin sheet. However, these methods change the rubber's natural surface roughness; so the tests may not reflect reality. Rana [45] developed a gold coating method; seal specimens were coated with four 50 nm thick layers of gold. This method minimized the influence on seal roughness.

Apart from optical interferometry, direct observation of lubricating films also has been done. From the 1970s to recently, Schrader, Kawahara and Rana have designed various test rigs to record the sealing surface using a high speed camera [6], [46]-[48]. Rana's recent rig is capable of observing cavitation from hydraulic fluid starvation, air bubbles at the edges of the sealing contact, as well as obstruction of fluid replenishment by the accumulation of debris particles under dynamic conditions, such as varying contact load on the seal, the reciprocating frequency, and the stroking length.

2.2 Theoretical Studies

2.2.1 Material Models

In order to allow automatic adaption to shaft vibration and sealed pressure variations, seals normally are made of flexible materials, either elastomers (generally rubber compounds), or thermoplastics such as PTFE, polyurethanes. For strains exceeding a certain limit, such materials exhibit a non-linear stress–strain behavior, including hyperelasticity, viscoelasticity and viscoplasticity, which make their material property modeling a complicated task.

For incompressible, rubber-like materials, the most popular phenomenological models [49]-[51] are hyperelastic material models, such as Ogden model [52]-[54], Neo-

Hookean model [55] and Mooney–Rivlin model [56]-[57]. In these models, the mechanical properties are represented in terms of the energy function. Specifically, the elastic strain energy per unit volume W is expressed as a function of the three strain invariants, that is $W = W(I_1, I_2, I_3)$. I_1, I_2, I_3 are functions of $\lambda_1\ \lambda_2\ \lambda_3$, where λ_i (i = 1, 2, 3) stands for principal stretch (ratio of deformed to reference length).

For Neo-Hookean model, the form of the strain energy potential is:

$$W = \frac{\mu}{2}(\overline{I_1} - 3) + \frac{1}{d}(J-1)^2 \tag{2.1}$$

where:

μ = initial shear modulus of materials

d = material incompressibility parameter

For 2 parameter Mooney-Rivlin model, the form of the strain energy potential is:

$$W = C_{10}(\overline{I_1} - 3) + C_{01}(\overline{I_2} - 3) + C_{11}(\overline{I_1} - 3)(\overline{I_2} - 3) + \frac{1}{d}(J-1)^2 \tag{2.2}$$

where: $C_{10}, C_{01}, C_{11}, d$ are material constants.

For Ogden model, the form of the strain energy potential is:

$$W = \sum_{i=1}^{N} \frac{\mu_i}{\alpha_i}(\overline{\lambda_1^{\alpha_i}} + \overline{\lambda_2^{\alpha_i}} + \overline{\lambda_3^{\alpha_i}} - 3) + \sum_{k=1}^{N} \frac{1}{d_k}(J-1)^{2k} \tag{2.3}$$

where:

N = material constant

μ_i, α_i, d_k = material constants

Although hydraulic seals are made largely or entirely of rubber, silicone and other elastomers, PTFE and other composite materials are also widely used because of their excellent mechanical and chemical properties. The main benefits of these materials over

elastomers are their low friction, avoidance of extrusion and high resistance to thermal and chemical degradation [58].

PTFE is a thermoplastic and is well known for its low-friction properties. It has a very high resistance to ageing and suitable for applications with temperatures in excess of 250°C [59] which are not allowed for elastomers. To improve its mechanical properties, PTFE normally is filled with metal, graphite or glass fibers to form complex compounds. So PTFE in its various compounds has different response in tension and compression, its yield point, Young's modulus and Poisson's ratio all greatly depend on its composition and manufacture process [60]-[63].

2.2.2 Seal Mechanisms

The elasticity of polymers makes the theoretical analysis of hydraulic seals a complicated task. The complexity of the phenomenological materials models allows analytical solutions in structural analysis for only the simplest geometries such as rectangular. In recent studies, commercial finite-element software has been used to deal with complex geometries.

Since a lubricating film of micrometer thickness is present at the contacting surface, the fluid mechanics of the lubricating film is coupled with the elastic deformation mechanics of the sealing element. The calculation of that film thickness and its distribution in a contact is based on the theory of elastohydrodynamics lubrication. The fluid mechanics of the lubricating film is governed by the Reynolds equation (for the hydrodynamic pressure P), which contains the local film thickness H. The deformation of the sealing element is governed by the elasticity equations (for H), which contain P. The

coupling between these equations is handled in one of two ways, the direct method or the inverse method.

In the inverse method [8], [17], [64] the hydrodynamic pressure distribution is assumed to be known and equal to the static contact pressure distribution (since the static interference is much larger than the additional deformations due to the hydrodynamic pressure). The Reynolds equation is then solved for the film thickness distribution, in closed form, yielding a simple expression that can be used to estimate the leakage during the instroke and outstroke. White and Denny [14] assumed a parabolic static pressure distribution and a tapered film profile to calculate film thickness. Müller [15] also used a tapered film profile but the contact pressures are derived from measurements. Later, according to inverse hydrodynamic theory [65], the Reynolds equation is used to obtain a cubic algebraic equation for the film thickness [66]. However, the flexibility of the seals brings numerical instability problems for the application of this method to elastomeric seals [67]-[69]. To tackle this problem, Nikas [70] developed a modified version of the inverse hydrodynamic theory. Instead of solving the cubic algebraic equation, a first-order, ordinary differential equation is obtained and solved.

In the direct method, iteration is used. The film thickness distribution H is initially guessed, and the Reynolds equation is numerically solved for the pressure distribution P. The pressure P is then inserted into the elasticity equations, which are solved for the deformation (e.g. using FEA) and, therefore, H. The new values of H are inserted into the Reynolds equation, which is re-solved for new pressure P. Iteration is continued until the solution is converged. However, numerical instability and inconsistency also exists for this method, like the oscillating pressure and film thickness distributions and the slow

numerical convergence. Most studies have been focused on the improvement of numerical stability.

The study of Field and Nau [71], are representatives of this methodology. Ruskell [72] tackled the instability problem by combining the elasticity equation of the seal and the Reynolds equation, which was solved iteratively. A similar method is used by Prati and Strozzi [41] and Yang, Y. and Hughes [73]. Then Nikas [9]-[11], [74]-[76] developed a method that separates the effect of the roughness asperities and the effect of the bulk contact pressure. However the problems of convergence and consistency still have not been totally solved.

Most of the previous analytical models of reciprocating rod seals make two key assumptions: i. full film lubrication, i.e. a continuous liquid lubricating film separates the sealing element from the rod during operation, and ii. perfectly smooth sealing surfaces. While these models has been of some help to designers in that it gives some guidance as to the required shape of the static contact pressure distribution, it was found as early as 1973 that there are serious problems with the basic assumptions of all the models discussed above [5]. Experimental measurements have shown that the assumption of full film lubrication is very questionable. Over a wide range of conditions, mixed lubrication (in which there is asperity contact between the sealing element and the rod) occurs [6]. Furthermore, the assumption of smooth sealing surfaces is unrealistic. Experiments have shown that surface roughness, especially roughness of the sealing element, plays an important role in the lubrication of these seals [7].

Thus, it is not surprising that previous research studies, in particular previous analytical models, have not had a significant impact on practical seal design. A successful

model must take account of both mixed lubrication and surface roughness effects. It is the intent of this research to do.

CHAPTER 3

SINGLE LIP SEAL

3.1 Seal Configuration

Figure 3.1 shows a typical single lip U-Cup hydraulic rod seal, which is characterized by a sealing lip that contacts the rod with a line contact for a wide range of pressures. At the oil side, the angle between the lip and rod is much larger than that at air side. This has been proven to be a critical point for a successful design.

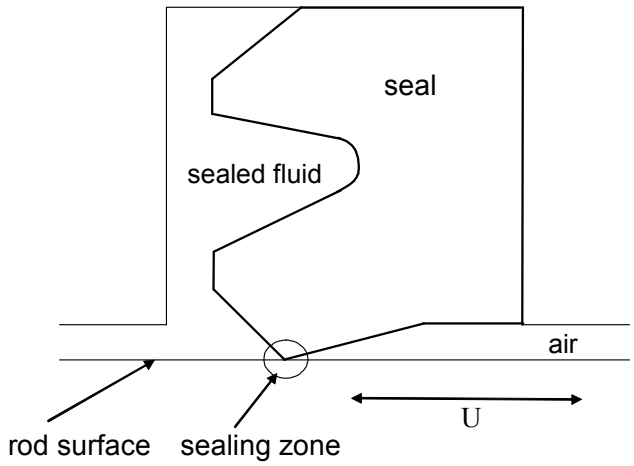

Figure 3.1: Typical single lip U-Cup hydraulic rod seal.

During the outstroke, as the rod moves to the right, hydraulic fluid is drawn out of the cylinder with Couette flow in the sealing zone. In most conventional actuator applications, the cylinder pressure adjacent to the seal is ambient during the outstroke. However, in the injection molding application, that pressure is significant and results in

Poiseuille flow in the outward direction in addition to the Couette flow. During the instroke, as the rod moves to the left, hydraulic fluid is drawn back into the cylinder, with Couette flow in the sealing zone. Since in all applications there is a significant cylinder pressure adjacent to the seal during the instroke, there is also Poiseuille flow in the outward direction. The net leakage over a cycle will equal the fluid transport during the outstroke minus that during the instroke. In order for the net leakage to be zero, the fluid transport out of the cylinder during the outstroke must be less than the inward transport that the seal is capable of inducing during the instroke. The net leakage per cycle of the seal is defined as the difference between the fluid transport out of the cylinder during the outstroke and the transport back into the cylinder during the instroke.

Figure 3.2 shows a schematic of the sealing zone, as it is represented in the present model, in a state of mixed lubrication. In general there will be contact between asperities on the lip surface and the rod. The rod is much smoother than the seal, so it is treated as perfectly smooth. There will also be a lubricating film of hydraulic fluid in this region, usually of μm or sub-μm scale thickness.

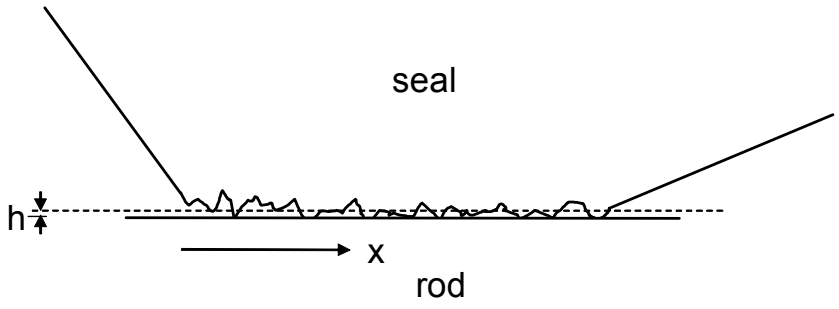

Figure 3.2: Sealing zone, as represented in present model.

3.2 Assumptions

In order to compute the net leakage through the sealing zone, as well as the friction force on the rod and the details of the behavior in the sealing zone, a model that analyzes the sealing zones must be developed.

This model consists of four components, a fluid mechanics analysis of the flow in the lubricating film, a contact mechanics analysis of the contacting asperities, a deformation analysis of the seal, and a thermal analysis of the hydraulic fluid in the sealing zone.

The fluid mechanics analysis computes the fluid pressure distribution in the sealing zone, the leakage rate and the viscous friction, and reveals if cavitation occurs. This cavitation happens when the pressure gets very low, and air that is dissolved in the hydraulic fluid comes out of solution to form a liquid-air mixture.

The contact mechanics analysis computes the contact pressure distribution and the friction due to contacting asperities.

The thermal analysis computes the heat generation and the temperature at the contacting surface, and then determines the viscosity of the hydraulic fluid.

The deformation mechanics analysis computes the deformed shape of the seal, which allows one to determine the fluid film thickness distribution and the local interference.

Since these four components are strongly coupled, an iterative computation procedure is required.

To achieve this objective with a reasonable computation time, it has been necessary to make a number of simplifying assumptions. These assumptions include:

I. This is a steady-state model, so it is only valid when the stroke length is large compared to the seal width.

II. Since only steady state is considered, viscoelastic effects are not present.

III. The rod is treated as perfectly smooth. This is reasonable, since during the run-in period, the rod is polished to a very smooth finish. The rod surface roughness is typically one-tenth that of the seal surface.

IV. The deformation is treated as hyperelastic.

V. The geometry is assumed as axisymmetric.

VI. The air side of the seal is flooded with lubricant, so the fluid transport during instroke can always be calculated.

VII. The Greenwood-Williamson contact model is used, which ignores dynamic effects.

VIII. The friction force due to contacting asperities is computed with an empirical friction coefficient.

3.3 Fluid Mechanics Analysis

3.3.1 Governing Equations

Since the thickness of the lubrication film normally is on the micro meter scale, which is small when compared to the length of the sealing zone, this allows the flow in the sealing zone to be modeled as one-dimensional using a Cartesian coordinate system. The fluid mechanics of the lubricating film is governed by Reynolds equation. Since cavitation is possible in portions of the film, the cavitation index F and the average density/Pressure Function Φ are used to account for such effect [77].

In dimensionless terms,

$$\frac{d}{d\hat{x}}\left[\phi_{xx}H^3 e^{-\hat{\alpha}F\phi}\frac{dF\phi}{d\hat{x}}\right] = 6\zeta\left[\frac{d}{d\hat{x}}\left\{\left[1+(1-F)\phi\right]H_T\right\} + F\frac{d\phi_{s.c.x}}{d\hat{x}}\right] \tag{3.1}$$

In the liquid region, F equals 1 and Φ represents the dimensionless fluid pressure,

$$\phi \geq 0 \quad F = 1 \text{ and } P = \phi \tag{3.2}$$

while in the cavitated region, F equals 0 and Φ is related to the dimensionless density.

$$\phi < 0 \quad F = 0 \text{ and } P = 0,\ \hat{\rho} = 1 + \phi \tag{3.3}$$

The boundary conditions are,

$$\begin{aligned} \phi &= P_{sealed} \text{ at } \hat{x} = 0 \\ &= 1 \qquad \text{at } \hat{x} = 1 \end{aligned} \tag{3.4}$$

The average truncated film thickness is given by,

$$H_T = \int_{-H}^{\infty} \left[H + \delta\right] f(\delta) d\delta \tag{3.5}$$

which, for a Gaussian distribution is,

$$H_T = \frac{H}{2} + \frac{H}{2} erf\left(\frac{H}{\sqrt{2}}\right) + \frac{1}{\sqrt{2\pi}} e^{\left(\frac{-H^2}{2}\right)} \tag{3.6}$$

Here ϕ_{xx} and $\phi_{s.c.x}$ are flow factors that take into account the effect of the surface roughness of the seal lip. They are functions of the ratio of the film thickness to the roughness amplitude and the roughness geometry (aspect ratio and orientation of the asperities). These flow factors are computed numerically using equations derived and outlined by Patir and Cheng [78]-[79].

The Reynolds equation, eq.(3.1), is put into finite volume form and solved for Φ and F for given values of H, using the tri-diagonal matrix algorithm. This yields the

pressure distribution and the locations of cavitating regions. The flow rate (per unit circumferential length) and the shear stress on the rod can then be computed from,

$$\hat{q} = -\phi_{xx} e^{-\hat{\alpha} F \phi} H^3 \frac{dF\phi}{dx} + 6\zeta \left\{ \left[1 + (1-F)\phi \right] H_T + F\phi_{s.c.x} \right\} \tag{3.7}$$

and,

$$\hat{\tau}_{avg} = \frac{\tau_{avg}}{E} = \frac{-\hat{\sigma}}{\xi} e^{-\hat{\alpha} F \phi} \frac{\varsigma}{H} \left(\phi_f - \phi_{fss} \right) - \phi_{fpp} \frac{\hat{\sigma}}{\xi} \frac{H}{2} \frac{dF\phi}{d\hat{x}} \tag{3.8}$$

The shear stress flow factors, ϕ_f , ϕ_{fss}, and ϕ_{fpp} are obtained from [79].

3.3.2 Numerical Algorithms

The analytical solution of equation (3.1) is not obtainable. Thus, a numerical method is implemented. A control volume scheme is used to discretize the equation over the solution domain to get a system of linear equations. Then these equations are solved using the tri-diagonal matrix algorithm.

The solution domain is generated during the deformation analysis; the coordinate of every node and the contact pressure at every node is exported and written to an output file. In the fluid mechanics analysis, the node coordinates are read in and non-dimensionalized.

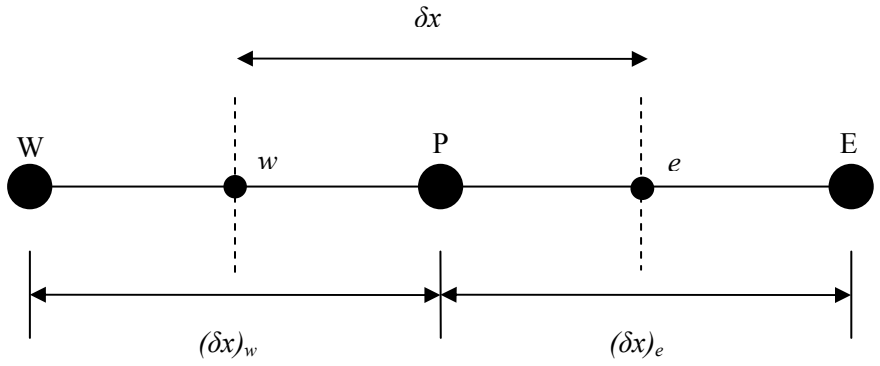

Figure 3.3: Diagram of control volume for discretization process.

A single control volume illustrates how the Reynolds equation is discretized. This control volume scheme uses the e and w nodes, which are defined as being located at the midpoint between the W and P and E and P nodes respectively, as shown in Figure 3.3.

Where:

$$\begin{aligned}(\delta x)_w &= x_P - x_W \\ (\delta x)_e &= x_E - x_P \\ \delta x &= \frac{(\delta x)_w + (\delta x)_e}{2}\end{aligned} \tag{3.9}$$

K is defined as

$$K = \varphi_{xx} H^3 e^{-\hat{\alpha} F \phi} \tag{3.10}$$

Equation (3.1) then becomes:

$$\frac{d}{d\hat{x}}\left[K \frac{d}{d\hat{x}}\left(F\varphi\right)\right] - 6\zeta \frac{d}{d\hat{x}}\left[\left\{1+\left(1-F\right)\varphi\right\}\cdot H_T\right] - 6\zeta F \frac{d\varphi_{s.c.x.}}{d\hat{x}} = 0 \tag{3.11}$$

Integrating equation (3.11) over the control volume from x_w to x_e yields the following:

$$\int_{x_w}^{x_e} \frac{d}{d\hat{x}}\left[K \frac{d}{d\hat{x}}(F\varphi)\right] d\hat{x} - \int_{x_w}^{x_e} 6\zeta \frac{d}{d\hat{x}}\left[\left\{1+(1-F)\varphi\right\}\cdot H_T\right] d\hat{x} - \int_{x_w}^{x_e} 6\zeta F \frac{d\varphi_{s.c.x.}}{d\hat{x}} d\hat{x} = 0 \quad (3.12)$$

Now, integrating the first term,

$$\int_{x_w}^{x_e} \frac{d}{d\hat{x}}\left[K \frac{d}{d\hat{x}}(F\varphi)\right] d\hat{x} = \left(K \frac{d}{d\hat{x}}(F\varphi)\right)_e - \left(K \frac{d}{d\hat{x}}(F\varphi)\right)_w \quad (3.13)$$

Approximating the derivative with finite differences gives

$$\left(K \frac{d}{d\hat{x}}(F\varphi)\right)_e - \left(K \frac{d}{d\hat{x}}(F\varphi)\right)_w = K_e \frac{F_E\varphi_E - F_P\varphi_P}{\delta\hat{x}_e} - K_w \frac{F_P\varphi_P - F_W\varphi_W}{\delta\hat{x}_w} \quad (3.14)$$

Define K_e and K_w using the harmonic mean, respectively,

$$K_e = \frac{2\cdot K_E \cdot K_P}{(K_E + K_P)} \quad (3.15)$$

$$K_w = \frac{2\cdot K_W \cdot K_P}{(K_W + K_P)}$$

Finite differencing the second term yields,

$$\int_{x_w}^{x_e} 6\zeta \frac{d}{d\hat{x}}\left[\left\{1+(1-F)\varphi\right\}\cdot H_T\right] d\hat{x} = 6\zeta\left\{\left(\left[1+(1-F)\varphi\right]\cdot H_T\right)_e - \left(\left[1+(1-F)\varphi\right]\cdot H_T\right)_w\right\} \quad (3.16)$$

where $(H_T)_e$ and $(H_T)_w$ are defined using the arithmetic mean,

$$(H_T)_e = \frac{(H_T)_P + (H_T)_E}{2} \quad (3.17)$$

$$(H_T)_w = \frac{(H_T)_P + (H_T)_W}{2}$$

An "upwind" scheme is applied to Equation, where the scheme is dependent on the direction of flow [80]. For flow in a positive x-direction, equation (3.16) becomes,

$$\int_{x_w}^{x_e} 6\zeta \frac{d}{d\hat{x}}\left[\left\{1+\left(1-F\right)\varphi\right\}\cdot H_T\right]d\hat{x} = 6\zeta\left\{\left[1+\left(1-F_P\right)\varphi_P\right]\cdot\left(H_T\right)_e-\left[1+\left(1-F_W\right)\varphi_W\right]\cdot\left(H_T\right)_w\right\}$$

(3.18)

For flow in a negative x-direction, the second term is defined by,

$$\int_{x_w}^{x_e} 6\zeta \frac{d}{d\hat{x}}\left[\left\{1+\left(1-F\right)\varphi\right\}\cdot H_T\right]d\hat{x} = 6\zeta\left\{\left[1+\left(1-F_E\right)\varphi_E\right]\cdot\left(H_T\right)_e-\left[1+\left(1-F_P\right)\varphi_P\right]\cdot\left(H_T\right)_w\right\}$$

(3.19)

By grouping similar terms from the simplification of the finite difference equations and applying a harmonic mean for the flow factors, the third term becomes,

$$\int_{x_w}^{x_e} 6\zeta F\frac{d\varphi_{s.c.x.}}{d\hat{x}}d\hat{x} = 6\zeta\cdot F_P\left[\left(\frac{2\cdot\left(\varphi_{s.c.x.}\right)_P\cdot\left(\varphi_{s.c.x.}\right)_E}{\left(\varphi_{s.c.x.}\right)_P+\left(\varphi_{s.c.x.}\right)_E}\right)-\left(\frac{2\cdot\left(\varphi_{s.c.x.}\right)_P\cdot\left(\varphi_{s.c.x.}\right)_W}{\left(\varphi_{s.c.x.}\right)_P+\left(\varphi_{s.c.x.}\right)_W}\right)\right] \quad (3.20)$$

Then substitute equations (3.13)-(3.19) back into equation (3.12), the equation (3.12) becomes,

$$A_P\varphi_P = A_E\varphi_E + A_W\varphi_W + b \quad (3.21)$$

where for a positive rod speed

$$\begin{aligned}
A_P &= \left(\frac{K_e}{(\delta x)_e}+\frac{K_w}{(\delta x)_w}\right)F_P + 6\zeta\left(1-F_P\right)\left(H_T\right)_E \\
A_E &= \frac{K_e}{(\delta x)_e}\left(F_E\right) \\
A_W &= \frac{K_w}{(\delta x)_w}\left(F_W\right) \\
b &= -6\zeta\cdot H_E + 6\zeta\left\{\left[1+\left(1-F_W\right)\varphi_W\right]\left(H_T\right)_W\right\} - \\
&\quad 6\zeta\cdot F_P\left[\left(\frac{2\cdot\left(\varphi_{s.c.x.}\right)_P\cdot\left(\varphi_{s.c.x.}\right)_E}{\left(\varphi_{s.c.x.}\right)_P+\left(\varphi_{s.c.x.}\right)_E}\right)-\left(\frac{2\cdot\left(\varphi_{s.c.x.}\right)_P\cdot\left(\varphi_{s.c.x.}\right)_W}{\left(\varphi_{s.c.x.}\right)_P+\left(\varphi_{s.c.x.}\right)_W}\right)\right]
\end{aligned} \quad (3.22)$$

and for a negative rod speed

$$
\begin{aligned}
A_P &= \left(\frac{K_e}{(\delta x)_e} + \frac{K_w}{(\delta x)_w} \right) F_P + 6\zeta \left(1 - F_P\right)\left(H_T\right)_W \\
A_E &= \frac{K_e}{(\delta x)_e}\left(F_E\right) \\
A_W &= \frac{K_w}{(\delta x)_w}\left(F_W\right) \\
b \quad &= 6\zeta \cdot H_W - 6\zeta \left\{ \left[1 + \left(1 - F_E\right)\varphi_E \right]\left(H_T\right)_E \right\} - \\
&\quad 6\zeta \cdot F_P \left[\left(\frac{2 \cdot \left(\varphi_{s.c.x.}\right)_P \cdot \left(\varphi_{s.c.x.}\right)_E}{\left(\varphi_{s.c.x.}\right)_P + \left(\varphi_{s.c.x.}\right)_E} \right) - \left(\frac{2 \cdot \left(\varphi_{s.c.x.}\right)_P \cdot \left(\varphi_{s.c.x.}\right)_W}{\left(\varphi_{s.c.x.}\right)_P + \left(\varphi_{s.c.x.}\right)_W} \right) \right]
\end{aligned}
\tag{3.23}
$$

In terms of the node index *i*, equation is unified as,

$$
A_i \varphi_i = B_i \varphi_{i+1} + C_i \varphi_{i-1} + D_i \tag{3.24}
$$

where A_i, B_i, C_i, and D_i are defined for a positive speed by,

$$
\begin{aligned}
A_i &= \left(\frac{2 \cdot K_{i+1} \cdot K_i}{K_{i+1} + K_i} \Big/ (x_{i+1} - x_i) + \frac{2 \cdot K_{i-1} \cdot K_i}{K_{i-1} + K_i} \Big/ (x_i - x_{i-1}) \right) \cdot F_i + 6\zeta \left(1 - F_i\right)\left(H_T\right)_{i+1} \\
B_i &= \left(\frac{2 \cdot K_{i+1} \cdot K_i}{K_{i+1} + K_i} \right) \Big/ (x_{i+1} - x_i) \cdot F_{i+1} \\
C_i &= \left(\frac{2 \cdot K_{i-1} \cdot K_i}{K_{i-1} + K_i} \right) \Big/ (x_i - x_{i-1}) \cdot F_{i-1} \\
D_i &= -6\zeta \cdot H_{i+1} + 6\zeta \left\{ \left[1 + \left(1 - F_{i-1}\right)\varphi_{i-1} \right]\left(H_T\right)_{i-1} \right\} \\
&\quad - 6\zeta \cdot F_P \left[\left(\frac{2 \cdot \left(\varphi_{s.c.x.}\right)_i \cdot \left(\varphi_{s.c.x.}\right)_{i+1}}{\left(\varphi_{s.c.x.}\right)_i + \left(\varphi_{s.c.x.}\right)_{i+1}} \right) - \left(\frac{2 \cdot \left(\varphi_{s.c.x.}\right)_i \cdot \left(\varphi_{s.c.x.}\right)_{i-1}}{\left(\varphi_{s.c.x.}\right)_i + \left(\varphi_{s.c.x.}\right)_{i-1}} \right) \right]
\end{aligned}
\tag{3.25}
$$

and for a negative speed by,

$$
\begin{aligned}
A_i &= \left(\frac{2 \cdot K_{i+1} \cdot K_i}{K_{i+1} + K_i} \Big/ (x_{i+1} - x_i) + \frac{2 \cdot K_{i-1} \cdot K_i}{K_{i-1} + K_i} \Big/ (x_i - x_{i-1}) \right) \cdot F_i + 6\zeta \left(1 - F_i\right) \left(H_T\right)_{i-1} \\
B_i &= \left(\frac{2 \cdot K_{i+1} \cdot K_i}{K_{i+1} + K_i} \right) \Big/ (x_{i+1} - x_i) \cdot F_{i+1} \\
C_i &= \left(\frac{2 \cdot K_{i-1} \cdot K_i}{K_{i-1} + K_i} \right) \Big/ (x_i - x_{i-1}) \cdot F_{i-1} \\
D_i &= 6\zeta \cdot H_{i-1} - 6\zeta \left\{ \left[1 + \left(1 - F_{i+1}\right) \varphi_{i+1} \right] \left(H_T\right)_{i+1} \right\} \\
&\quad - 6\zeta \cdot F_P \left[\left(\frac{2 \cdot \left(\varphi_{s.c.x.}\right)_i \cdot \left(\varphi_{s.c.x.}\right)_{i+1}}{\left(\varphi_{s.c.x.}\right)_i + \left(\varphi_{s.c.x.}\right)_{i+1}} \right) - \left(\frac{2 \cdot \left(\varphi_{s.c.x.}\right)_i \cdot \left(\varphi_{s.c.x.}\right)_{i-1}}{\left(\varphi_{s.c.x.}\right)_i + \left(\varphi_{s.c.x.}\right)_{i-1}} \right) \right]
\end{aligned}
\tag{3.26}
$$

Equation (3.24) is solved using the TDMA procedure.

The *TDMA* procedure is programmed using *FORTRAN* language and is compiled in *Compaq Visual Fortran* environment.

3.4 Contact Mechanics Analysis

The contact mechanics analysis is based on the Greenwood and Williamson surface contact model [81]-[82], and is used to compute the contact pressure P_c.

3.4.1 Greenwood and Williamson Surface Contact Model

Assuming all the contacting asperities are purely elastic and treating each asperity contact spot as a separate, independently acting Hertzian contact between a sphere and a flat, the contact pressure can be expressed as

$$
P_c = \frac{4}{3} \eta \frac{E}{\left(1 - \nu^2\right)} R^{\frac{1}{2}} \int_d^\infty \Phi(z) \left(z - d\right)^{\frac{3}{2}} dz \tag{3.27}
$$

Assuming a Gaussian distribution of asperities

$$
\Phi(z) = \frac{1}{\sqrt{2\pi}\sigma} e^{-z^2 / 2\sigma^2} \tag{3.28}
$$

Let $u = \frac{z}{\sigma}$, then the contact pressure is computed from

$$P_c = \frac{4}{3}\eta \frac{E}{\left(1-\nu^2\right)} R^{\frac{1}{2}} \sigma^{\frac{3}{2}} I \tag{3.29}$$

where $I = \frac{1}{\sqrt{2\pi}} \int_{d/\sigma}^{\infty} \left(u - d/\sigma\right)^{3/2} e^{-u^2/2} du$. The integration can't be calculated analytically, so a numerical computation is made. Using *Matlab* to compute this integration at a series of points and using a fourth order polynomial curve to fit; one finds that, with a stand error of 1.5×10^{-4} and $R^2 = 0.999999$,

$$log_{10}\left(I\right) = C_4(\frac{d}{\sigma})^4 + C_3(\frac{d}{\sigma})^3 + C_2(\frac{d}{\sigma})^2 + C_1(\frac{d}{\sigma}) + C_0 \tag{3.30}$$

Where C_4 = 5.27094E-04, C_3 = -1.01490E-02, C_2 = -0.124475, C_1 = -0.619892 and C_0 = -0.367014. The maximum error for $\frac{z}{\sigma}$ from 0 to 6 is 0.13%. This range covers the range of mixed lubrication (from 0 to 3) and all the possible film thickness for this numerical model.

In eq. (3.29), E is Young's modulus and ν is Poisson's ratio, which are material property; I is a function of film thickness and calculated numerically; η asperity density, σ is the *RMS* roughness and R is average radius of asperities, which must be measured experimentally.

The shear stress on the rod due to contacting asperities is computed from the following equation:

$$\hat{\tau}_c = -fP_c\left(\frac{\varsigma}{|\varsigma|}\right) \tag{3.31}$$

using an empirical friction coefficient *f*.

3.4.2 Surface Measurements

In the Greenwood and Williamson surface contact model, a surface is defined by three characteristics: root mean square roughness σ, asperity density η and average radius of asperities *R*. Because the parameters η and *R* are highly scale dependent, while the autocorrelation length is relatively independent to the sampling interval within a reasonable range, we identify *R* as the autocorrelation length l_a, and taking the surface roughness to be isotropic, η is computed from autocorrelation length l_a : let autocorrelation length l_a to be the average distance between two asperities, then η is computed from

$$\eta = \frac{1}{(l_a / 2)^2} \tag{3.32}$$

So the root mean square roughness σ and autocorrelation length l_a should be measured directly.

Figure 3.4 shows the image of the surface of a typical polyurethane seal lip taken by a microscope. A regular pattern of circumferential grooves or ridges spaced about 0.04 mm apart can be observed. This is believed to be a result of the manufacturing process.

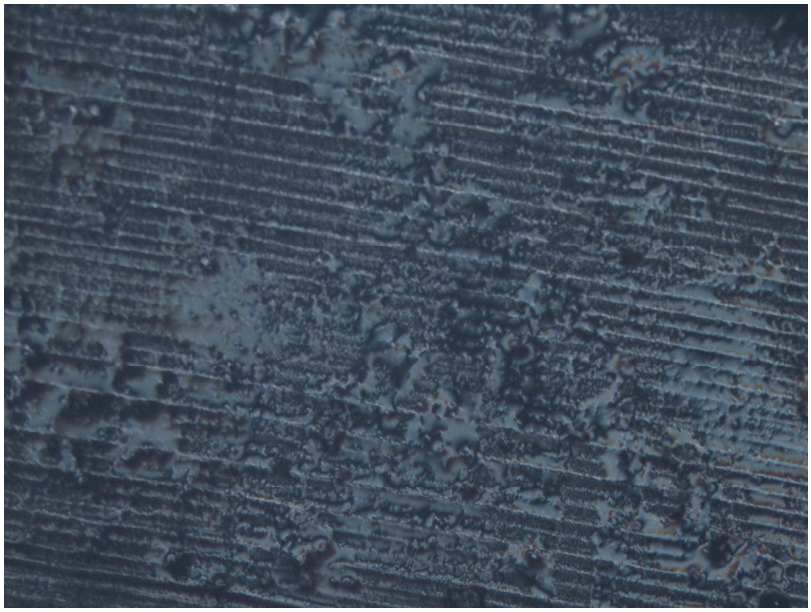

Figure 3.4: Surface image of a typical polyurethane seal lip.

Figure 3.5 and Figure 3.6 show the surface measurements from a *ZYGO* optical profilemeter.

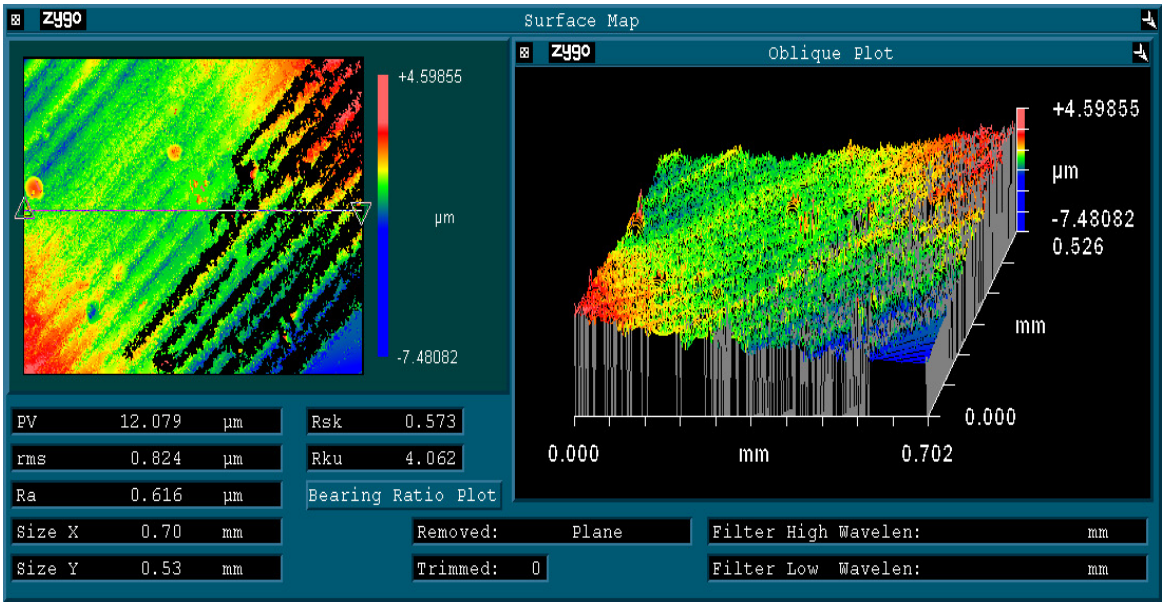

Figure 3.5: Surface map measurements from a *ZYGO* optical profilemeter

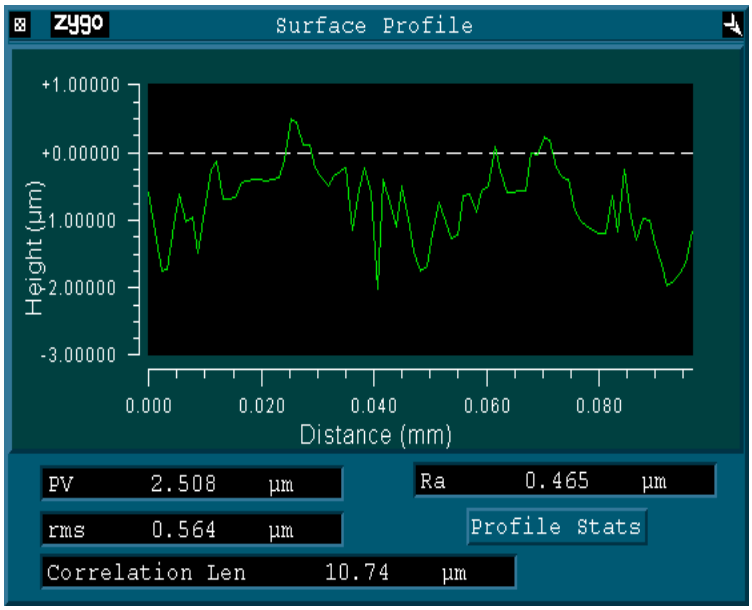

Figure 3.6: Surface profile measurements from a *ZYGO* optical profilemeter.

Four groups of samples are measured. On average, the RMS roughness is estimated at 0.8µm and the autocorrelation length is estimated at 4µm and asperity density is estimated at $4 \times 10^{11}\ m^{-2}$.

3.5 Thermal Analysis

During sliding, the temperature at the contact zone rises due to frictional heat generation. Since the mechanical properties (such as elastic modulus and hardness) and lubricating properties varies with the interface temperature, an estimate of the interface temperature rise is necessary for the analysis of seal performance.

3.5.1 Assumptions

The heat is generated at the contacting surface and then conducted into the seal and rod. The partition of heat is determined by assuming the surface temperature of the two parts is the same. From Table 3.1, it is seen that the thermal conductivity of steel is over 100 times larger than that of polyurethane, so essentially all of the heat generated in the sealing zone by viscous and contact friction ($\hat{\tau}_{avg}$ and $\hat{\tau}_c$) is transferred to the rod. Then the rod sliding through the reciprocating seal can be treated as a band source over a semi-infinite body.

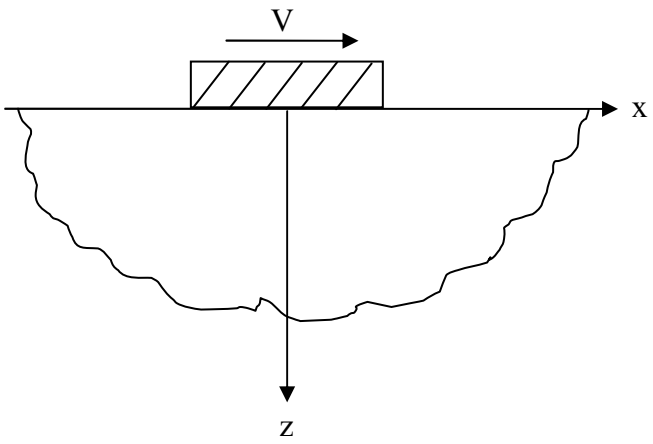

Figure 3.7: Schematic of a moving band heat source over a semi-infinite body.

3.5.2 Governing Equations

The heat transfer in the rod is governed by the classic heat conduction equation in a homogeneous isotropic solid. It is assumed that thermal properties are constant and heat is only introduced at the boundaries.

$$\frac{\partial^2\theta}{\partial x^2}+\frac{\partial^2\theta}{\partial y^2}+\frac{\partial^2\theta}{\partial z^2}=\frac{1}{\kappa}\frac{\partial\theta}{\partial t} \tag{3.33}$$

The heat generation rate is given by

$$q_{friction} = \left(\hat{\tau}_c + \hat{\tau}_{avg}\right) EU \tag{3.34}$$

The closed form solution of equation (3.33) is not available. Thus, an approximate solution is developed for the steady-state temperature in the sealing zone [83].

$$\begin{aligned} T_{ave} - T_{ambient} &= 1.07 \frac{q_{friction} L}{k} \left[\frac{\rho_r c_p UL}{k} \right]^{-1/2} \quad for\ \rho_r c_p UL / k > 0.68 \\ &= 0.64 \frac{q_{friction} L}{k} ln \left[\frac{5.0k}{\rho_r c_p UL} \right] \quad for\ \rho_r c_p UL / k < 0.68 \end{aligned} \tag{3.35}$$

Since the first equation had been developed for Peclet numbers ($\rho_r c_p Ul / k$) greater than 10 and the second for Peclet numbers less than 0.5, their use in the intermediate region represents an extrapolation. Comparison with the equations of Ref. [84], which include a separate correlation for the intermediate region, indicates a deviation of less than 5%. The deviation is shown by Figure 3.8.

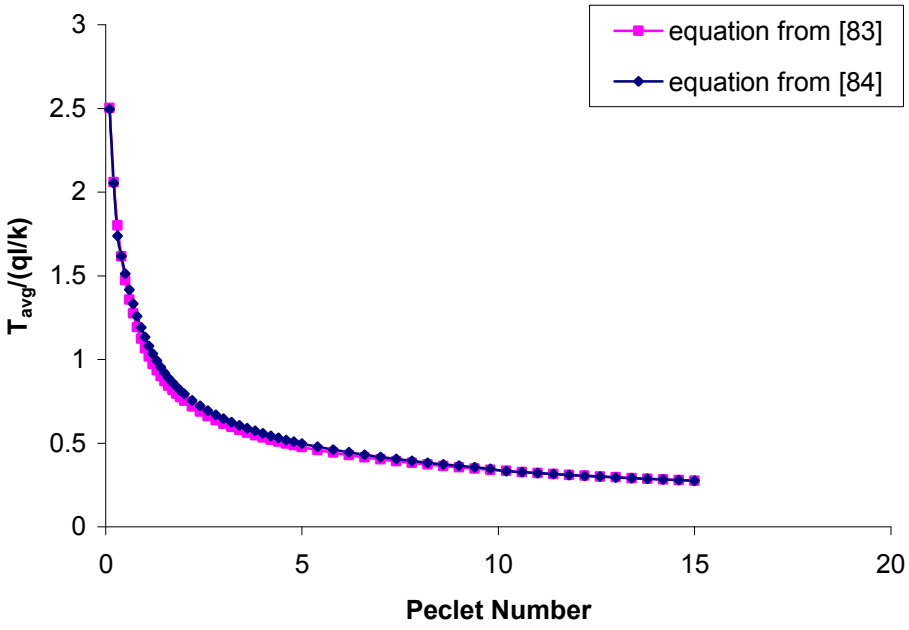

Figure 3.8: Approximate solutions of heat conduction equation.

This temperature is used to calculate the viscosity in the fluid mechanics analysis. The viscosity at several temperatures is given in Table 3.1. Interpolation is done with an exponential function. As pointed out earlier, this analysis assumes steady state, and is valid for applications in which the stroke length is significantly larger than the seal width.

3.6 Deformation Analysis

The radial (normal) deformation of the sealing element is computed by the finite element method, using the commercial software *ANSYS*.

3.6.1 Seal Geometry

Since the seal has a fairly complex shape, the geometric profile of the seal is quite difficult to be accurately generated in *ANSYS*. Therefore a separate CAD system is used to build the geometry and then exported to *ANSYS* for further analysis. The original designs of the seal are provided by the seal manufacture.

3.6.2 Material Properties

The seal under study, a Hallite U-cup rod seal, is made of polyurethane. Since steel is much more rigid than elastic polymers, to simplify the analysis, the housing and rod are assumed to be constructed from the same grade of steel. Then it is only necessary to consider two kinds of materials. For the steel, a linear elastic model is used with a Young's Modulus of 210 GPa and a Poisson's ratio of 0.29. For polyurethane, a hyperelastic model is used. At room temperature, it has an initial Young's Modulus of 43 MPa and a Poisson's ratio of 0.499. The coefficients for the two parameter Mooney Rivlin hyperelastic model are C_{10}=0.2 MPa, C_{01}=6 MPa and d = 0.000279.

3.6.3 Element Type

Plane183 is selected for seal body, rod and housing. It is a higher order 2D 8-node or 6-node element. It has quadratic displacement behavior and is well suited for modeling with irregular meshes. This element has two degrees of freedom at each node: translations in the nodal *x* and *y* directions. The element may be used as a plane element (plane stress, plane strain and generalized plane strain) or as an axisymmetric element. This element has plasticity, hyperelasticity, creep, stress stiffening, large deflection, and large strain capabilities.

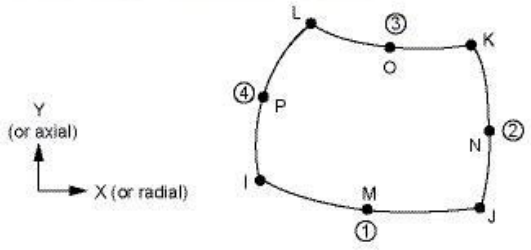

Figure 3.9: PLANE183 geometry.

Contact pairs between the seal and rod and between the seal and housing are defined using elements CONTA172 and TARGE169 with a coefficient of friction of 0.25. The CONTA172 element was used to simulate the contact surfaces as it is a 2-D 3-node surface-to-surface element. The TARGE169 is a 2-D target element, which is applied to rod and housing as they are much more rigid than the seal. The augmented Lagrangian method is selected for the contact algorithm.

3.6.4 Mesh and Convergence Analysis

From the fluid mechanics analysis, it's noted that the Poiseuille flow rate is proportional to the cube of film thickness and the Couette flow rate is proportional to film thickness, which means the flow rate is quite sensitive to film thickness. The mesh must be carefully refined to make the contact pressure curve as smooth as possible; at the same time, the total number of nodes must be limited since the computation time increases dramatically with node count. So at areas with a high pressure gradient such as the lip tip, the mesh must be refined, while at other areas, a moderate mesh is sufficient.

A convergence study was performed to ensure accurate results: the mesh was refined until further the results did not yield significantly different results. Figure 3.10 shows the meshed seal.

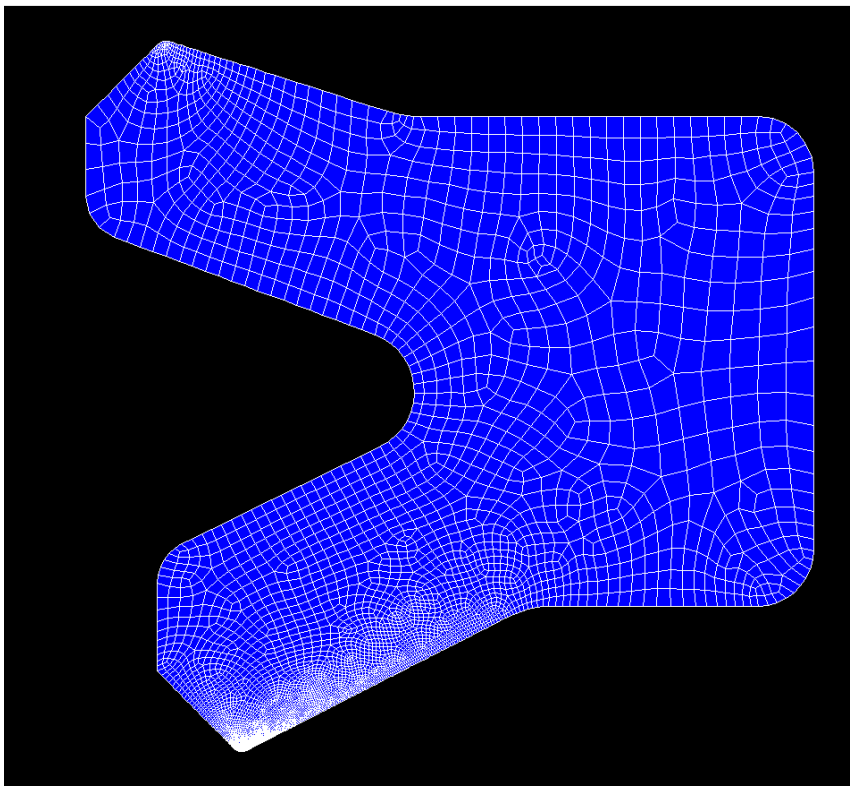

Figure 3.10: Single lip seal with the meshing.

3.6.5 Boundary Conditions

Figure 3.11 shows the defined boundary conditions. The housing and rod are fixed in the *x* direction. The housing moves down and rod moves up in the *y* direction to simulate the mounting process. The red outline around the seal surface shows the location of the surface load exerted by the sealed hydraulic fluid. The red arrows in the sealing zone indicate the generated fluid pressure in the lubrication film, which is computed from the previous fluid mechanics analysis.

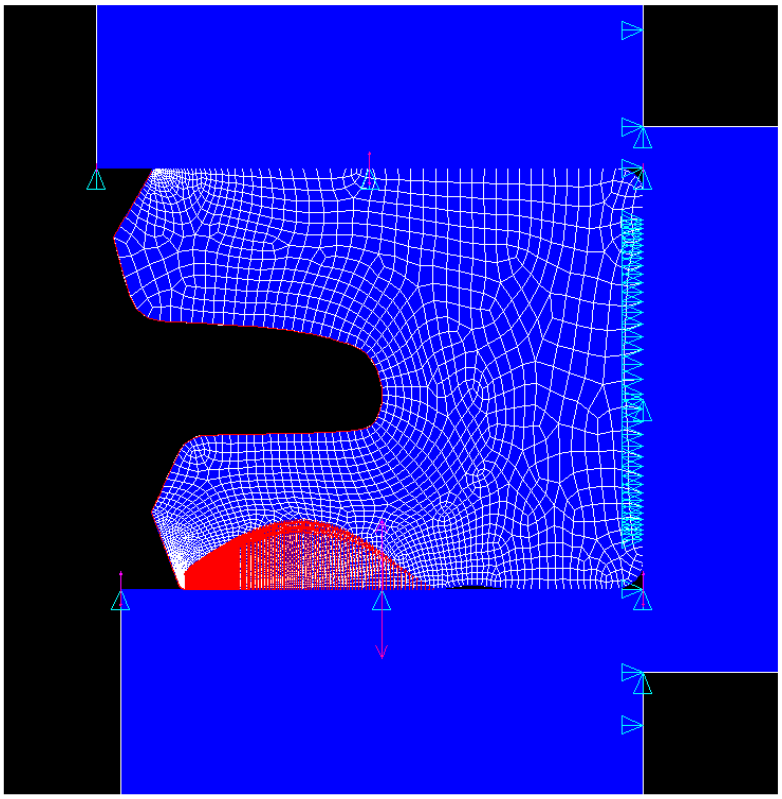

Figure 3.11: Boundary conditions of single lip seal.

At the oil side, for the areas without contact, oil pressure is a surface load exerted on the seal; at the contact area, the contact pressure serves as a surface load. These two loads must be continuous along the boundary, so it's important to determine the node that separates the contact area and non-contact area. This process is performed via a trial and error iteration.

Figure 3.12 shows the method.

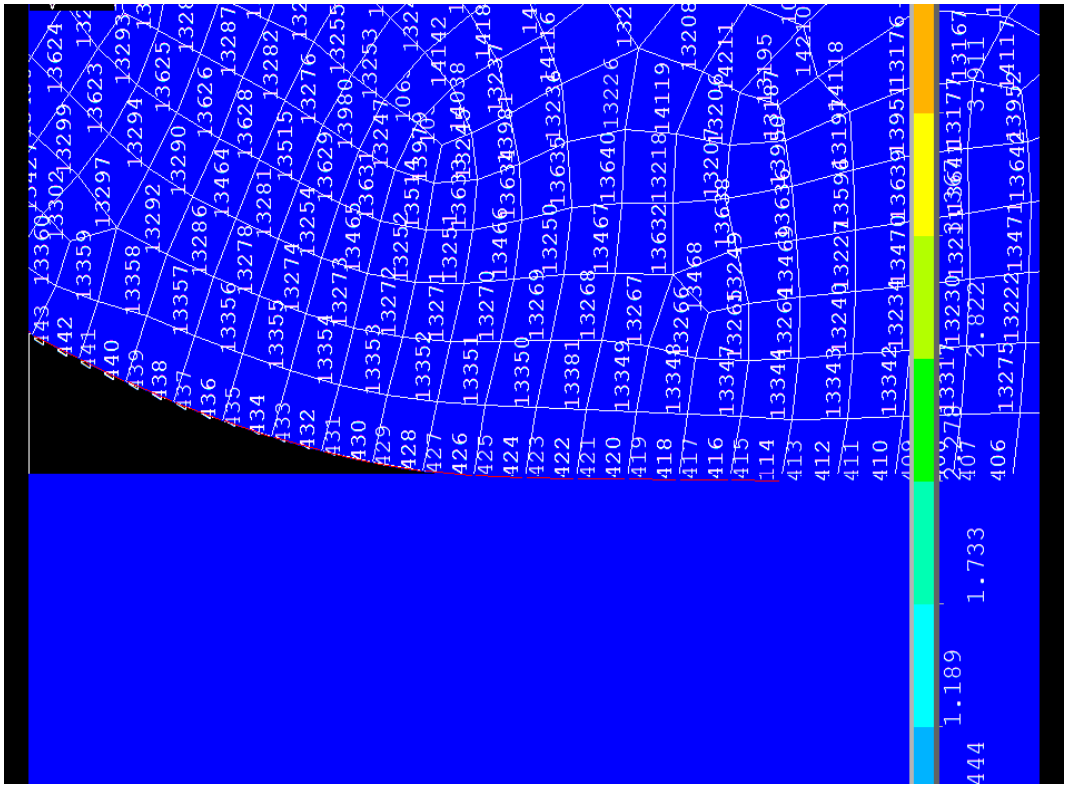

Figure 3.12: Deformed seal tip with node number and surface load.

The red line indicates the region of added surface load from oil pressure. Initially node 114 is used as a guess of the boundary, and then after analysis, it is observed that from node 114 to node 426, the nodes are contacting with rod and node 426 should be the

boundary. Then the oil surface load is revised according to the new boundary and the analysis is run again. Such a process iterates until the contact pressure at the boundary node has the best match with the sealed fluid pressure. Figure 3.13 shows the optimum surface load on seal. Also notice the node numbers in the sealing zone is not always continuous, such as node 114 between node 413 and node 415. It's important to find the pattern of node numbering, which is crucial for the succeeding analysis.

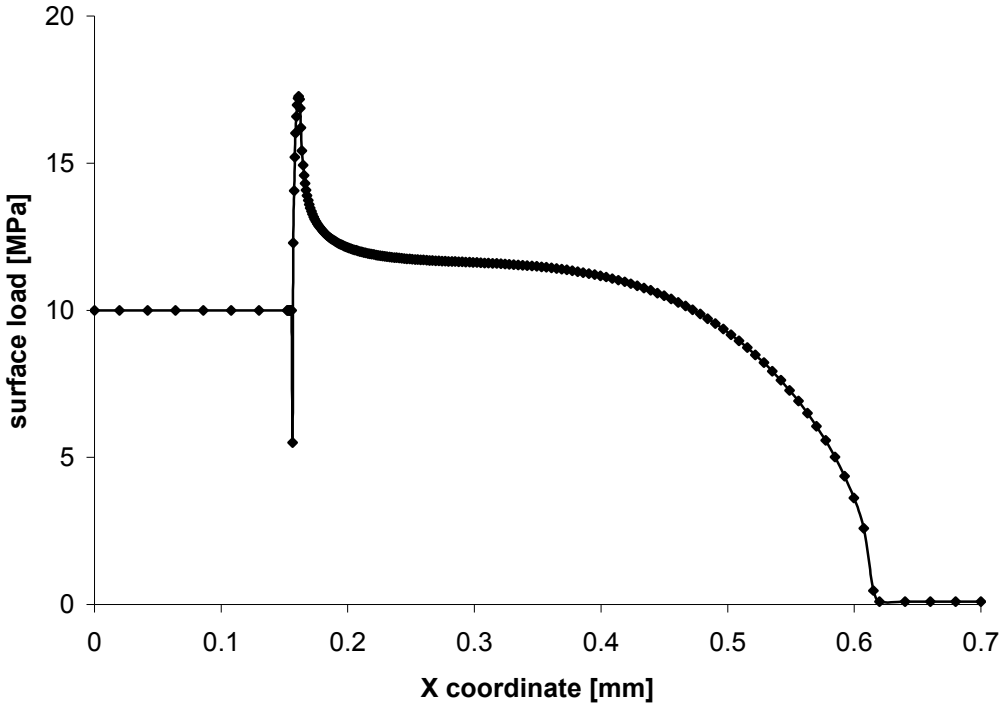

Figure 3.13: Static surface loads on the seal.

3.6.6 Integration with Other Analysis

Since the deformation analysis is performed in *ANSYS* and all others are done in the Compaq Visual Fortran environment. There exists the problem of how to integrate

them together. Depending on whether these are done simultaneously or not, there are two methods: online method and influence coefficient method.

3.6.6.1 Online Method

The online method is just straightforward. Figure 3.14 shows the flowchart. The main program is written in *FORTRAN*. During every iteration, when it goes to the deformation analysis step, *ANSYS* is called and run at background in batch mode. The fluid pressure and frictional stress are read in from the output file of the fluid mechanics analysis and used to define the loads at the sealing zone. When the deformation analysis is finished, the contact nodes coordinates and contact pressure are written to an output file. They are then imported by *Compaq Visual Fortran* and used in the succeeding analysis. This process iterates until the change in fluid pressures is less than a given criteria and the computation is converged.

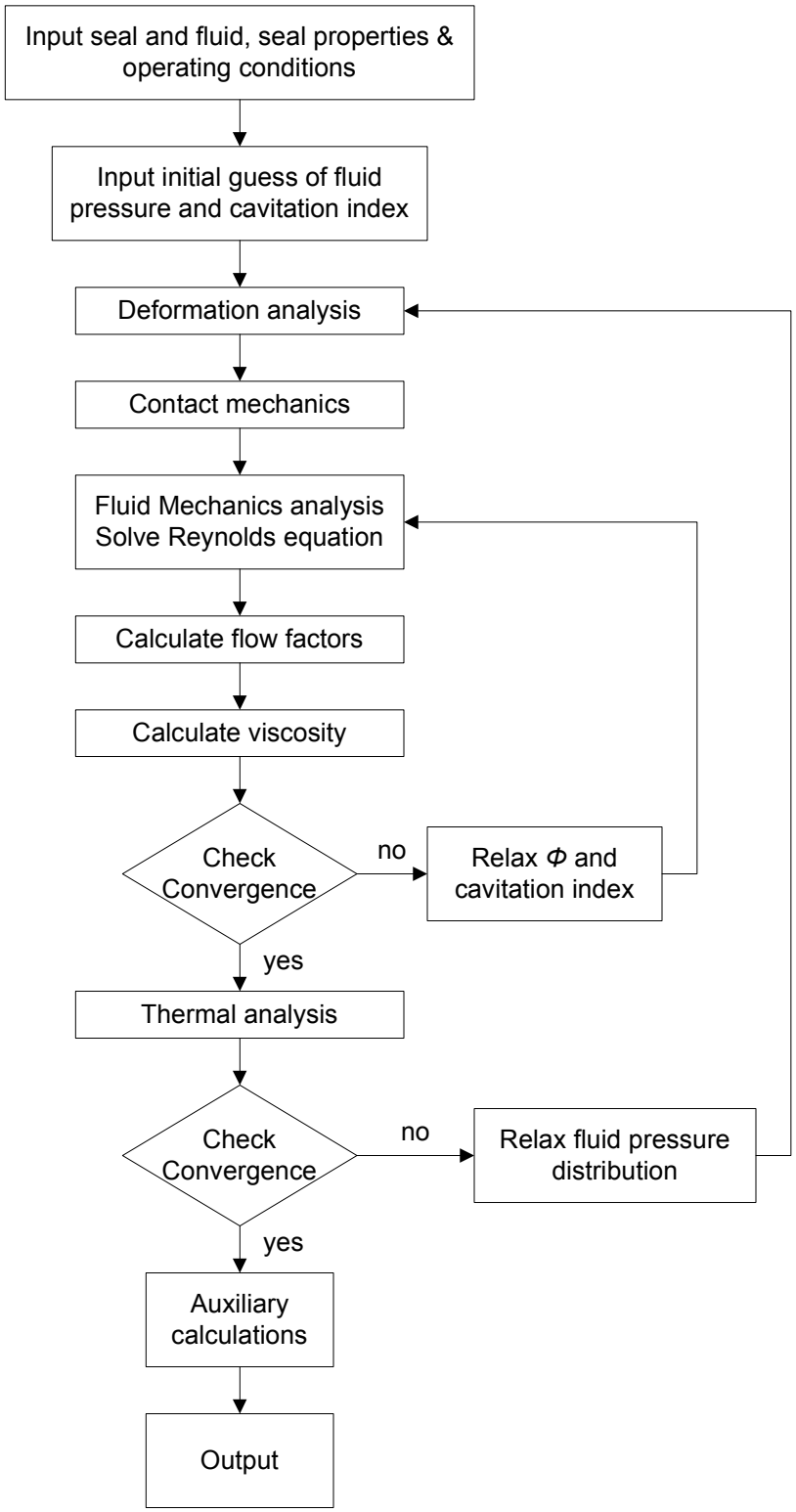

Figure 3.14: Computational procedure for single lip seal using online method.

3.6.6.2 Influence Coefficient Method

The pros of online method are its accuracy and as it is running in the *ANSYS* environment, a non-linear material model can be utilized. However its cons are also significant. At high sealed pressure or high speeds, it takes a very long time to converge, which is sometimes intolerable.

It's observed that during the deformation analysis, the frictional stress load has very little effect on the contact pressure. Figure 3.15 shows the comparison of contact pressure with and without frictional stress load for the base case during outstroke.

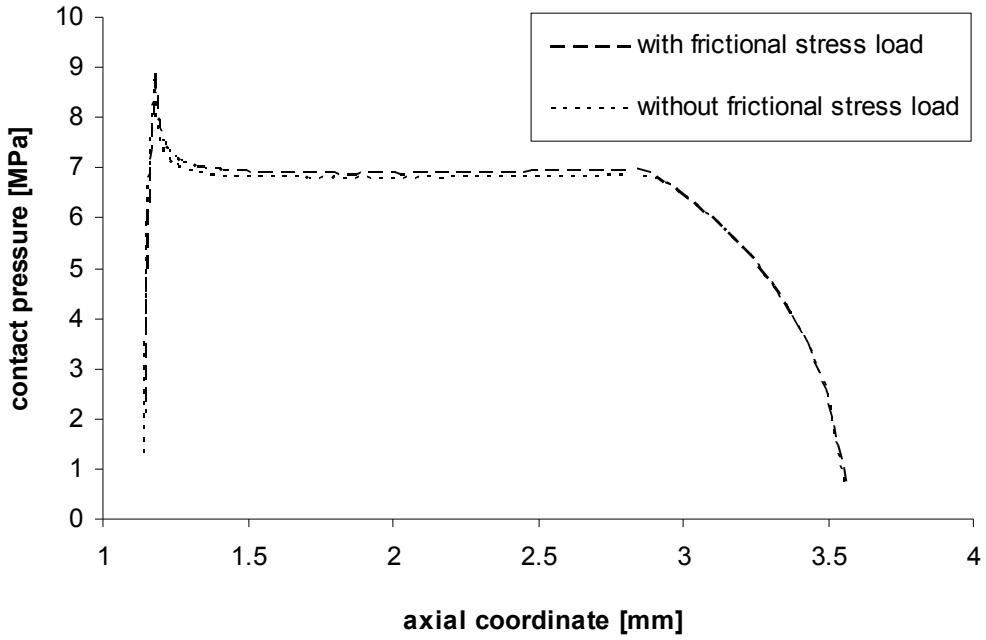

Figure 3.15: Comparison of contact pressure with and without frictional stress load.

Also since the variation of film thickness is significantly smaller than the dimension of the seal itself, according to small deformation theory, it is recognized that in the sealing zone, the deformation at any location is proportional to the forces applied at

every location. Thus, in discretized form with n axial nodes across the sealing zone, the film thickness at the i^{th} node can be expressed as,

$$H_i = H_s + \sum_{k=1}^{n} (I_1)_{ik} (P_t - P_{sc})_k \tag{3.36}$$

The proportionality factors $(I_1)_{ik}$, the "influence coefficients," are computed off-line using *ANSYS*. Figure 3.16 shows a typical distribution of the influence coefficients. The pressure P_t is the sum of the fluid and contact pressures. P_{sc} is the static contact pressure distribution, computed off-line with the same finite element code used to obtain the influence coefficients. Thus, with this "influence coefficient method", the model contains only linear algebraic equations.

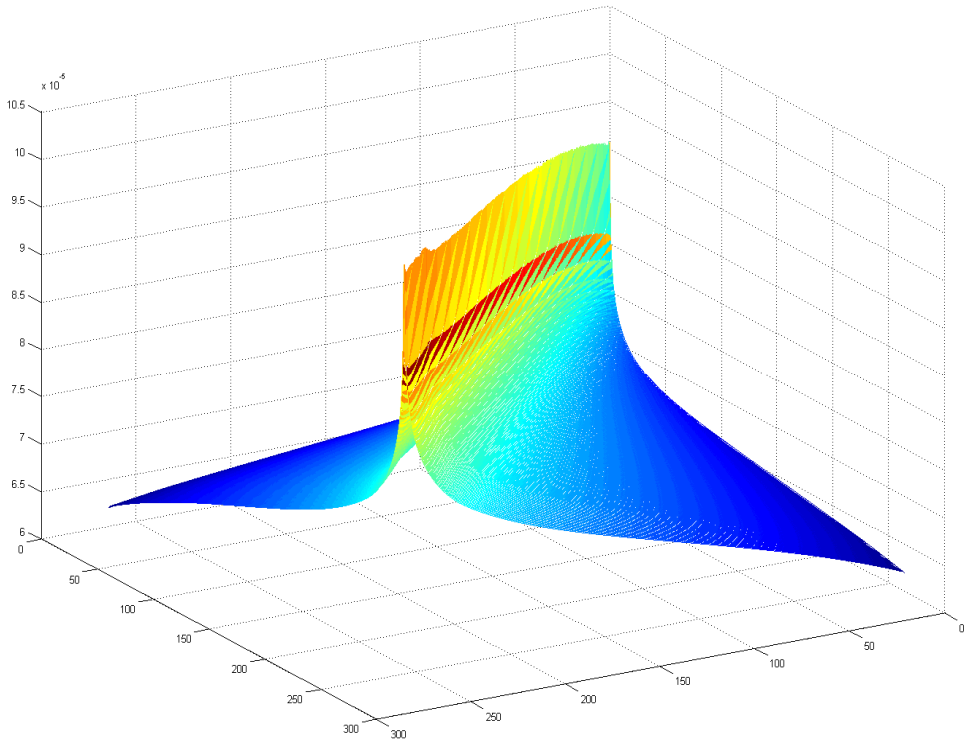

Figure 3.16: Influence coefficients for the deformation analysis

Figure 3.17 shows the computational procedure for a single lip seal using influence coefficient method, which is different from that of the on-line method. First, input the seal properties, fluid properties and operating conditions, initial guesses of the film thickness and cavitation index as well as the influence coefficients and static contact pressure. The fluid mechanics analysis is then performed to yield the fluid pressure distribution. Next, the contact mechanics analysis is performed to yield the contact pressure distribution. Based on this contact pressure distribution and the fluid pressure distribution, the normal deformation of the seal is computed, and then the film thickness distribution is updated. Iteration continues until the solution converges. Auxiliary calculations yield the flow rate and frictional shear stress.

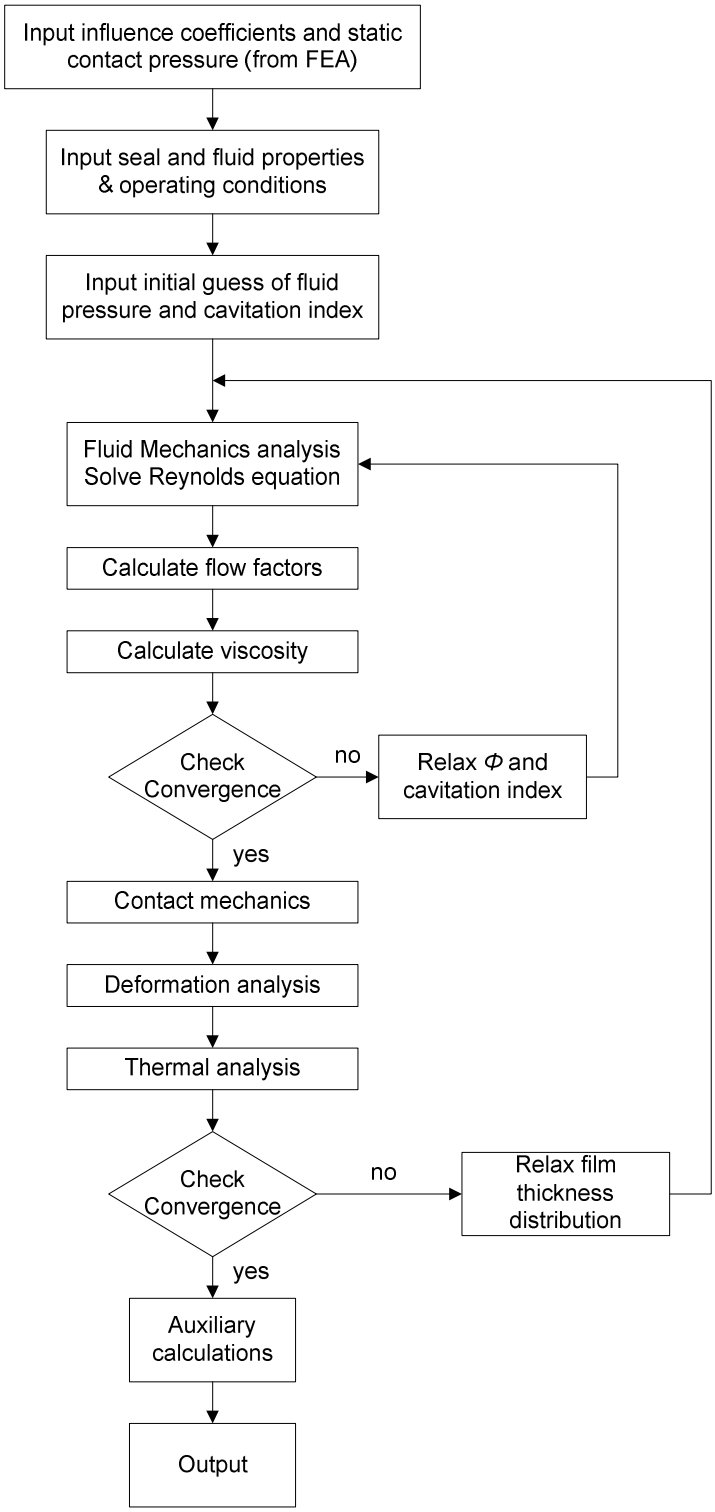

Figure 3.17: Computational procedure for single lip seal using influence coefficient method.

3.7 Computational Scheme

Since the fluid mechanics analysis, the contact mechanics analysis, the structural deformation analysis, and the thermal analysis are all strongly coupled, an iterative computation procedure is required.

For both the pressure iteration and film thickness iteration, relaxation technique is used to solve the instability problem. A proper relaxation coefficient is found by trial and error method since normally it is dependent on operation conditions and seal surface characteristics.

When the relative change at any node is smaller than a given criterion, iteration is considered to be converged. The value of 1×10^{-3} is used for both the pressure loop and film thickness loop.

As the online method is extremely time consuming, it is only applied to the analysis of the seals with simple geometry at base case, such as the single lip seal, O-ring and the step seal. For the seal with double lip or with surface pattern or the tandem seal, the influence coefficient method is implemented.

3.8 Results

Computations have been performed for a typical hydraulic rod seal used in an injection molding application. For this application, different from the conventional hydraulic cylinder, the sealed pressure is same for outstroke and instroke [85].

The base parameters for which computations have been performed are shown in Table 3.1.

Table 3.1: Base parameters of the single lip U-cup seal.

Seal	Hallite U-cup
Seal material	polyurethane
Elastic modulus, E	43 MPa
Poisson's ratio, ν	0.499
Thermal conductivity - rod	46 W/m-K
Thermal conductivity - seal	0.25 W/m-K
Sealed pressure, P_{sealed}	6.90 MPa (1000 psi)
Rod diameter, D	88.9 mm (3.5")
Stroke length	1.93 m (76")
Speed – outstroke, U	0.635 m/s (25 in/s)
Speed – instroke, $-U$	0.813 m/s (32 in/s)
Sealed fluid	Mobil DTE 25 oil
Viscosity	0.0387 Pa-s at 40 ^{o}C 0.0167 Pa-s at 66.5 ^{o}C 0.0058 Pa-s at 100 ^{o}C
Pressure-viscosity coefficient, α	20 x 10^{-9} Pa^{-1}
Asperity radius, R	4 μm
RMS roughness, σ	0.8 μm
Asperity density, η	4x10^{11} m^{-2}
Sealing zone length, L	2.5 mm
Asperity contact friction coefficient, f	0.25
Aspect ratio, γ	1

3.8.1 Leakage and Friction

Figure 3.18 shows the computed fluid transport per stroke versus seal roughness. All parameters other than the seal roughness are equal to the base values. Both the outstroke and instroke transports increase almost linearly with roughness. For zero net leakage per cycle, the outstroke transport must be less than the potential instroke transport. From the Figure 3.18 it is seen that this occurs when the roughness is below a critical roughness, in this case 1.37 μm. Above this critical value, the larger the roughness, the larger would be the leakage. This critical roughness is dependent on the seal design

and operating conditions as well as the surface characteristics such as asperity density and radius.

For this base seal, the volume of fluid carried out during the outstroke is computed as 0.337 cm^3/stroke, while the volume the seal is capable of drawing back in during the instroke, is computed as 0.516 cm^3/stroke. Since the latter exceeds the former, there is no net leakage during a cycle, and one could say that this seal does not leak.

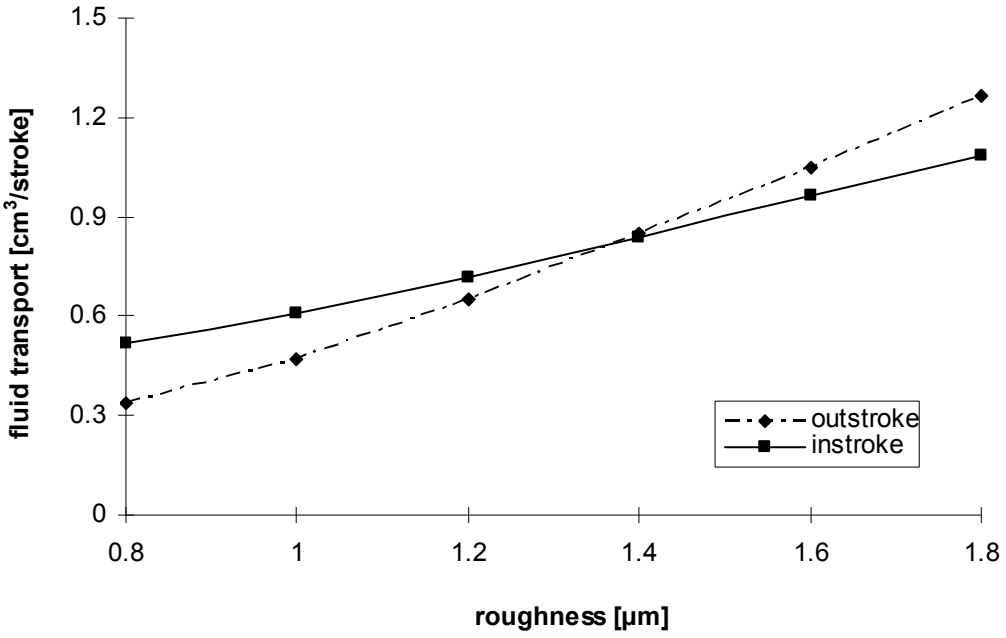

Figure 3.18: Computed fluid transport per stroke vs. seal roughness.

Since the viscosity of hydraulic fluid varies with temperature, the heat generation due to friction needs to be considered. The average temperature of the contact surface goes up for about 3 degrees in an injection molding application. Also the temperature gets higher as the rod speed increases. The thermal effect slightly influences the performance of the seal, which makes the net leakage a little bit larger.

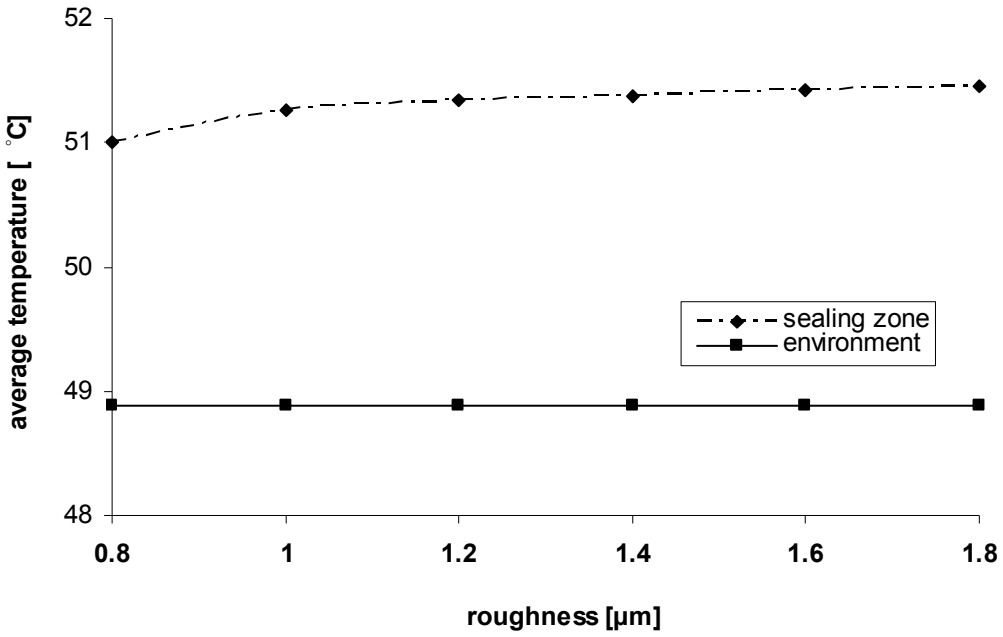

Figure 3.19: Average temperature vs. seal roughness.

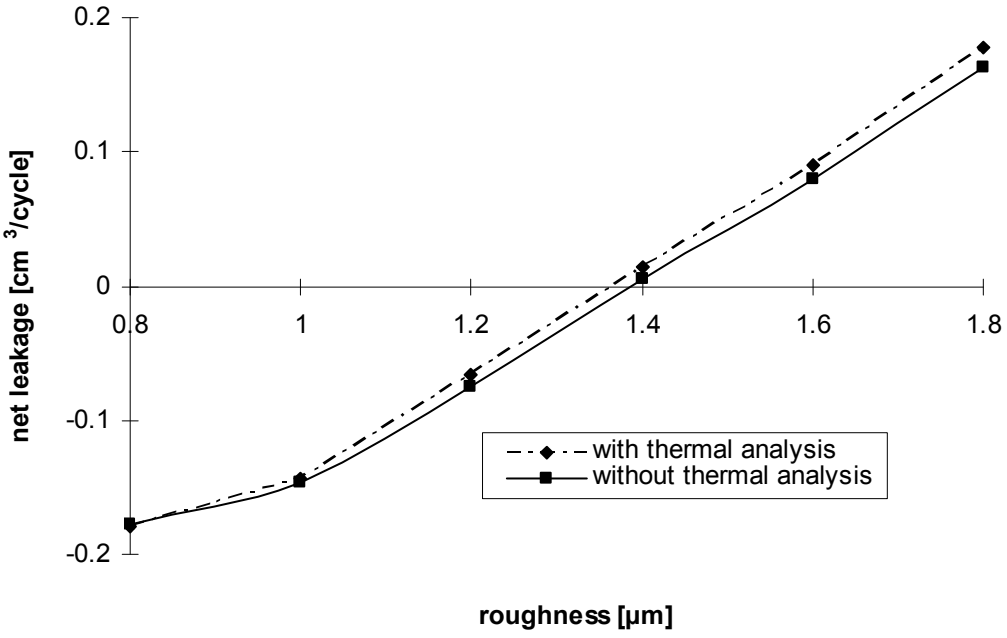

Figure 3.20: Net leakage vs. seal roughness.

The friction force on the rod as a function of seal roughness is shown in Figure 3.21. As can be seen, the friction force can be quite high, on the order of a kilo Newton. These computed values are comparable to those measured by the seal manufacturer. It is interesting to note that the friction force decreases with increasing surface roughness for the outstroke while the opposite trend is found for instroke. The reason will be discussed below.

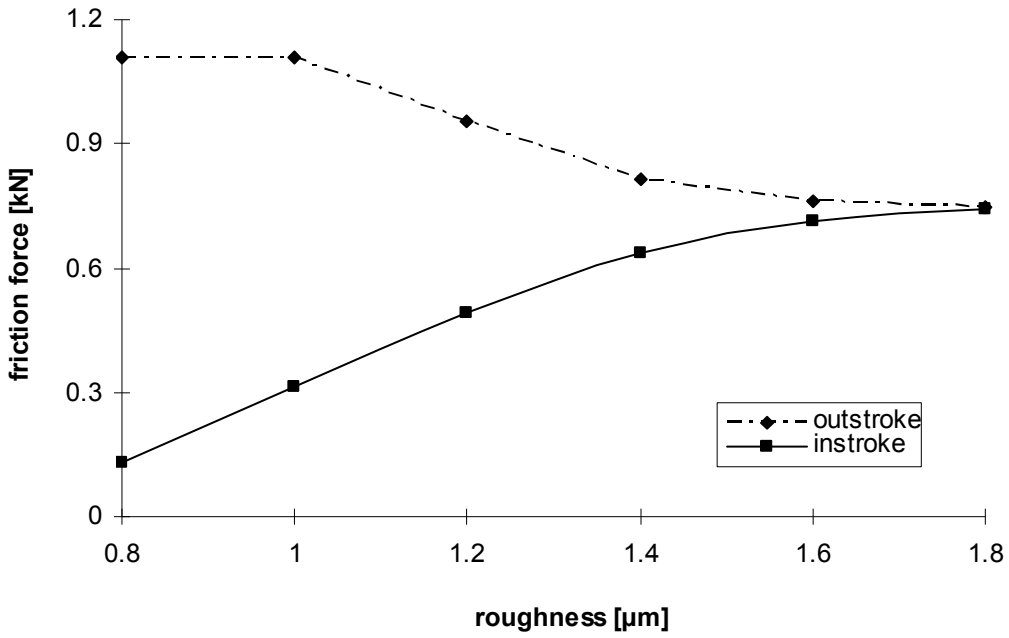

Figure 3.21: Friction force on the rod vs. seal roughness.

3.8.2 Details of Sealing

Figure 3.22 shows the film thickness distribution for the outstroke and the instroke for the base case, 0.8 µm. Since significant asperity contact occurs when the film

thickness is less than 3σ (for the base seal, less than 2.4 μm), it is clear that during the outstroke and the instroke the entire sealing zone experiences mixed lubrication. Thus it is clear that the assumption of full film lubrication in previous models is not justified. It is also noted that during the instroke the film thickness is larger than that during the outstroke. This has an important implication regarding leakage, as will be discussed.

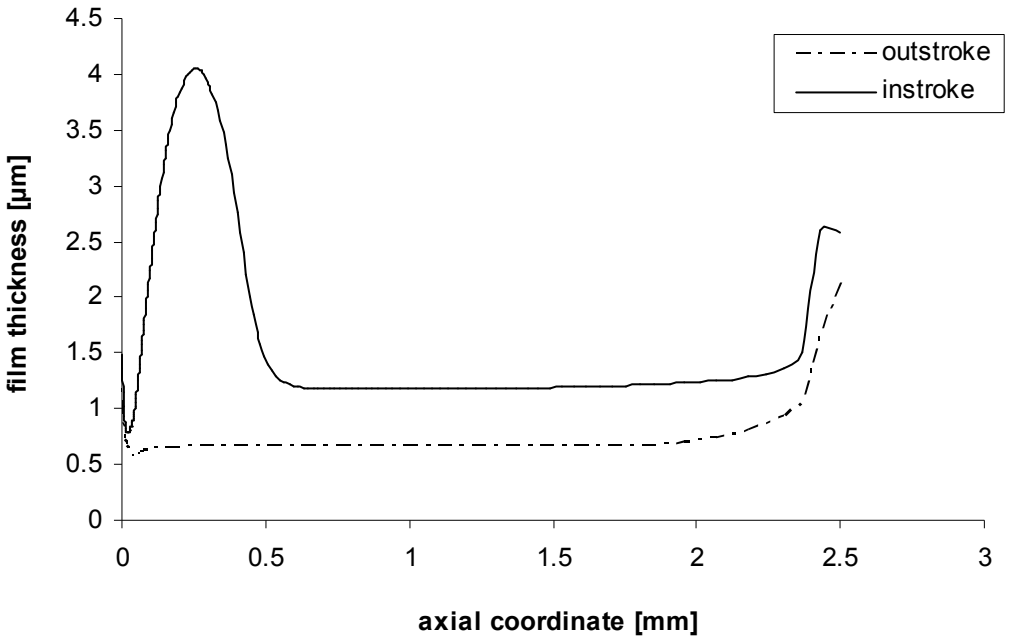

Figure 3.22: Film thickness distributions, 0.8 μm roughness.

The pressure distributions in the sealing zone for the outstroke are shown in Figure 3.23. As can be seen, the contact pressure distribution has a steep slope near the liquid side of the zone and a more gradual slope near the air side.

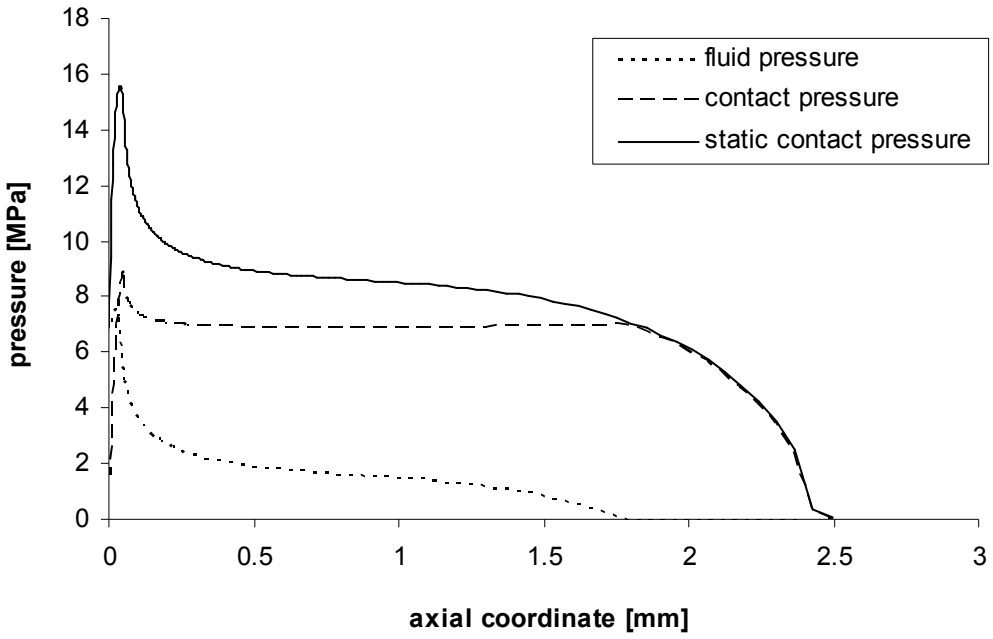

Figure 3.23: Pressure distributions - outstroke, 0.8 μm roughness.

Hydrodynamic pressure generation causes the fluid pressure to be elevated near the liquid side of the zone, slightly lifting the seal away from the rod. This reduces the contact pressure below its static value in that region. However, over almost a quarter of the sealing zone, near the air side, the fluid is cavitated (zero pressure), and therefore the contact pressure equals its static value.

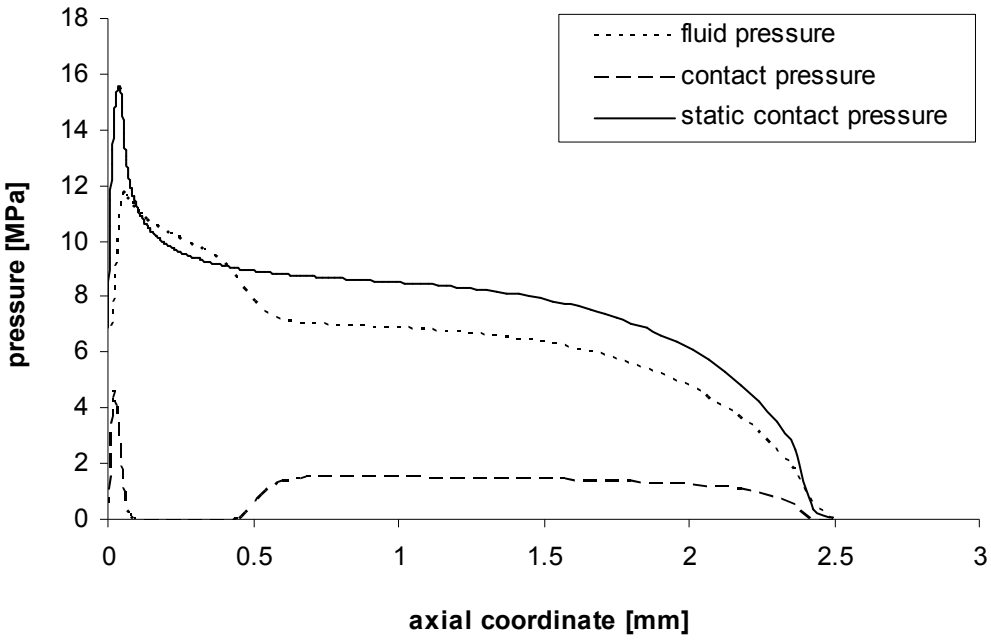

Figure 3.24: Pressure distributions - instroke, 0.8 μm roughness.

Figure 3.24 shows the pressure distributions for the instroke. There is significantly more hydrodynamic pressure generation than during the outstroke. However, there is still a non-zero contact pressure and mixed lubrication.

The frictional shear stress on the rod is shown in Figure 3.25. As would be expected, it is in opposite directions for the instroke and the outstroke. The peak stresses are near the liquid side of the sealing zone, where the contact pressures are highest.

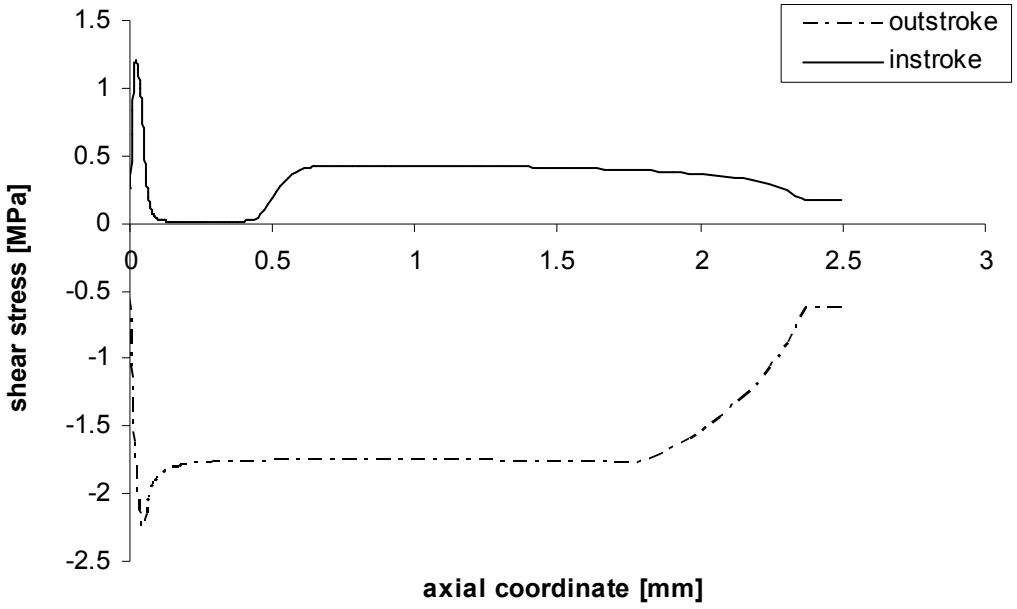

Figure 3.25: Frictional shear stress on the rod distributions, 0.8 μm roughness.

Figure 3.26 is a plot of fluid transport vs. rod speed for the base case seal with 0.8 μm roughness and for a similar seal with 1.6 μm roughness. This type of plot would be very useful when designing or selecting a seal, since it shows the combinations of roughness and rod speeds which would result in a non-leaking seal. The arrows denote the seal operating points at the base rod speeds. As seen on this plot, as well as on the plot in Figure 3.18, the 0.8 μm roughness seal is non-leaking while the 1.6 μm roughness seal leaks. To eliminate leakage from the latter seal, the rod speeds would have to be raised considerably, to values above 1 m/s.

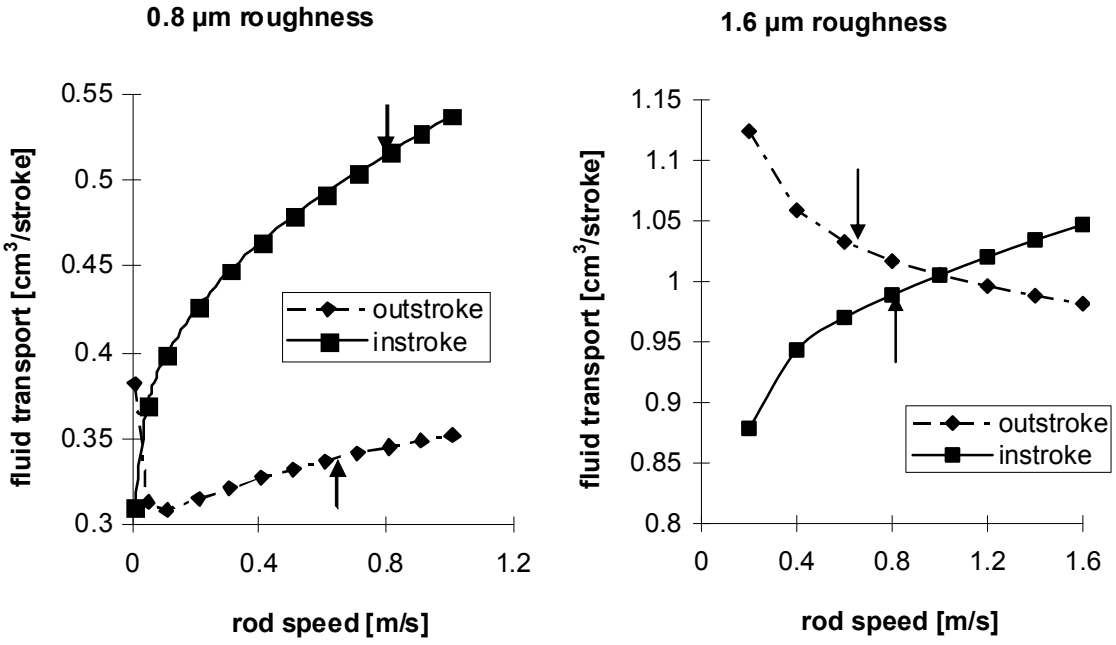

Figure 3.26: Fluid transport vs. rod speed.

To understand the sealing process, it is useful to examine the details of the sealing zone for two seals, a non-leaking seal with a roughness of 0.8 µm and a leaking seal with a roughness of 1.6 µm. The fluid transports for the two seals under the base operation condition are shown in Table 3.2. Note that increasing the roughness to 1.6 µm, increases the volume of fluid carried out during the outstroke relative to that carried in during the instroke, such that the former exceeds the latter, leading to net leakage. The causes of this change can be seen by examining the pressure and film thickness distributions for the 1.6 µm roughness seal, Figure 3.27 to Figure 3.29, and comparing them with the corresponding distributions for the 0.8 µm roughness seal.

Table 3.2: Comparison between leaking & non-leaking seals.

	1.6 μm roughness seal leaking	0.8 μm roughness seal non-leaking
fluid transport - outstroke	1.051 cm^3/stroke	0.337 cm^3/stroke
fluid transport - instroke	0.961 cm^3/stroke	0.516 cm^3/stroke

Figure 3.27 shows the film thickness distributions for the leaking seal. For the non-leaking seal, the film thickness is larger during the instroke than during the outstroke. This is a favorable characteristic because it allows comparatively more fluid to be drawn back into the cylinder during the instroke. For the leaking seal, the film thicknesses are about equal during the instroke and outstroke, a less favorable condition than for the non-leaking seal. This is because the fluid pressure and contact pressure distributions, which determine the film thickness distribution, are almost identical for the instroke and outstroke, as discussed below in connection with Figure 3.28 and Figure 3.29.

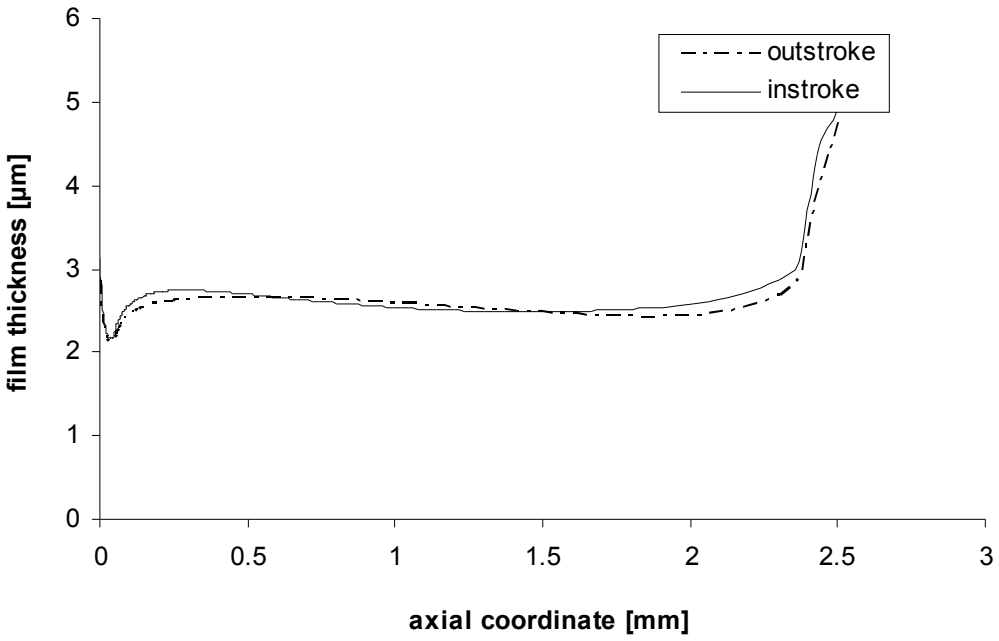

Figure 3.27: Film thickness distributions, 1.6 µm roughness.

Figure 3.28 shows the pressure distributions during the outstroke for the leaking seal. The static contact pressure distributions are the same as the non-leaking seal, with a peak close to the liquid side and a steeper slope on the liquid side than on the air side. The full film lubrication models, would predict zero leakage for both seals, while it has been shown that the seal with 1.6 µm roughness does indeed leak.

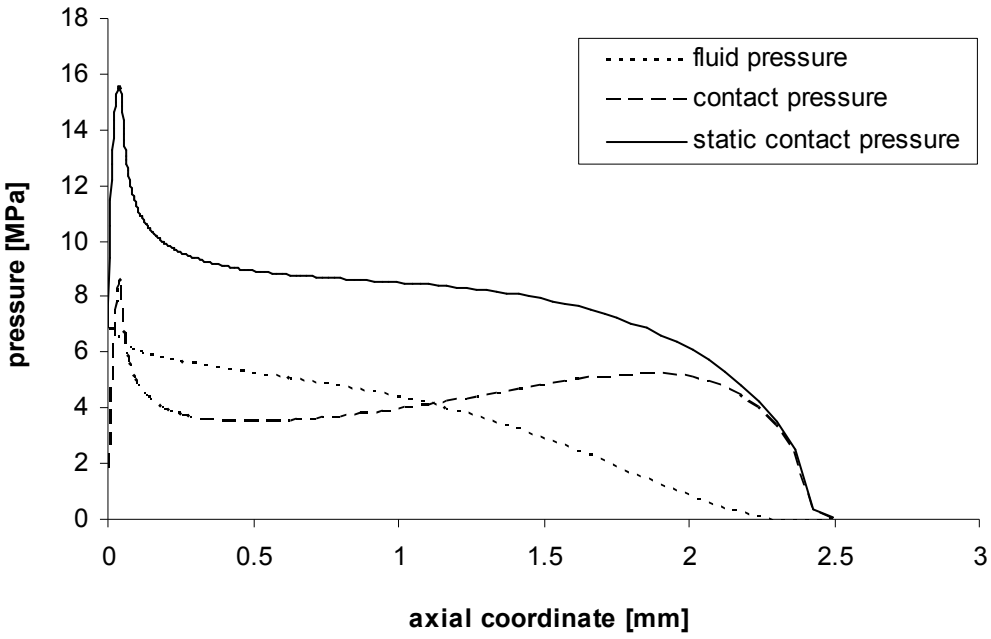

Figure 3.28: Pressure distributions - outstroke, 1.6 μm roughness.

For the non-leaking seal, the fluid pressure is zero over more than a quarter of the sealing zone. The fluid is cavitating in this region. This is a favorable characteristic since cavitation tends to restrict the flow out of the cylinder. For the leaking seal the cavitation region has almost eliminated, a less favorable condition. Due to the increased roughness of the leaking seal, the film thickness is so large as to virtually eliminate the hydrodynamic effect on fluid pressure, so that the fluid pressure distribution is almost linear, decreasing from the sealed pressure on the liquid side to ambient on the air side. Since the net force produced by the linear fluid pressure distribution on the leaking seal is larger than that produced by the fluid pressure distribution on the non-leaking seal, the contact pressures on the leaking seal are lower than those on the non-leaking seal, as seen

in Figure 3.24. Thus, as the surface roughness increases, the contact force and the friction force decrease, as discussed earlier.

The corresponding pressure distributions during the instroke are shown in Figure 3.29. The cavitation in both seals has been eliminated. During the instroke cavitation is undesirable because it restricts the amount of fluid that can flow back into the cylinder. Comparing Figure 3.29 with Figure 3.28, it is interesting to note that the fluid pressure and contact pressure distributions are almost the same for the instroke and outstroke of the leaking seal. As mentioned above in connection with Figure 3.28, the increased roughness of the leaking seal produces a film thickness so large as to virtually eliminate the hydrodynamic effect on the fluid pressure distribution. Therefore the fluid distribution is almost linear (and therefore almost identical) during both instroke and outstroke, and hence the contact pressure distributions are almost identical.

Figure 3.30 shows the frictional shear stress on the rod at 1.6 μm case. Compared with Figure 3.25, the frictional stress is smaller during outstroke and larger during instroke than the 0.8 μm case, which is consistent with the contact pressure and film thickness variation. This is because the shear stress due to contacting asperities accounts for the majority of the frictional shear stress and it is directly related to contact pressure by an empirical friction coefficient. Since the friction force on the rod is computed by integrating the frictional shear stress in the sealing zone, the variation of frictional shear stress with seal roughness explains why the friction force decrease with increasing surface roughness for the outstroke while the opposite trend is found for the instroke.

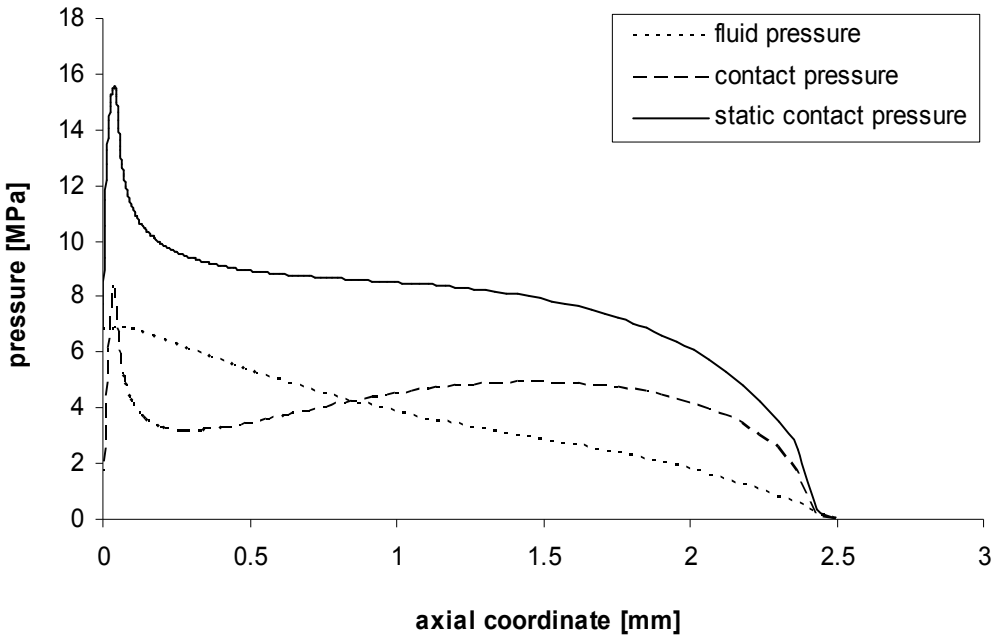

Figure 3.29: Pressure distributions - instroke, 1.6 μm roughness.

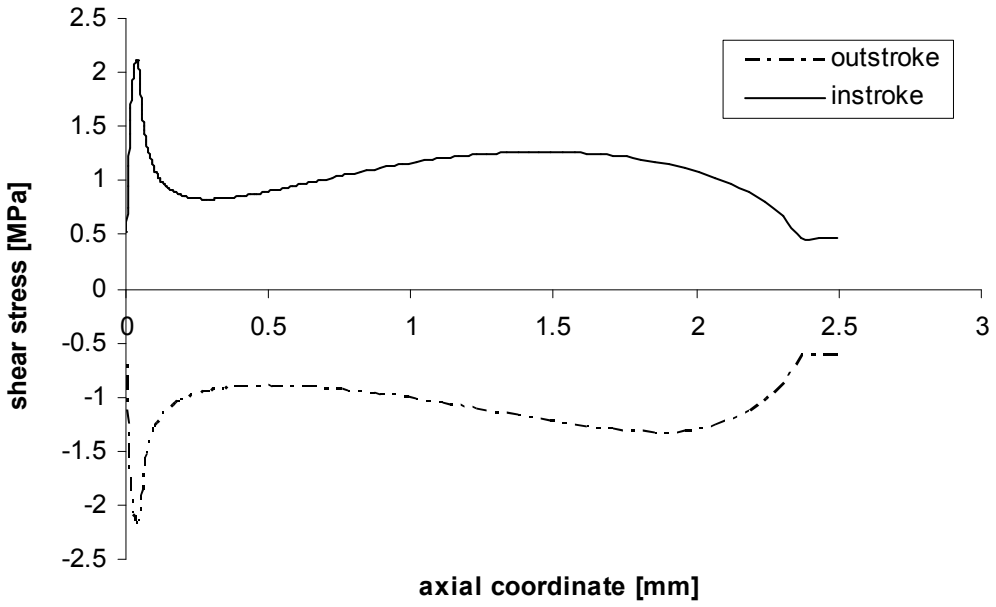

Figure 3.30: Frictional shear stress on the rod distributions, 1.6 μm roughness.

3.9 Conclusions and Discussions

The results of this study indicate that the rod seal operates with mixed lubrication in the sealing zone, and seal roughness plays an important role in determining its behavior. There is a critical seal roughness, below which the seal will be non-leaking, above which the seal will leak. A larger film thickness during outstroke compared to that during instroke promotes non-leaking. Cavitation during outstroke also promotes non-leaking.

CHAPTER 4

DOUBLE LIP SEAL, TANDEM SEAL AND POSSIBLE IMPROVEMENTS

4.1 Introduction

While many seals only have a single lip, there are some seals which have two lips. The secondary lip is intended to act as a second line of defense, as well as a bearing. It is important to understand the behavior of such a double lip seal, and how that behavior differs from that of a single lip seal.

Figure 4.1 contains a schematic of a typical reciprocating rod seal with double lips.

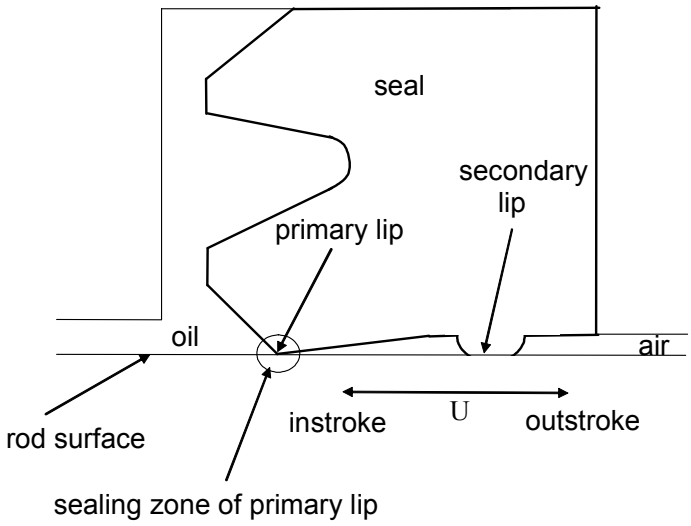

Figure 4.1: Schematic of double lip seal.

4.2 Analysis

In the previous chapter a seal with only the primary lip is analyzed using a model consisting of a fluid mechanics analysis, a contact mechanics analysis, a deformation analysis, a thermal analysis and an iterative computational procedure. In the present section a similar approach is applied to each lip, all the assumptions are the same as the previous chapter.

There are two primary differences between the analyses of the double lip and single lip cases [86], which complicate the double lip model. First, under steady state conditions (which are assumed), the mass flow rate past the two lips must be the same for the double lip seal, a restriction absent for the single lip seal. Second, the boundary conditions on the fluid in the sealing zone are different. For the single lip seal, the fluid pressure at the inner boundary (liquid side) is equal to the sealed pressure while that at the outer boundary (air side) is equal to the ambient pressure. These pressures are known a priori. For the double lip seal, boundary conditions must be applied to both lips. For the primary lip, the fluid pressure at the inner boundary is again equal to the sealed pressure, but that at the outer boundary is equal to the pressure in the interlip region (see Figure 4.1), provided the fluid is not cavitated. For the secondary lip, the fluid pressure at the inner boundary is also equal to the pressure in the interlip region, provided the fluid is not cavitated, while that at the outer boundary is equal to the ambient pressure. If the fluid in and near the interlip region is cavitated, then the average fluid density at the outer boundary of the primary lip must be equal to that at the inner boundary of the secondary lip. It should be noted that the conditions in the interlip region are not known a priori, and

must be determined in the course of the analysis. From these considerations it is clear that the behavior of the two lips in a double lip seal are coupled.

As discussed above, the boundary conditions on the Reynolds Equation for the single lip seal is replaced by eq. (4.1) for the primary and secondary lips of the double lip seal.

$$\begin{aligned} \phi_{primary} &= P_{sealed} \quad at\ \hat{x} = 0 \\ &= \phi_{interlip} \quad at\ \hat{x} = 1 \end{aligned} \tag{4.1}$$

Also as discussed above, the mass the flow rates through the sealing zones of the two lips must be equal.

$$\hat{q}_{primary} = \hat{q}_{secondary} \tag{4.2}$$

It should be noted that the two lips are also coupled through the deformation characteristics of the seal. Similar to the analysis of the single lip seal, the influence coefficients and static contact pressure distribution for each lip is obtained from a finite element structural analysis. One of the boundary conditions in that analysis involves the fluid pressure/density in the interlip region, which is jointly determined by the action of both lips.

This last form of coupling requires special treatment since the finite element analysis is done off-line and the interlip pressure/density is not known a priori. A series of finite element analyses are therefore performed for a number of specified discrete interlip pressures spanning the expected range. Depending on the computed interlip pressure/density, the appropriate finite element solution for the static contact pressure distribution and the influence coefficients is used in the iterative computation.

4.3 Computational Scheme

The computational procedure is shown in Figure 4.2. For a double lip seal, the analysis of each lip is the same as that of the single lip seal, which is explained in previous chapter. However, the inter seal pressure in the region between the two seals is unknown and must be determined by requiring the flow rates past the two seals to be the same. So an additional loop is required for double lip seal.

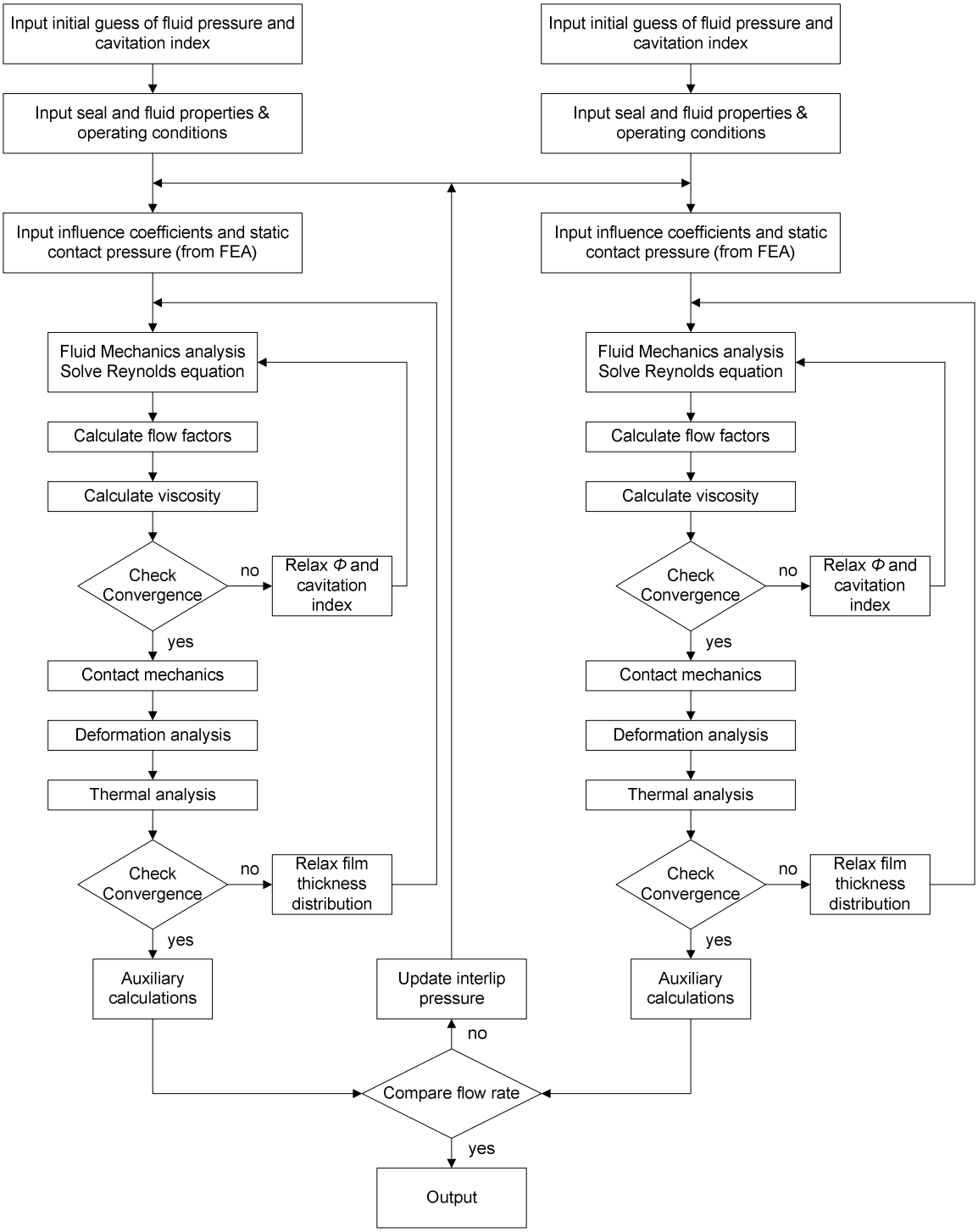

Figure 4.2: Computational procedure.

4.4 Results

Computations have been performed for a typical double lip seal with the same base parameters as the single lip seal, which are shown in Table 3.1.

The presence of the secondary lip can significantly change the geometry of the primary lip due to its effect on the pressure in the interlip region (discussed below). For example with a roughness of 1.6 μm, the length of the primary lip sealing zone is approximately 0.8 mm during an outstroke while it is approximately 1.7 mm during an instroke. Thus, while with a single lip seal there is no significant difference in the sealing zone length for an outstroke and an instroke, with a double lip seal, there are such differences for both the primary and secondary lips.

The interlip pressure is shown as a function of roughness in Figure 4.3. For the outstroke, as the roughness is decreased from a value of $\sigma = 1.8$ μm, the interlip pressure increases until it reaches a maximum of 6.4 MPa (compared to the sealed pressure of 6.9 MPa) at a roughness of $\sigma = 1.6$ μm, whereupon it decreases rapidly with a further reduction in roughness. Conversely, for the instroke, the fluid in the interlip region always cavitates.

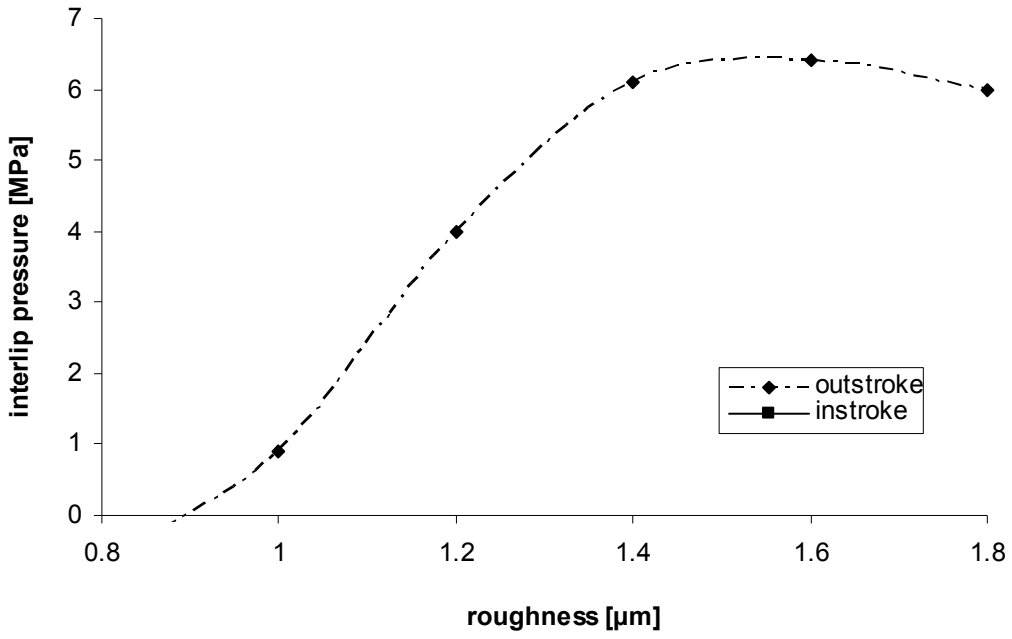

Figure 4.3: Interlip pressure vs. roughness.

4.4.1 Leakage and Friction

Figure 4.4 contains a plot of the fluid transport during instroke and outstroke versus roughness for the double lip seal. As discussed earlier, for zero net leakage, the instroke fluid transport must exceed the outstroke transport. This occurs at values of roughness of approximately 1.08 µm, which is much smaller than that of single lip seal, 1.37 µm. This means from the sealability point of view, the double lip seal is inferior to single lip seal.

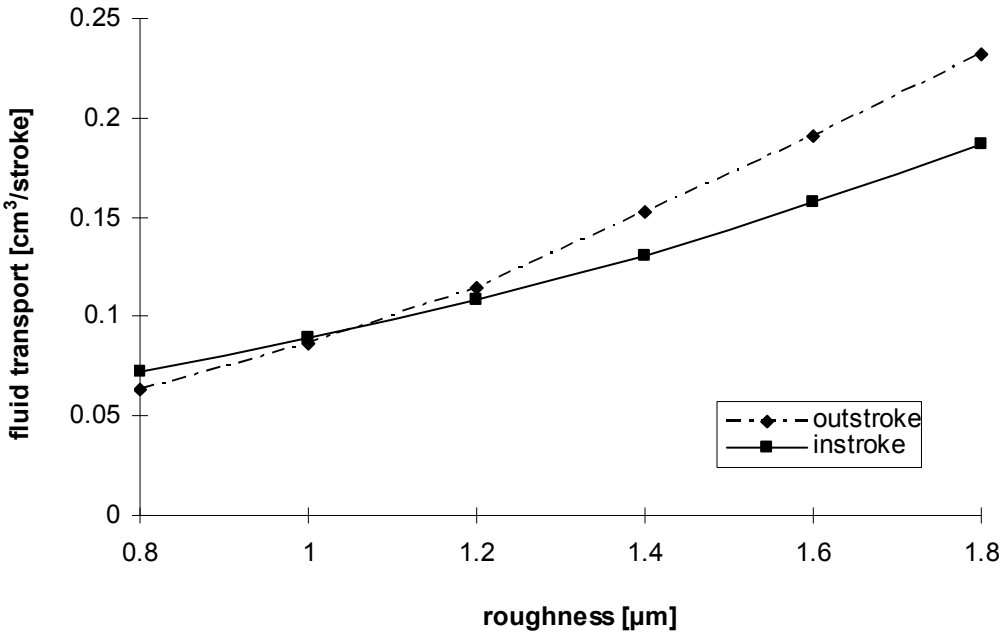

Figure 4.4: Fluid transport vs. roughness.

The frictional behavior of double lip seal is also of interest. Figure 4.5 shows the frictional force, due to both asperity contact friction and viscous friction, vs. *RMS* seal roughness for the double lip seal. Comparing with Figure 3.21, depending on the *RMS* roughness, this can be double that of a single lip seal.

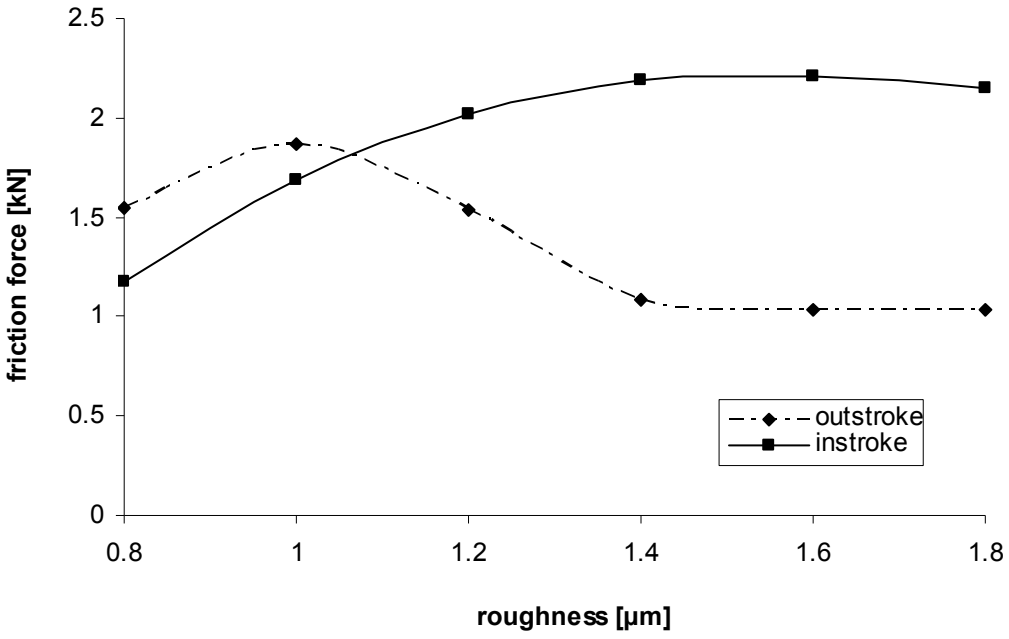

Figure 4.5: Friction force vs. roughness.

4.4.2 Details of Sealing

Figure 4.6 to Figure 4.11 describe the behavior of the double lip seal with a roughness of 0.8 µm, a non-leaking seal under the base conditions. The film thickness distributions of the primary lip, Figure 4.6 shows that the lip operates with mixed lubrication since the thicknesses are always less than 3σ. It should also be noted that the film thickness during the instroke exceeds that during an outstroke, which is a characteristic that promotes non-leakage. However the lengths of the sealing zone during outstroke and instroke are the same. This is not surprising, since Figure 4.3 indicates the pressure in the interlip region is the virtually the same for both strokes.

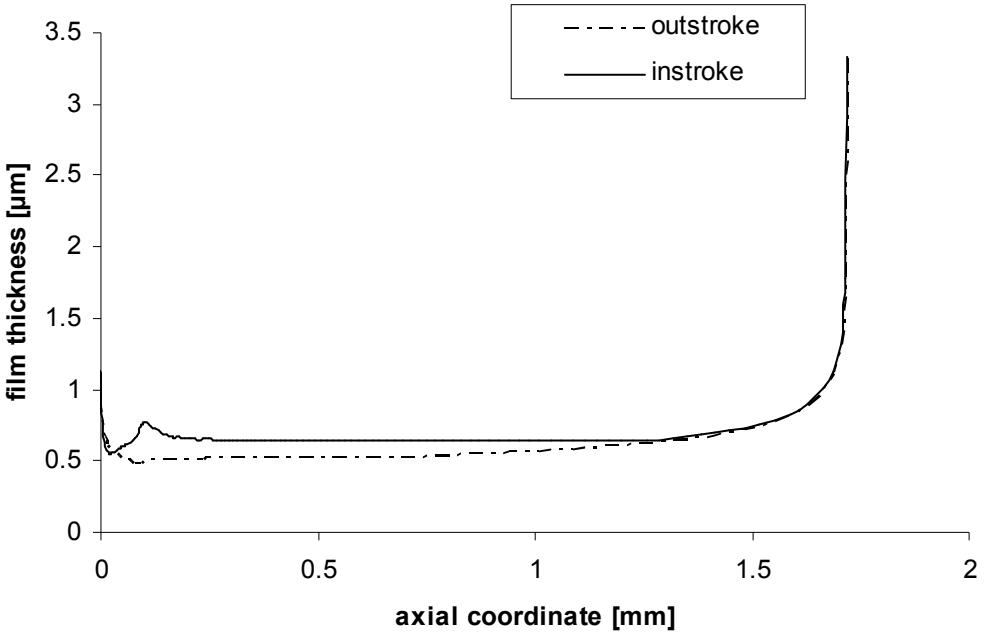

Figure 4.6: Film thickness distributions - primary lip, 0.8 µm roughness.

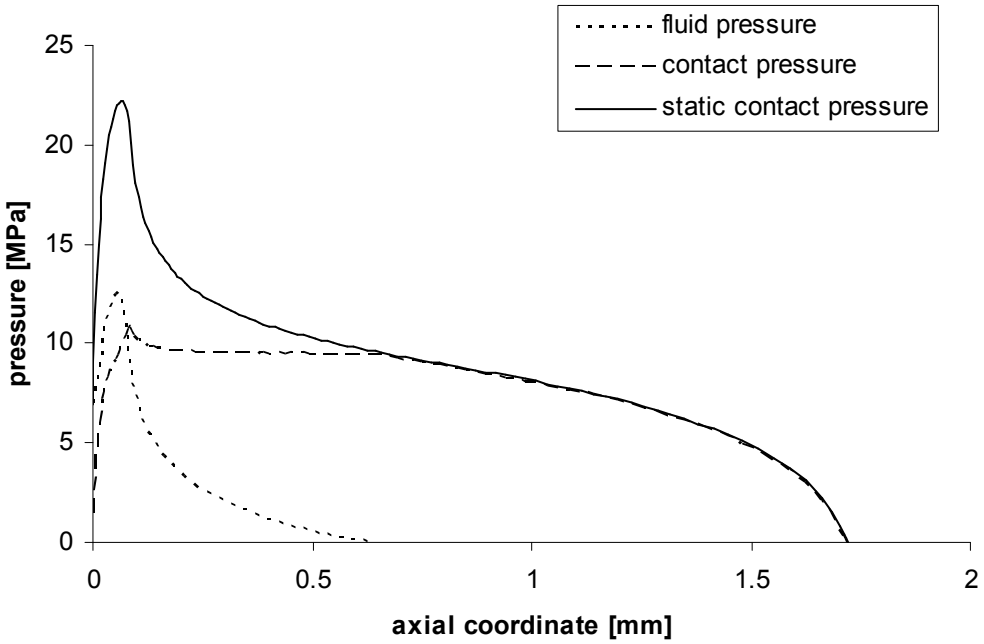

Figure 4.7: Pressure distributions - primary lip, outstroke, 0.8 µm roughness.

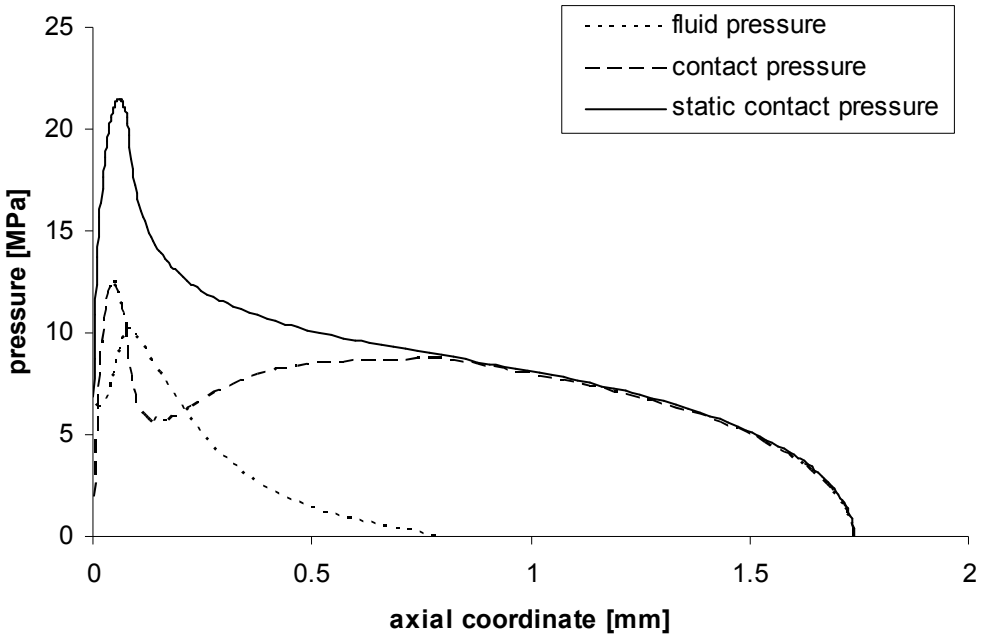

Figure 4.8: Pressure distributions - primary lip, instroke, 0.8 μm roughness.

The fluid pressure, contact pressure and static contact pressure distributions of the primary lip for the outstroke are shown in Figure 4.7. From the fluid pressure distribution it is clear that the fluid cavitates over most of the sealing zone, again a characteristic that promotes non-leakage since the cavitation restricts the outflow of fluid. The corresponding figure for the instroke, Figure 4.8, shows only a very small portion of the sealing zone cavitating. This, too, promotes non-leakage since the lack of cavitation during the instroke allows greater transport of fluid inward. These primary lip characteristics are very similar to those of a comparable single lip seal in a non-leaking condition.

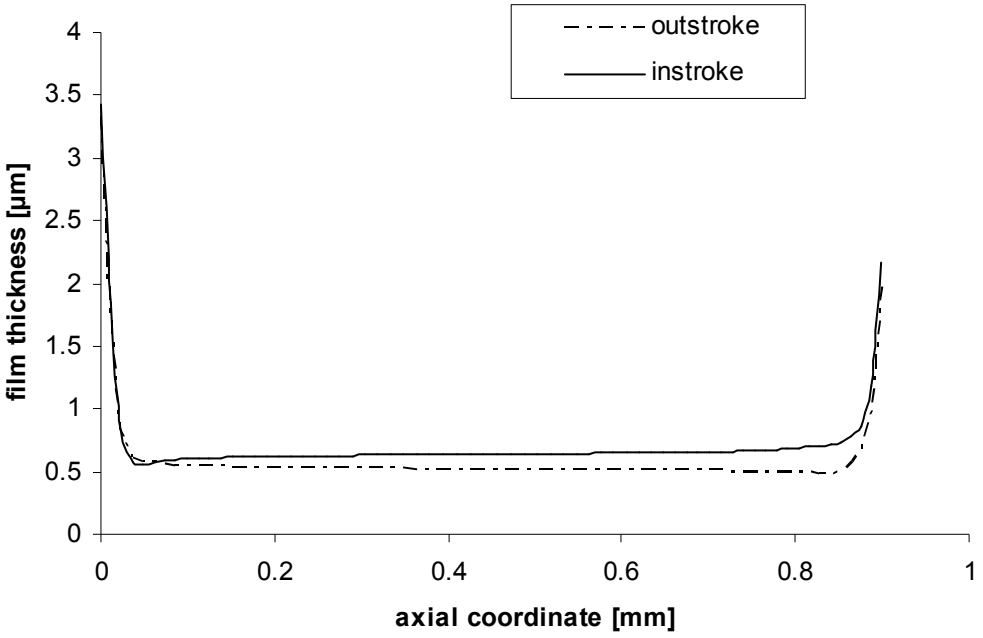

Figure 4.9: Film thickness distributions - secondary lip, 0.8 µm roughness.

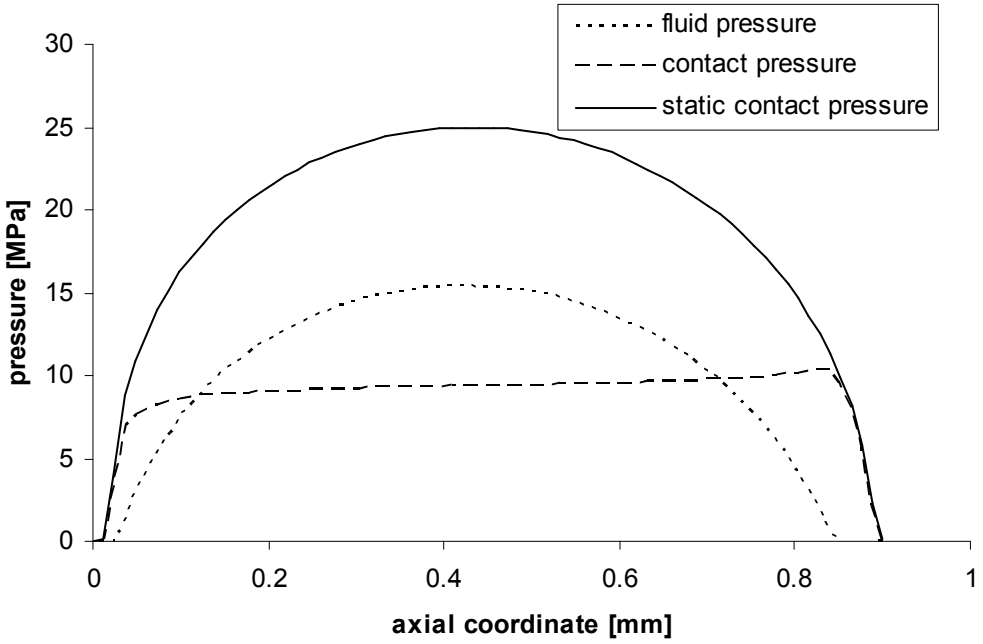

Figure 4.10: Pressure distributions - secondary lip, outstroke, 0.8 µm roughness.

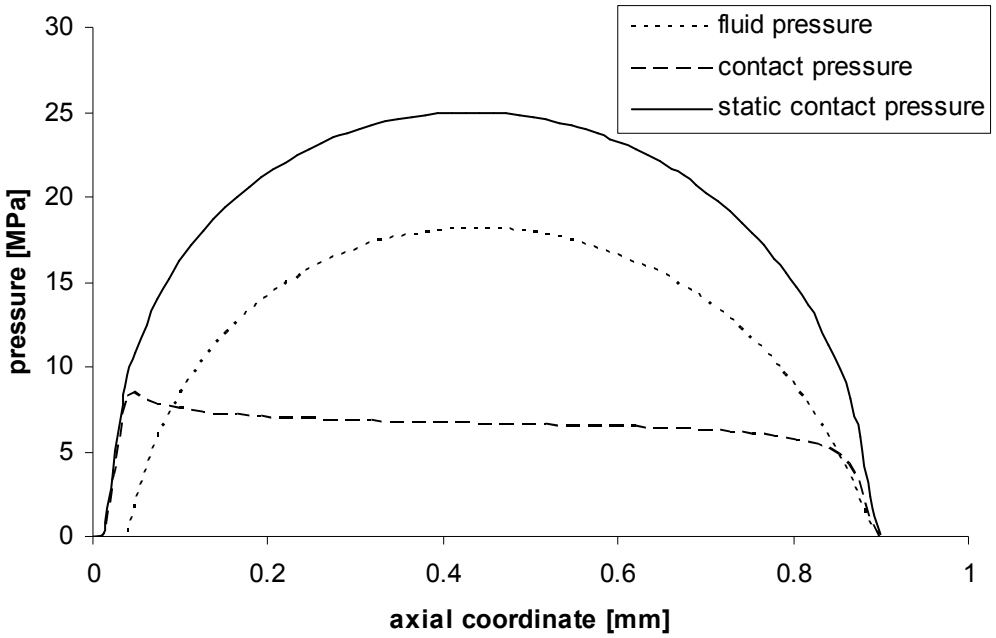

Figure 4.11: Pressure distributions - secondary lip, instroke, 0.8 μm roughness.

The film thickness and pressure distributions of the secondary lip are shown in Figure 4.9 to Figure 4.11. These, similarly, indicate mixed lubrication, and have characteristics that promote non-leakage: the film thickness during instroke is larger than that during outstroke; there is some cavitation during the outstroke to restrict outflow and no cavitation during the instroke allowing greater transport of fluid inward. The pressure distributions of the secondary lip are much more symmetric than those of the primary lip due to the secondary lip's symmetric shape.

It is useful to compare the above results for a non-leaking seal with those for a leaking seal: the same double lip seal but with a surface roughness of 1.6 μm, which Figure 4.4 indicates will leak. The behavior of such a seal is shown in Figure 4.12 to Figure 4.17.

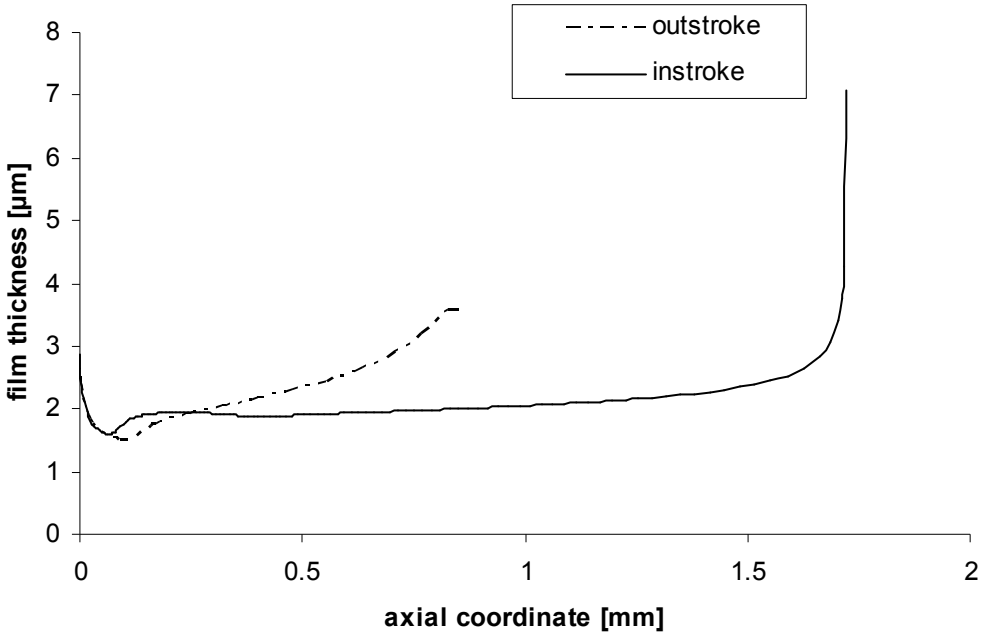

Figure 4.12: Film thickness distributions - primary lip, 1.6 µm roughness.

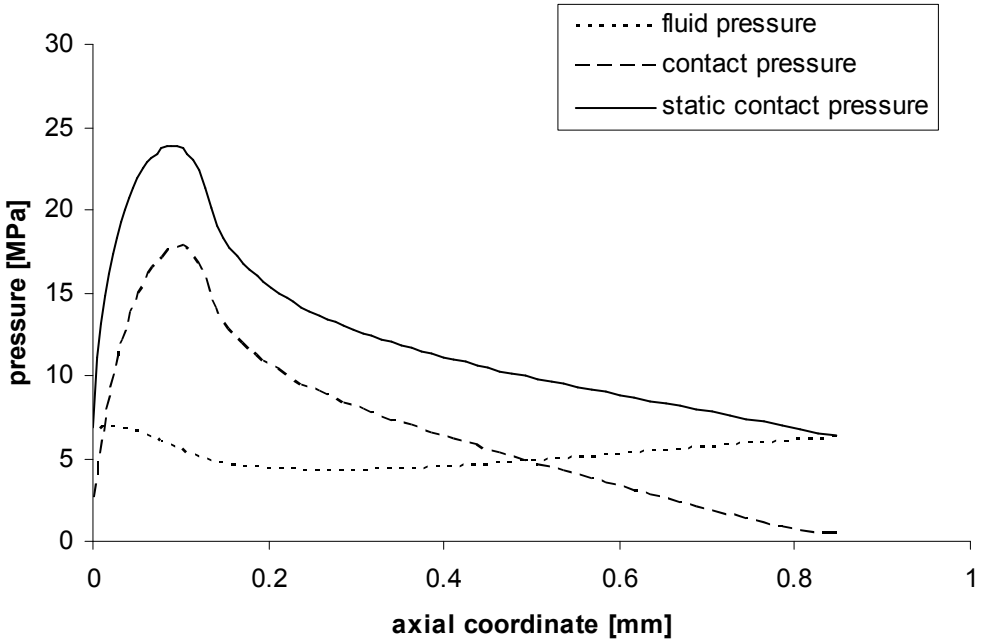

Figure 4.13: Pressure distributions - primary lip, outstroke, 1.6 µm roughness.

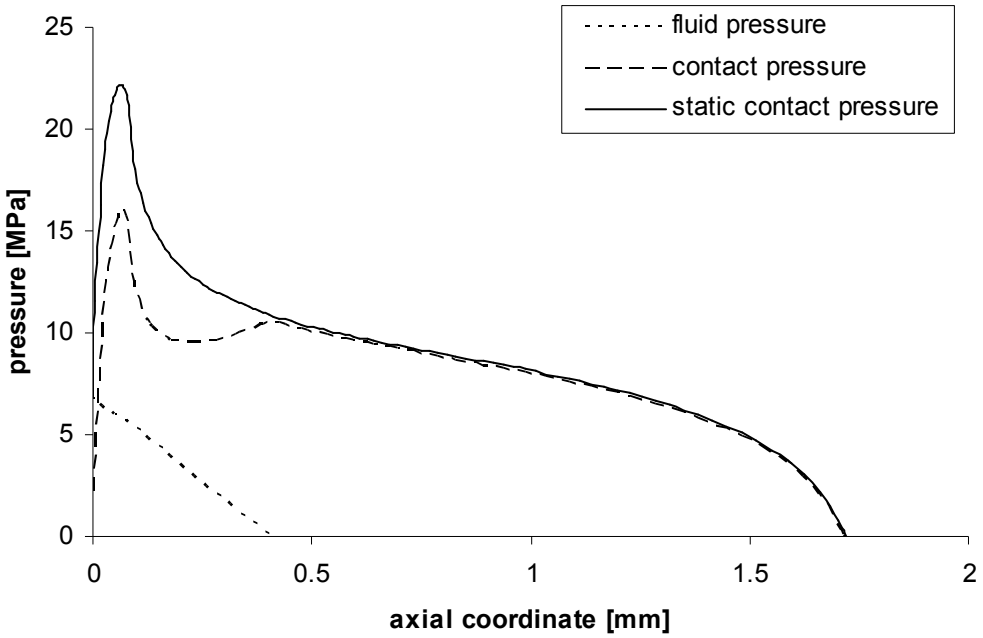

Figure 4.14: Pressure distributions - primary lip, instroke, 1.6 μm roughness.

The film thickness distributions of the primary lip, Figure 4.12, again indicate mixed lubrication. Here, however, we see the length of the sealing zone is much shorter during the outstroke than during the instroke, as mentioned earlier. Also, at proportional locations along the length of the sealing zone, the film thicknesses are larger for the outstroke than for the instroke. Both of these characteristics are detrimental for effective sealing, compared to the corresponding characteristics of the previously described non-leaking seal.

Figure 4.13 and Figure 4.14 show the pressure distributions of the primary lip. From these it is seen that there is no cavitation during the outstroke and a significant amount of cavitation during the instroke. This is the opposite of what occurs in the non-

leaking seal where cavitation helped prevent leakage; here it promotes leakage and is therefore detrimental.

The same general behavior is exhibited by the secondary lip, Figure 4.15 to Figure 4.17: mixed lubrication and the detrimental effect of cavitation (although there is a small amount of cavitation present during the outstroke).

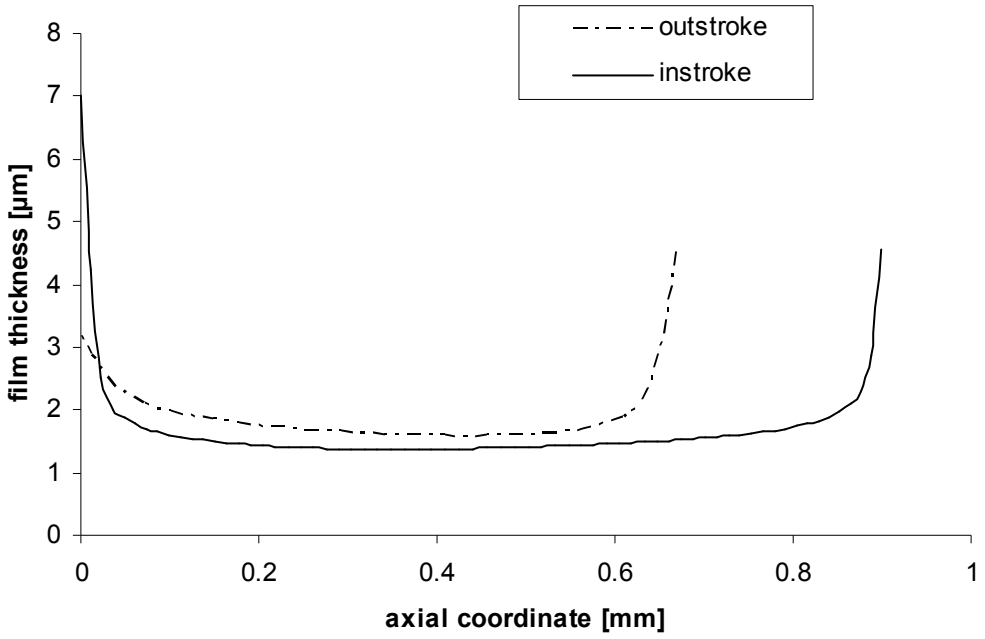

Figure 4.15: Film thickness distributions - secondary lip, 1.6 µm roughness.

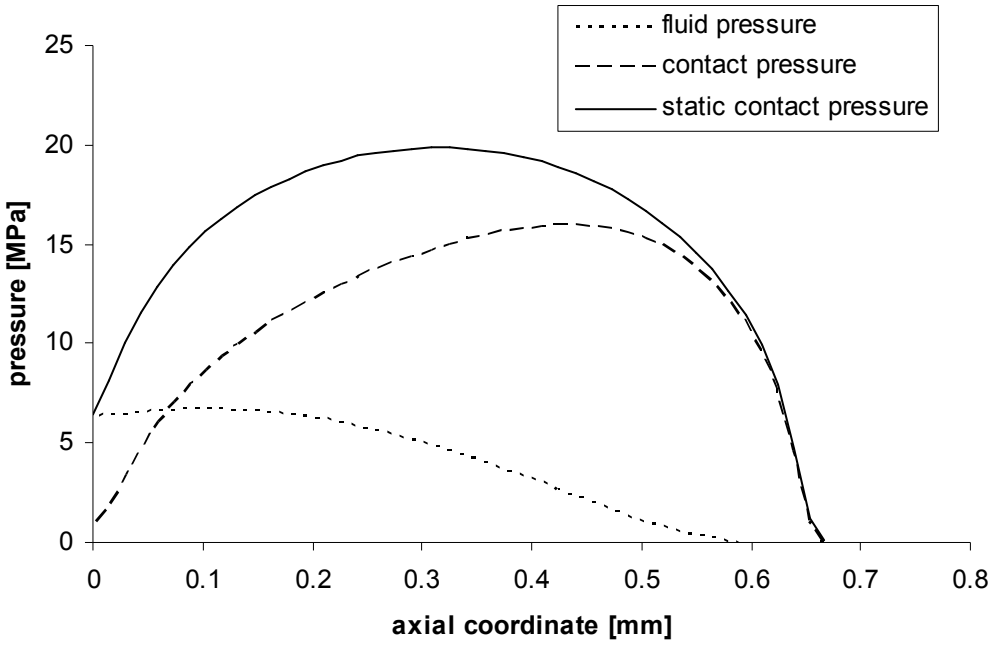

Figure 4.16: Pressure distributions - secondary lip, outstroke, 1.6 μm roughness.

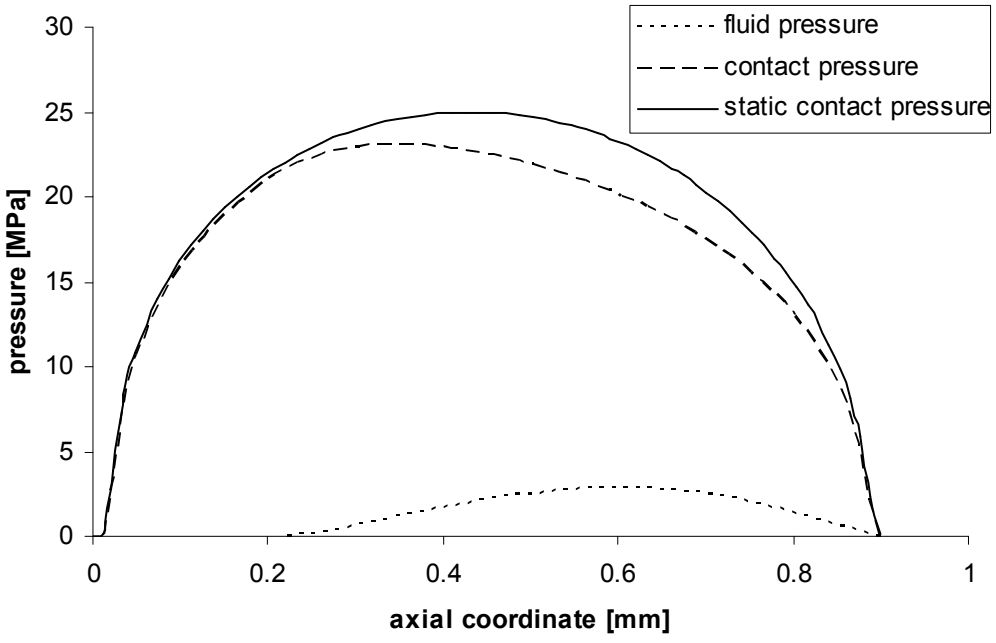

Figure 4.17: Pressure distributions - secondary lip, instroke, 1.6 μm roughness.

In addition to the film thickness and pressure distribution results for the double lip seal, shear stress distributions have also been generated. These are shown in Figure 4.18 and Figure 4.19 for the 0.8 μm case, and in Figure 4.20 and Figure 4.21 for the 1.6 μm case.

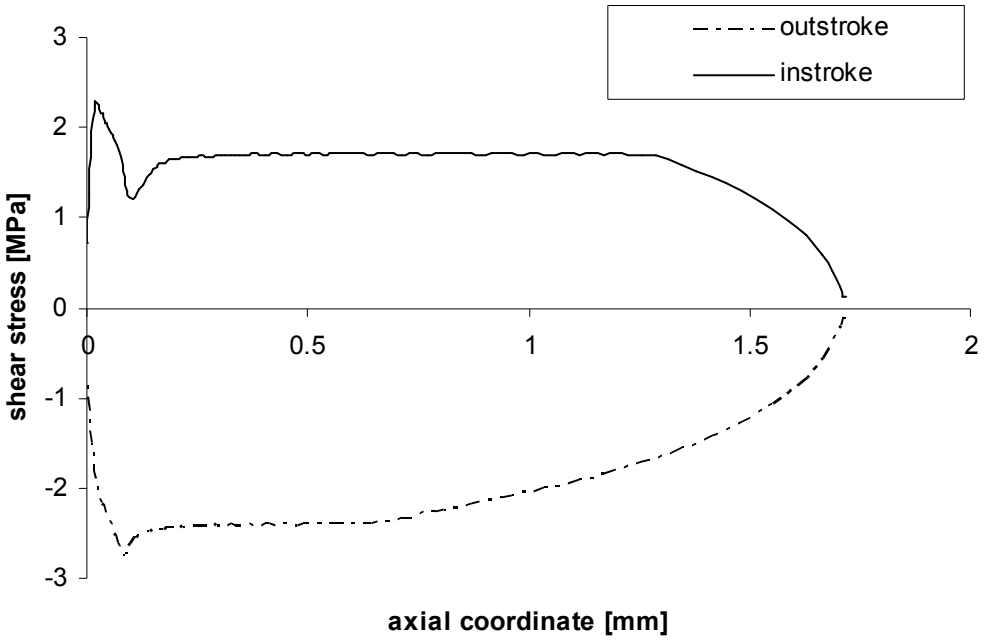

Figure 4.18: Shear stress distributions - primary lip, 0.8 μm roughness.

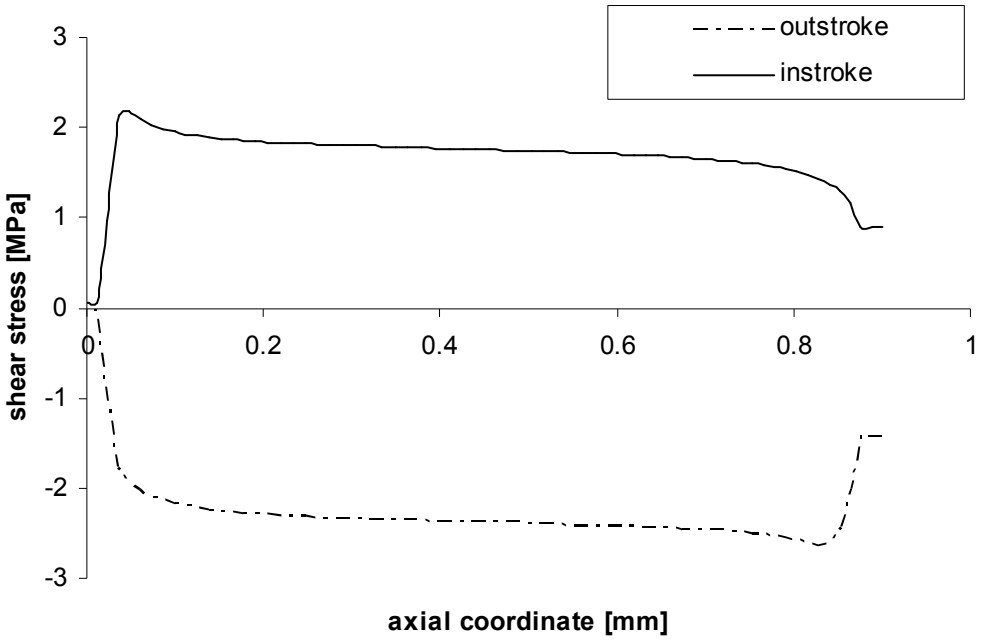

Figure 4.19: Shear stress distributions - secondary lip, 0.8 μm roughness.

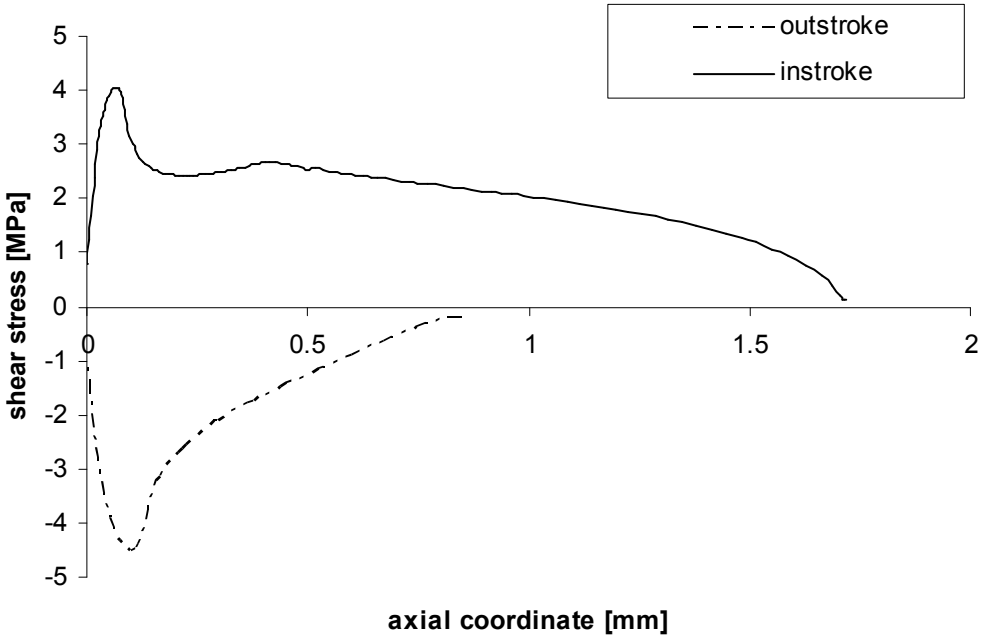

Figure 4.20: Shear stress distributions - primary lip, 1.6 μm roughness.

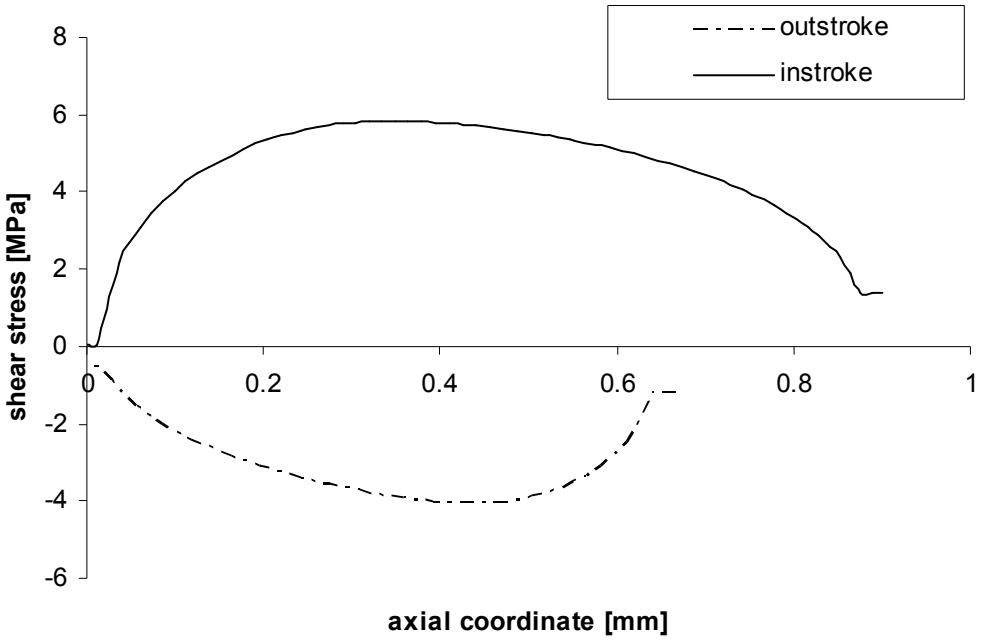

Figure 4.21: Shear stress distributions - secondary lip, 1.6 μm roughness.

4.5 Conclusion

The model results of this study show that the behavior of a reciprocating hydraulic rod seal with a double lip can be very different from that of a similar seal with a single lip. The secondary lip can strongly affect the behavior of the primary lip by producing an elevated pressure in the interlip region. The same seal characteristics that promote effective sealing in a single lip seal are also found to promote effective sealing in a double lip seal: cavitation of fluid in the sealing zone during the outstroke and a thicker film during the instroke than during the outstroke.

4.6 Secondary Lip Revised Seal

From Figure 4.22, one notices the secondary lip is symmetric which is against the empirical rule of successful shape: at the oil side, the angle between the lip and rod should be much larger than that at the air side. A possible improvement of the seal design is to revise the secondary lip to have a similar shape as the primary seal. Such a seal is shown in Figure 4.22. Compared with the original design, one can see, at the oil side the angle is changed from 45° to 60°, and at the air side the angle is changed from 45° to 30°, which is the same as the primary lip.

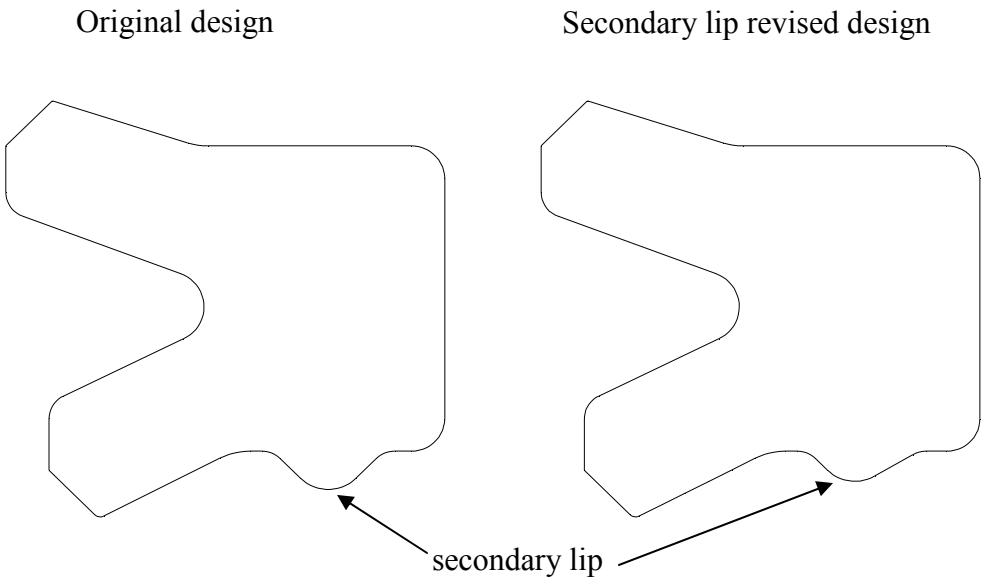

Figure 4.22: Comparison of seal configuration between revised design and original design.

Such a seal is analyzed using the same method as the normal double lip seal. The interlip pressure is shown as a function of roughness in Figure 4.23. Compared with Figure 4.3, one can see, for the outstroke, the trend of interlip pressure is the same.

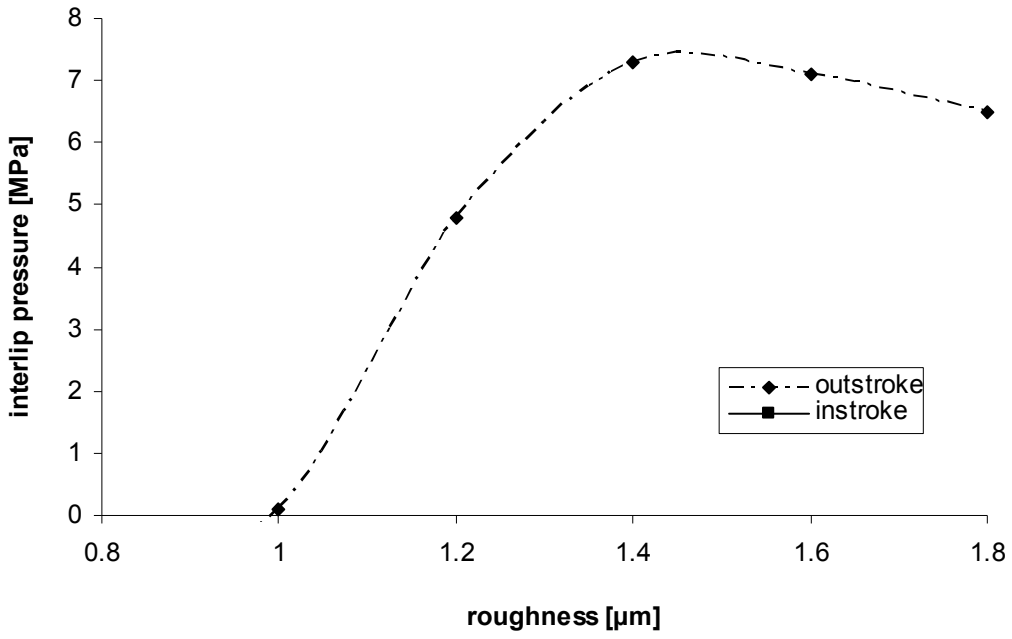

Figure 4.23: Interlip pressure vs. roughness, revised design.

Figure 4.24 contains a plot of the fluid transport versus roughness during instroke and outstroke for the double lip seal with the secondary lip revised. As discussed earlier, for zero net leakage, the instroke fluid transport must exceed the outstroke transport. This occurs at values of roughness below a critical roughness of approximately 1.2 µm, which is larger than the original design. This means the revision of the secondary lip improves the performance.

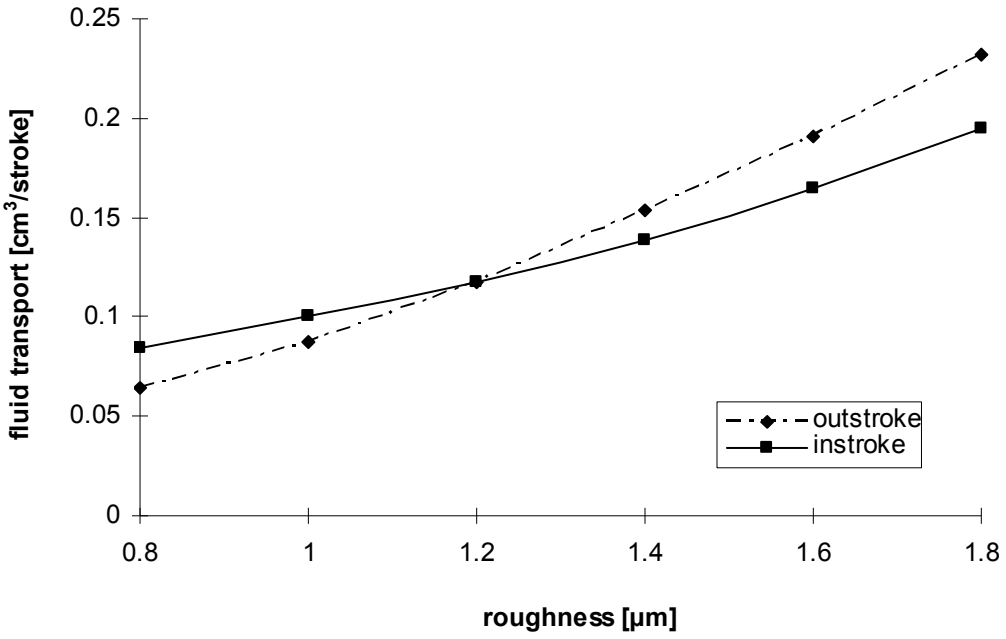

Figure 4.24: Fluid transport vs. roughness, revised design.

With the roughness of 1.1 µm, smaller than the critical roughness, the revised design acts as a non-leaking seal, while for the original design, Figure 4.4 indicates it will leak. The behavior of such a revised seal is shown in Figure 4.25 to Figure 4.30.

The film thickness distributions of the primary lip, Figure 4.25, again indicate mixed lubrication. Also, at proportional locations along the length of the sealing zone, the film thicknesses are smaller for the outstroke than for the instroke. These characteristics are beneficial for effective sealing, compared to the corresponding characteristics of the previously described leaking seal.

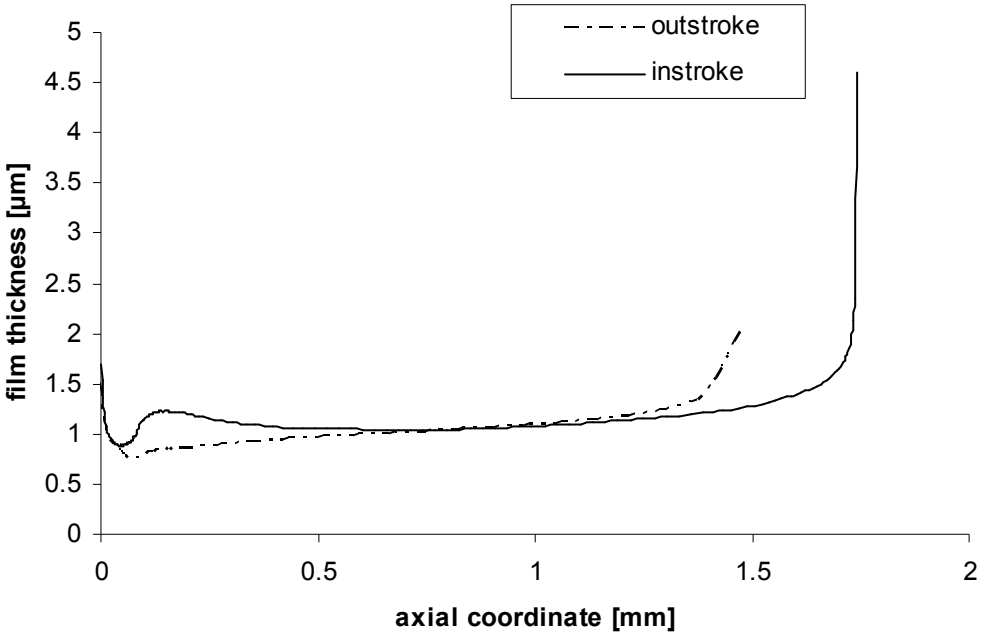

Figure 4.25: Film thickness distributions - primary lip, 1.1 µm roughness, revised design.

Figure 4.26 and Figure 4.27 show the pressure distributions of the primary lip. From these it is seen that there is a significant amount of cavitation during the outstroke and no cavitation during the instroke. This is the same as what occurs in the non-leaking seal where cavitation helped prevent leakage; here it helps prevent leakage and is therefore beneficial.

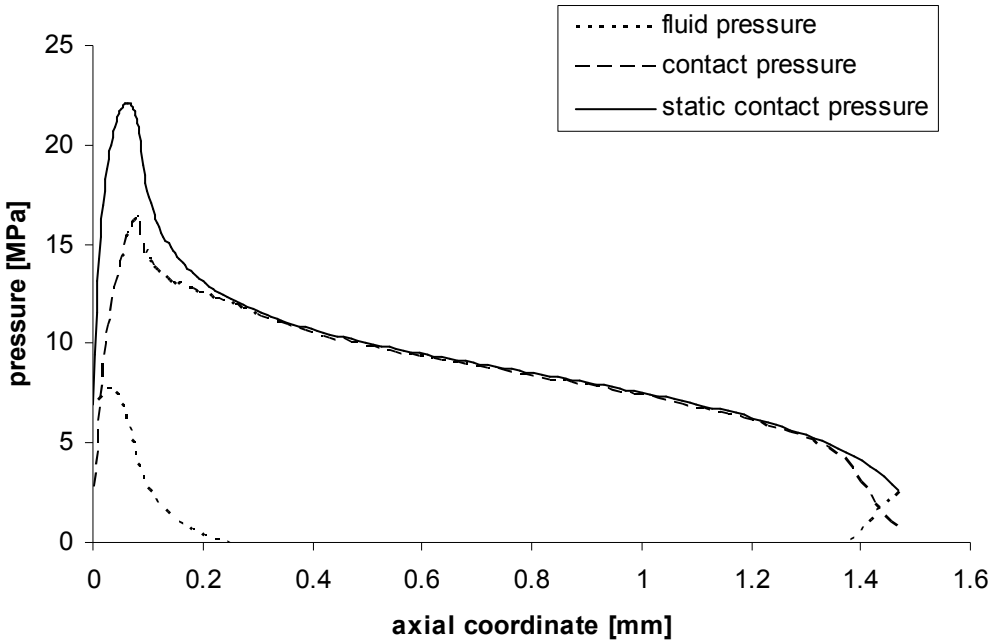

Figure 4.26: Pressure distributions - primary lip, outstroke, 1.1 μm roughness, revised design.

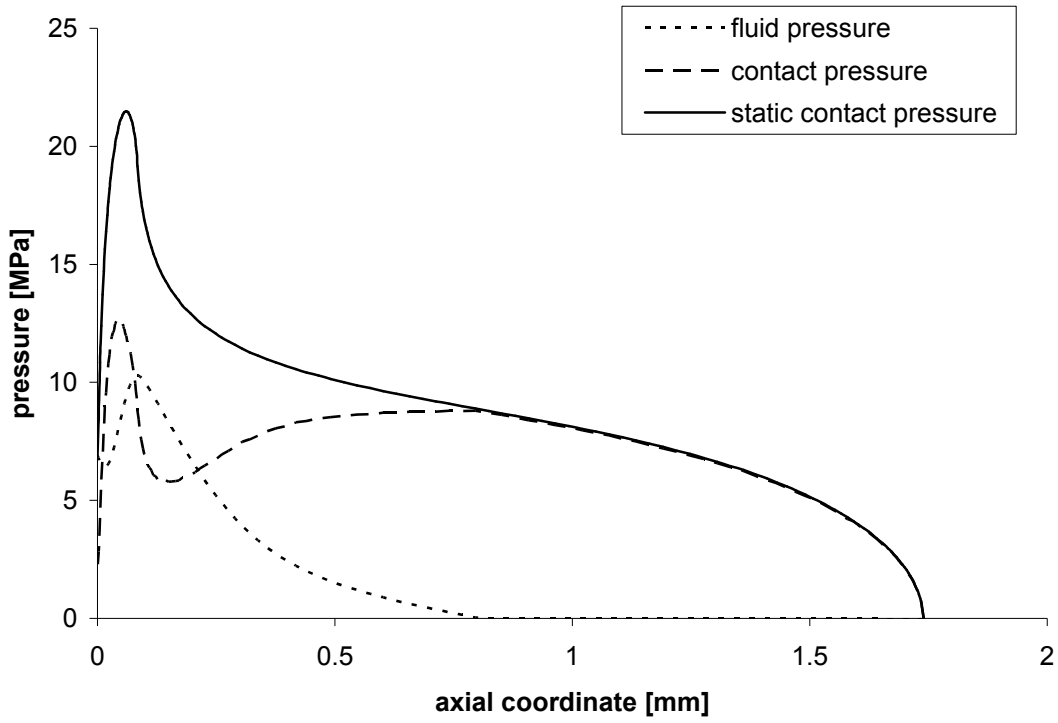

Figure 4.27: Pressure distributions - primary lip, instroke, 1.1 μm roughness, revised design.

Different from the symmetric film thickness and pressure distribution of the original design, the general behavior of the revised secondary lip is similar to that of the primary seal, Figure 4.28 to Figure 4.30: mixed lubrication and the beneficial effect of cavitation.

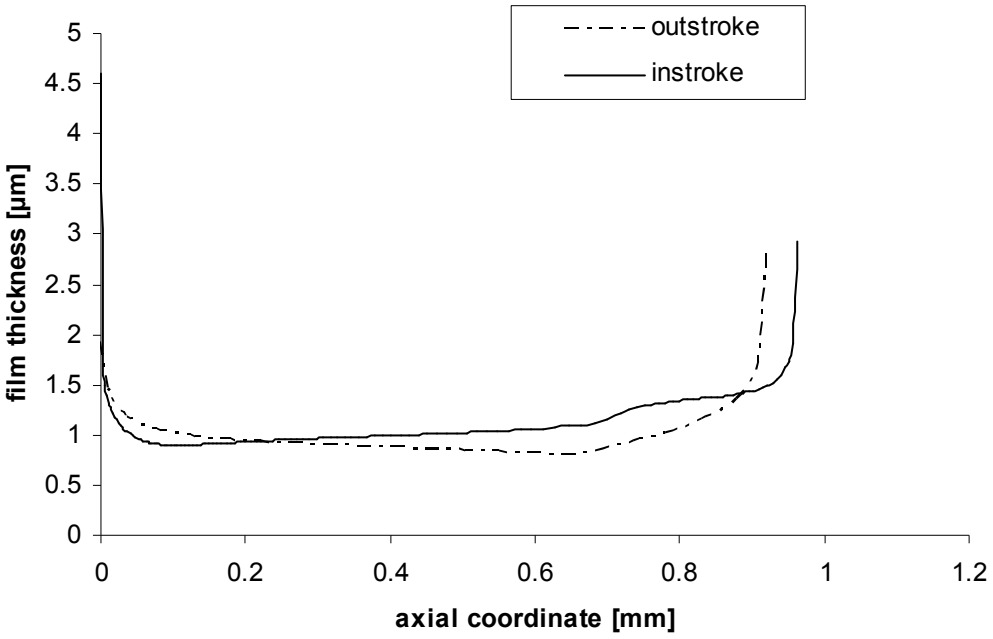

Figure 4.28: Film thickness distributions - secondary lip, 1.1 µm roughness, revised design.

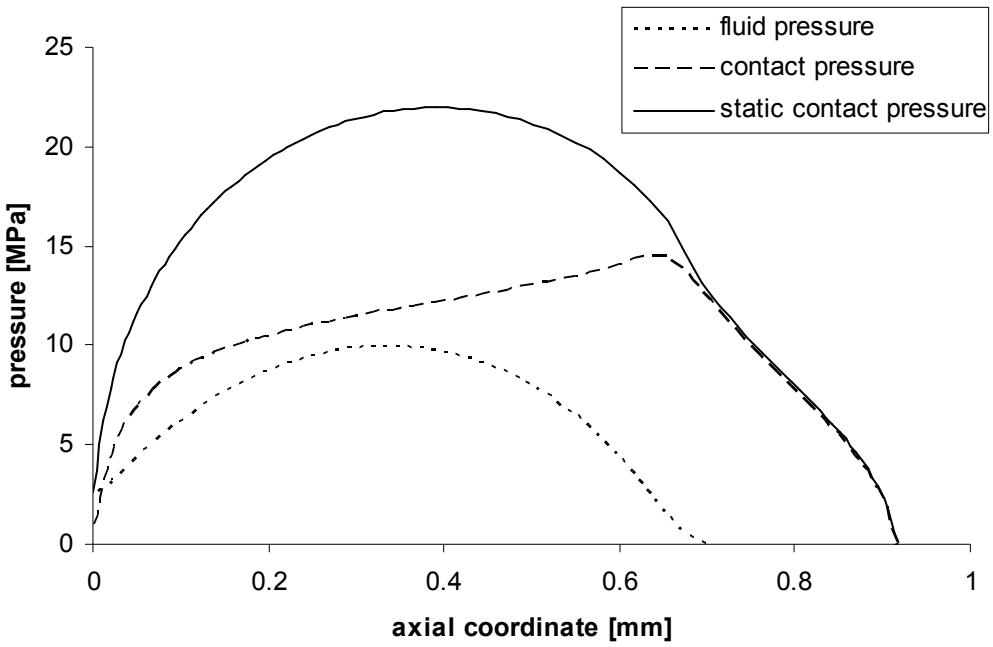

Figure 4.29: Pressure distributions - secondary lip, outstroke, 1.1 μm roughness, revised design.

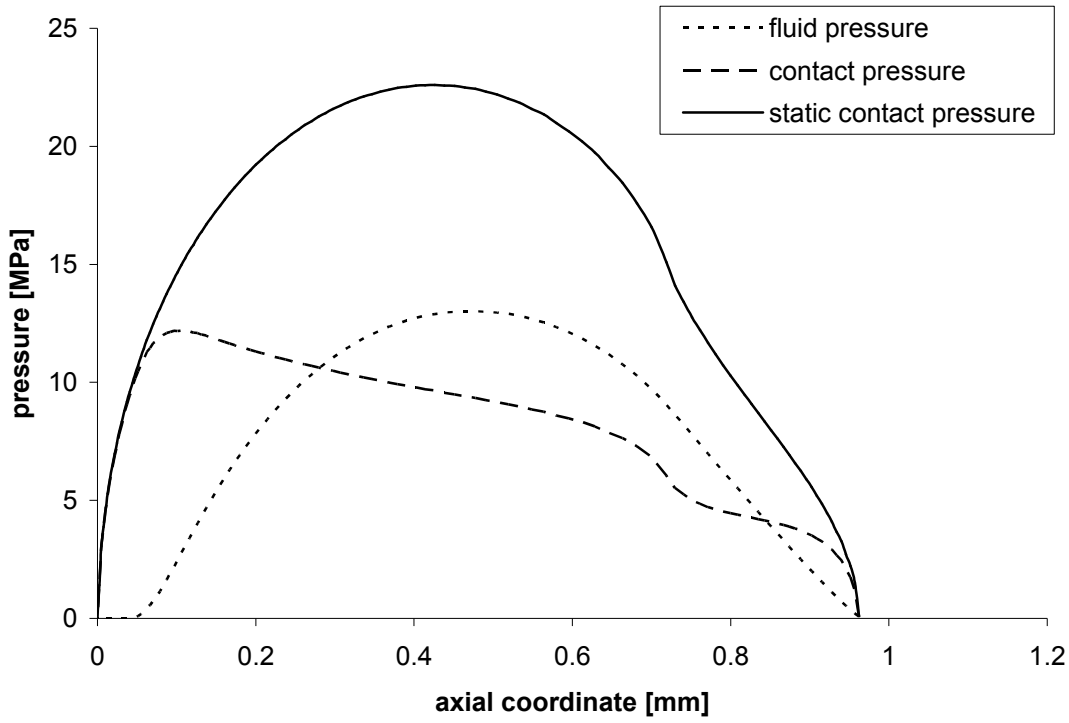

Figure 4.30: Pressure distributions - secondary lip, instroke, 1.1 μm roughness, revised design.

4.7 Tandem Seal

The secondary lip of a double lip seal is intended to act as a second line of defense in case of a defect in the primary lip, as well as a bearing. It also allows retention of lubricant in the interlip region in between periods of operation. However, it has been found that the secondary lip can interfere with the operation of the primary lip and reduce its sealing effectiveness, due to a very strong coupling between the actions of the two lips. An alternate means of obtaining a second line of defense is to use a tandem seal

arrangement, as shown schematically in Figure 4.31. The operation of such a seal is the subject of the present study [87].

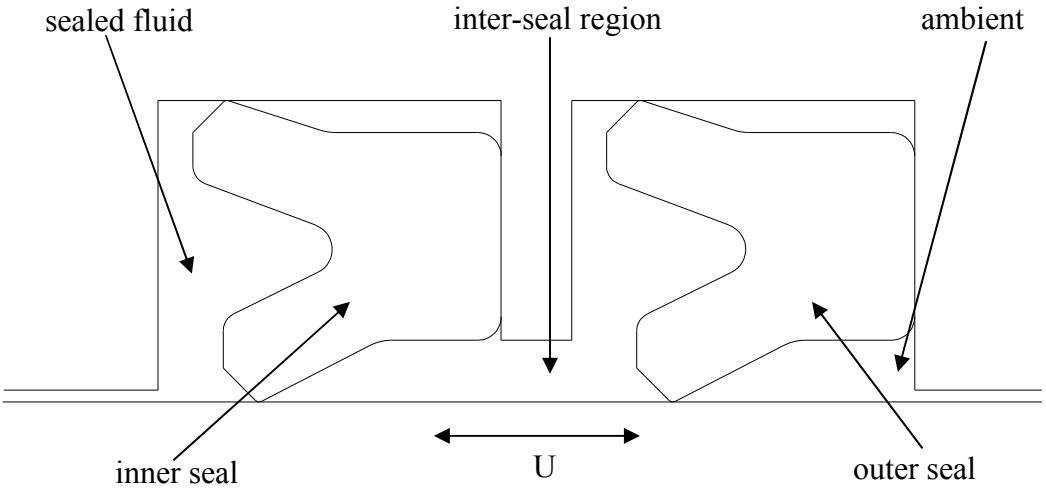

Figure 4.31: Schematic of tandem seal.

4.7.1 Analysis

The analysis of two seals in the tandem arrangement is very similar to the analysis of the double lip seal and will, therefore, only be outlined below.

Under steady state conditions (which are assumed), the mass flow rate past the two seals must be the same for the tandem seal, a restriction similar to the double seal.

$$\hat{q}_{outer} = \hat{q}_{inner} \tag{4.3}$$

Boundary conditions on Eq. (3.1) must be applied to both seals. For the inner seal (closest to the sealed fluid), the fluid pressure at the inner boundary is again equal to the sealed pressure, but that at the outer boundary is equal to the pressure in the inter-seal region (see

Figure 4.31), provided the fluid is not cavitated. For the outer seal, the fluid pressure at the inner boundary is also equal to the pressure in the inter-seal region, provided the fluid is not cavitated, while that at the outer boundary is equal to the ambient pressure. If the fluid in the inter-seal region is cavitated, then the average fluid density at the outer boundary of the inner seal must be equal to that at the inner boundary of the outer seal. Thus,

$$\begin{aligned} \phi_{inner} &= P_{sealed} \quad at\ \hat{x} = 0 \\ &= \phi_{interseal} \quad at\ \hat{x} = 1 \end{aligned} \tag{4.4}$$

$$\begin{aligned} \phi_{secondary} &= \phi_{interseal} \quad at\ \hat{x} = 0 \\ &= 1 \qquad\quad at\ \hat{x} = 1 \end{aligned}$$

It should be noted that the conditions in the inter-seal region are not known a priori, and must be determined in the course of the analysis. From these considerations it is clear that the behaviors of the two seals in a tandem seal are coupled. However, it is expected that such coupling is not as strong as that between the primary and secondary lips of a double lip seal, since the latter two lips are also structurally coupled.

4.7.2 Results

Computations have been performed for a typical tandem seal with the same base parameters as the single lip seal, as shown in Table 3.1.

Figure 4.32 shows a plot of fluid transport versus seal roughness for the outstroke and for the instroke. For zero net leakage, the latter must exceed the former. It is seen that the net leakage is strongly dependent on the seal roughness, and to obtain zero net leakage it is necessary for the seal roughness to be less than the critical value of 1.38 μm. The corresponding plot for an equivalent double lip seal is shown in Figure 4.4, where

the critical roughness, below which the net leakage is zero, is 1.08 μm. Thus, the tandem seal is a definite improvement over the double lip seal in regard to its sealing characteristic.

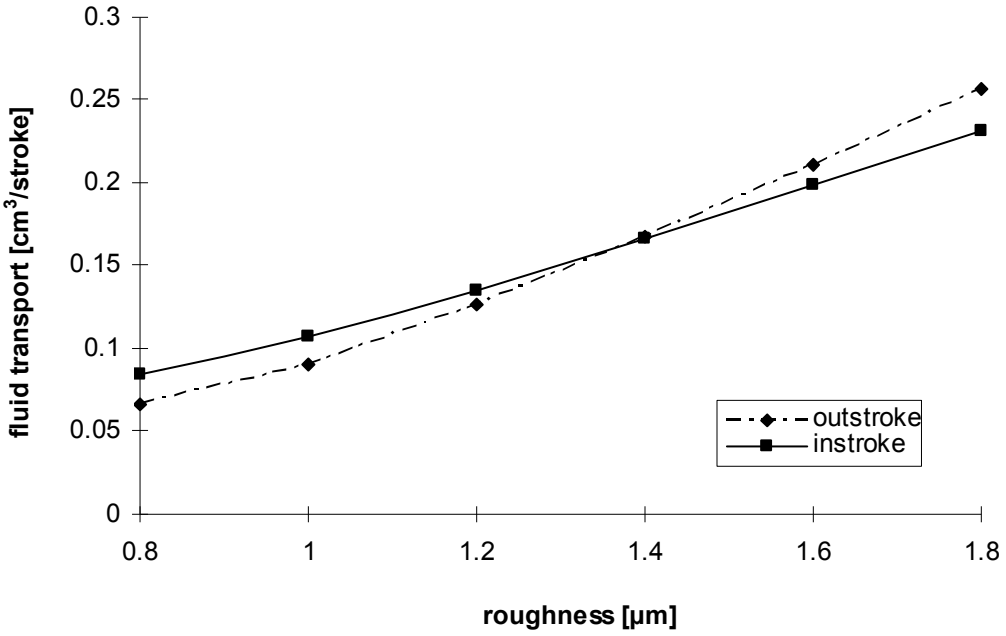

Figure 4.32: fluid transport versus seal roughness, tandem seal.

From the analysis in the previous chapter, the critical roughness is 1.37 μm for single lip seal, 1.08 μm for double lip seal, and 1.2 μm for double lip seal with secondary lip revised. Hence, the tandem seal has a sealing characteristic better than all the seals analyzed before, while still providing a second line of defense and allow retention of lubricant in the inter-seal region.

The pressure in the inter-seal region of the tandem seal is shown in Figure 4.33. During the outstroke it almost is a constant at a value of approximately 3 MPa. During the instroke it decreases with decreasing seal roughness; at a seal roughness below 1.6

μm the fluid in the inter-seal region cavitates. These pressures are much lower than the inter-lip pressures found in a comparable double lip seal, which can be as high as 6.4 MPa during the outstroke, depending on the seal roughness. This is one of the reasons why the characteristics of the tandem seal differ from those of the double lip seal. Another reason is the structural decoupling that occurs in the tandem seal. The effects of both can be seen in

Figure 4.34, which shows the deformed shapes of the various seals during the outstroke and instroke, each with a surface roughness of 1.6 μm. The interlip pressure in the double lip seal is 6.4 MPa during the outstroke and zero during the instroke, while the inter-seal pressure in the tandem seal is 3 MPa during the outstroke and zero during the instroke. Especially notable is the difference between the double lip seal and the tandem seal during the instroke. With the tandem seal, the outer seal lip makes comparatively little contact with the rod, due to the zero pressure in the inter-seal region and decoupling of the two seals. It therefore produces very little resistance to the fluid transport during the instroke. Conversely, with the double lip seal, the secondary lip makes substantial contact with the rod, in spite of the zero pressure in the interlip region, due to the structural coupling between the two lips. It therefore produces significant resistance to the fluid transport during the instroke.

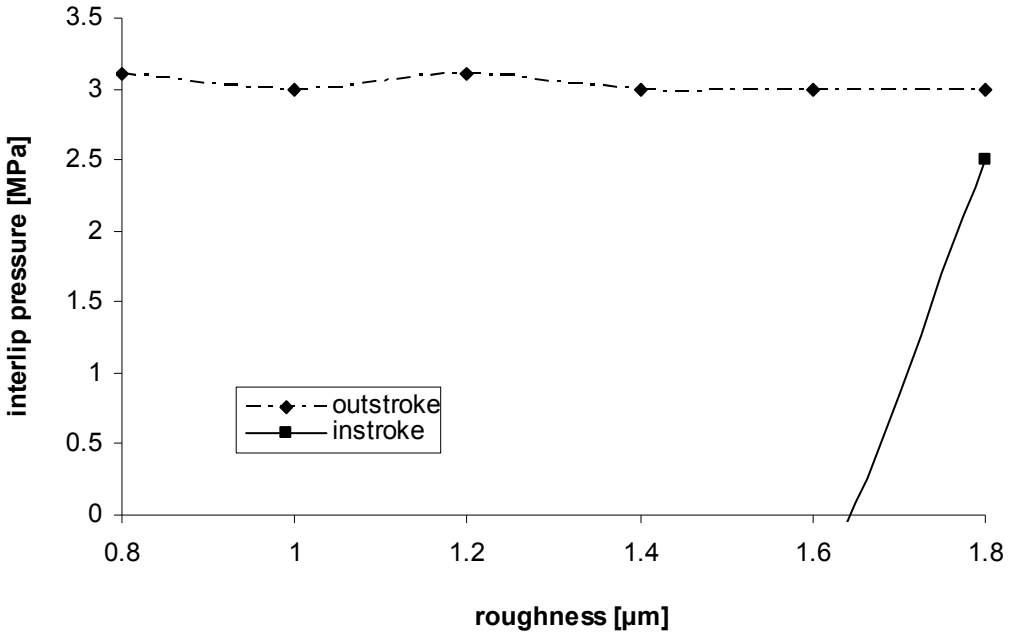

Figure 4.33: Interlip pressure vs. roughness.

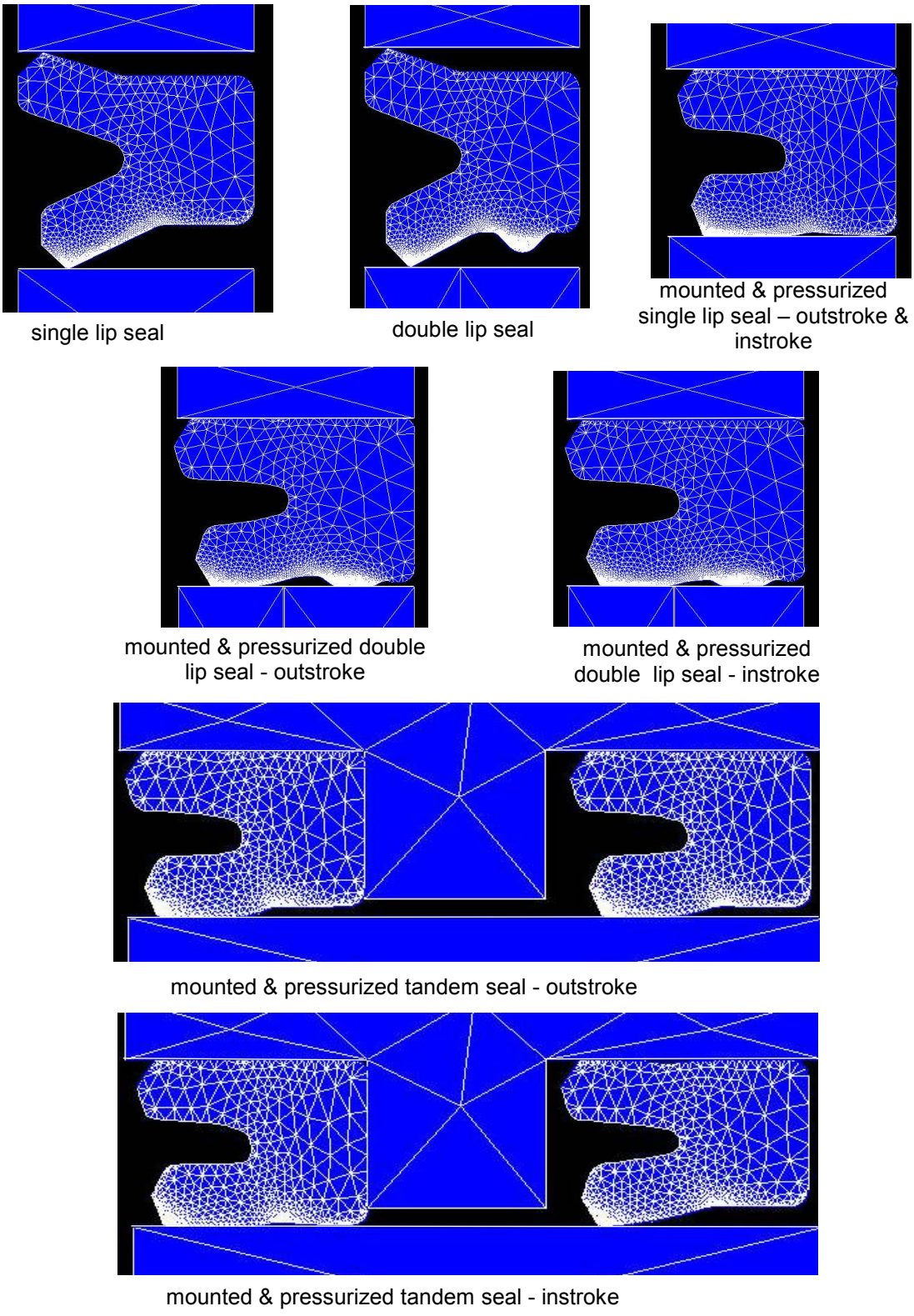

Figure 4.34: Deformed shapes of the various seals during the outstroke and instroke.

Figure 4.35 shows the frictional force on the rod, due to both asperity contact and viscous friction, as a function of surface roughness, for the tandem seal. Compared to the double lip seal, Figure 4.5, the frictional force is smaller, though larger than that for a single lip seal, Figure 3.21. It is interesting to note that the shapes of the curves for the tandem seal and the single lip seal are quite similar, while that of the double lip seal is quite different. This is due to the much stronger coupling between the two lips in the double lip seal, as compared to the two lips in the tandem seal.

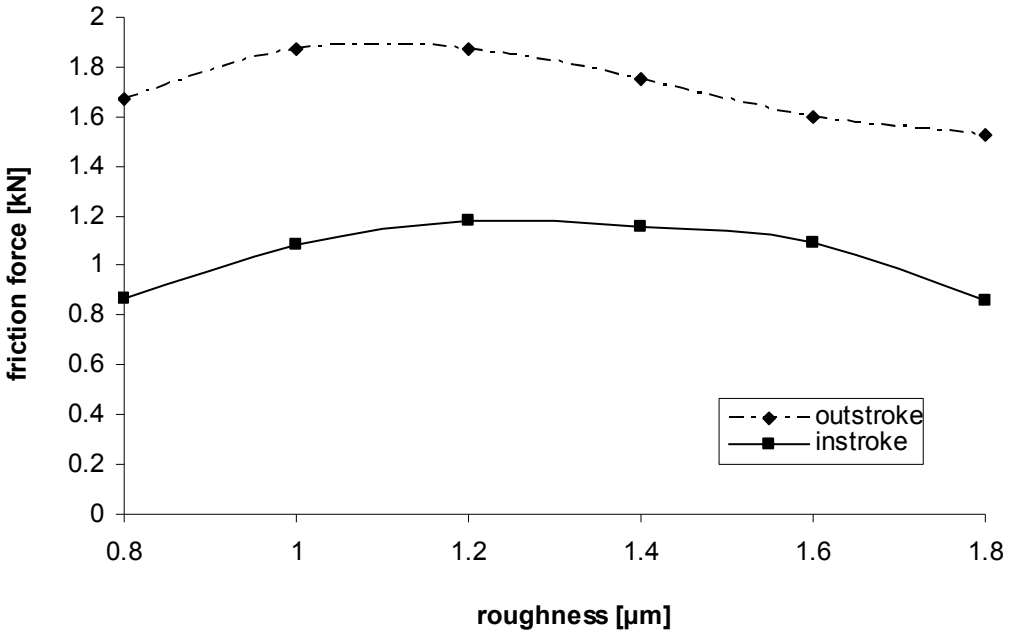

Figure 4.35: Fluid force vs. roughness, tandem seal.

Figure 4.36 shows the film thickness distributions of the inner seal for a seal roughness of 0.8 µm, a non-leaking case. The sealing zone is shorter during the outstroke than during the instroke, a result of the difference in inter-seal pressures. Also, the film is

thicker during the instroke than during the outstroke. This is a favorable characteristic because a relatively thicker film during the instroke allows relatively more fluid to be drawn into the cylinder, thereby reducing the possibility of leakage. For a leaking case with 1.6 μm seal roughness, the corresponding Figure 4.37 indicates the film thickness during the instroke is smaller than that during the outstroke, an unfavorable characteristic. It is also important to note that the film thicknesses during both instroke and outstroke for the non-leaking case are much smaller than the corresponding film thicknesses for the leaking case. For both cases the film thickness is less than 3σ, indicating mixed lubrication. Similar results had been previously found with single lip and double lip seals.

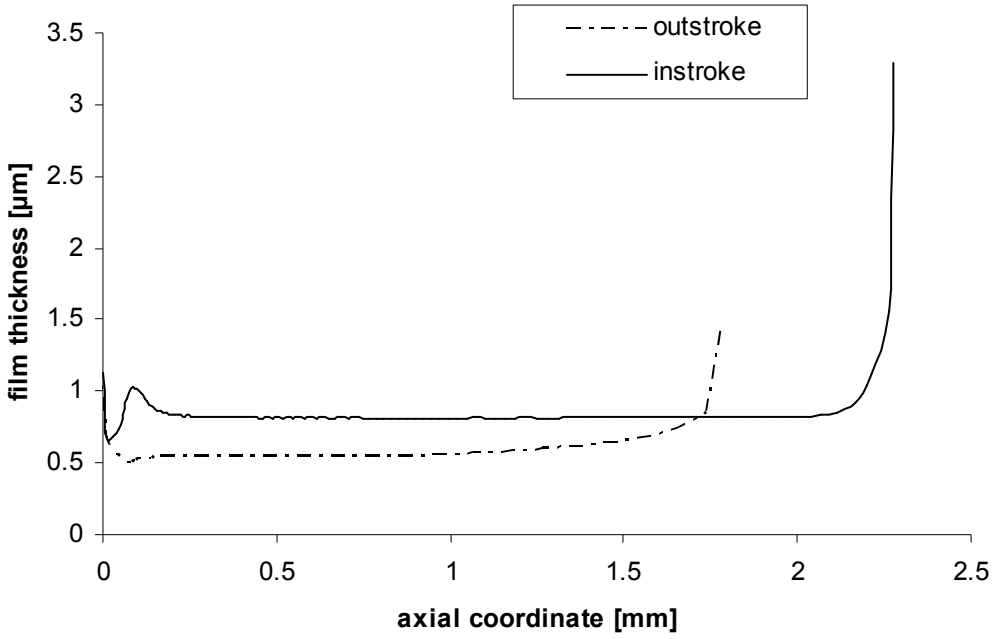

Figure 4.36: Film thickness distributions - inner seal, 0.8 μm roughness.

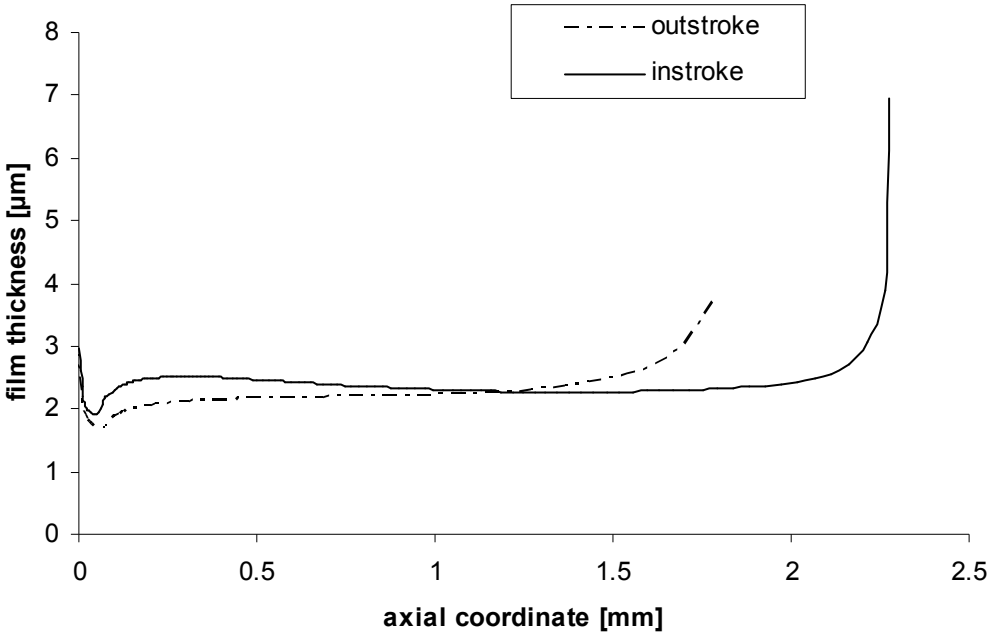

Figure 4.37: Film thickness distributions - inner seal, 1.6 µm roughness.

The static contact pressure, contact pressure and fluid pressure distribution of the inner seal for the non-leaking 0.8 µm seal roughness case are shown in Figure 4.38 and Figure 4.39 for the outstroke and instroke, respectively. The static contact pressure distribution has the characteristic shape typical of successful seals, with the peak closest to the inner side. During the outstroke, the fluid pressure near the inner side produces a reduction in the contact pressure. However, near the outer side of the seal the fluid pressure goes to zero and there is significant cavitation in the sealing zone. This, too, is a favorable characteristic since the cavitation restricts the amount of fluid that is carried out of the cylinder. During the instroke there is significantly greater hydrodynamic pressure elevation, with a larger reduction in the contact pressure. The cavitation is almost completely eliminated, allowing fluid to be drawn into the cylinder more freely. Figures

Figure 4.40 and Figure 4.41 contain corresponding curves for the leaking case of 1.6 μm seal roughness. From Figure 4.40 it is clear that in the leaking case the previously mentioned beneficial cavitation during the outstroke has been eliminated. Figure 4.41 shows that there is also no cavitation during the instroke in the leaking case. Similar results regarding the occurrence of cavitation had been previously found with a single lip and double lip seal.

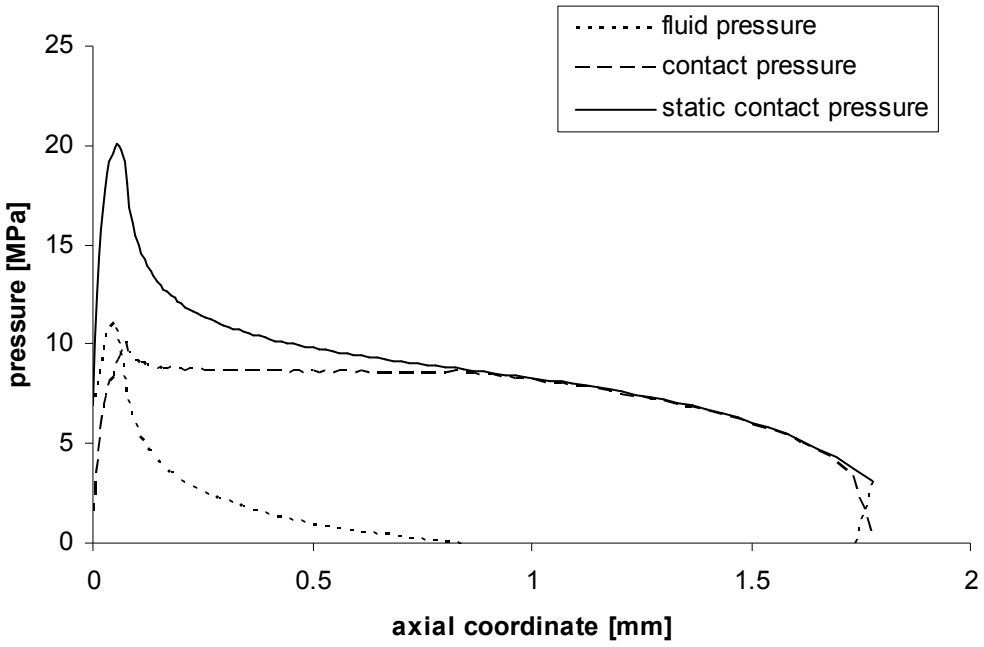

Figure 4.38: Pressure distributions - inner seal, outstroke, 0.8 μm roughness.

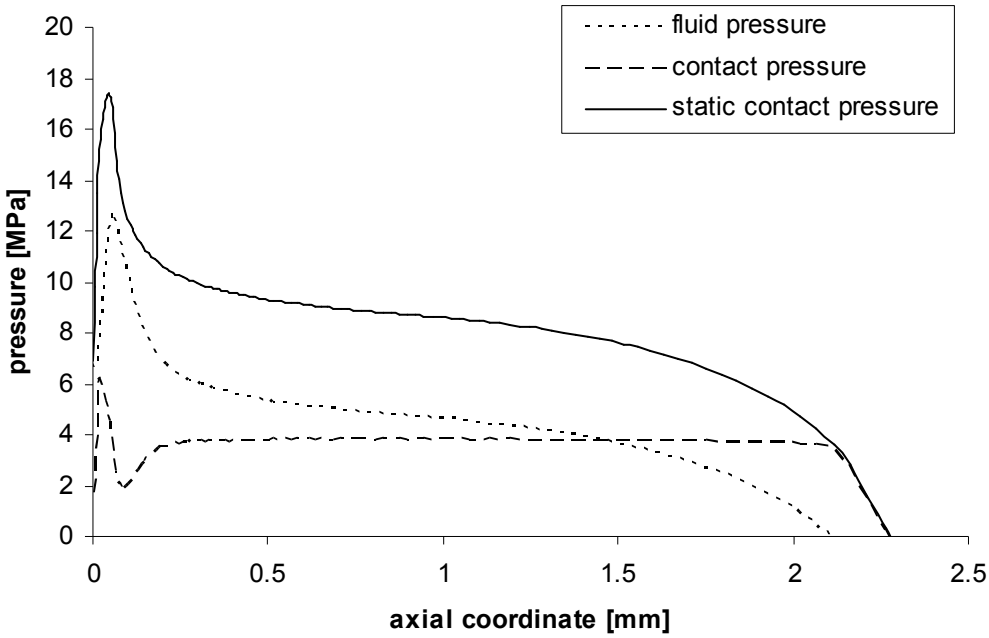

Figure 4.39: Pressure distributions - inner seal, instroke, 0.8 μm roughness.

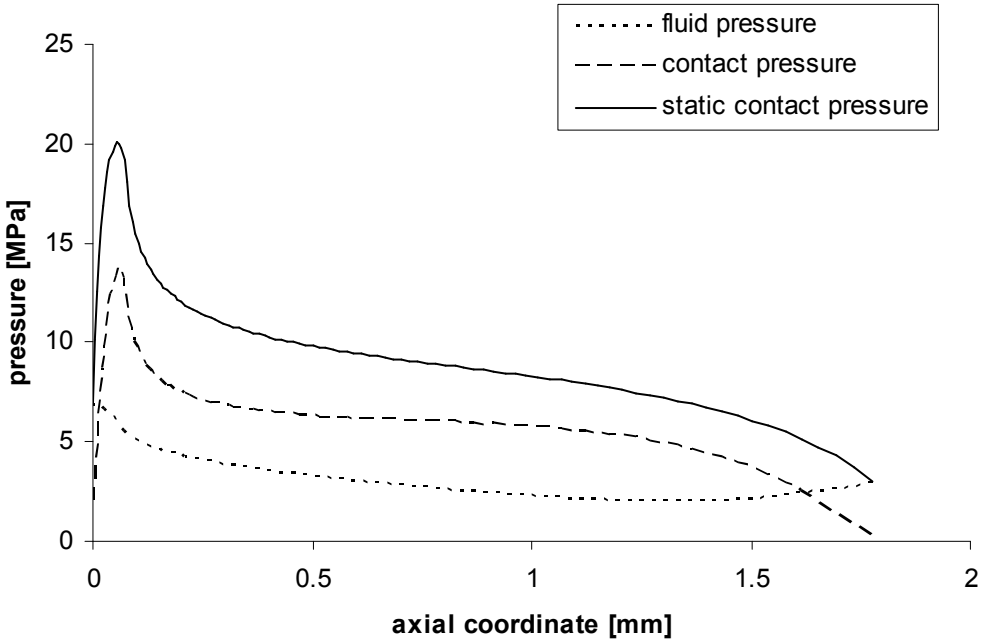

Figure 4.40: Pressure distributions - inner seal, outstroke, 1.6 μm roughness.

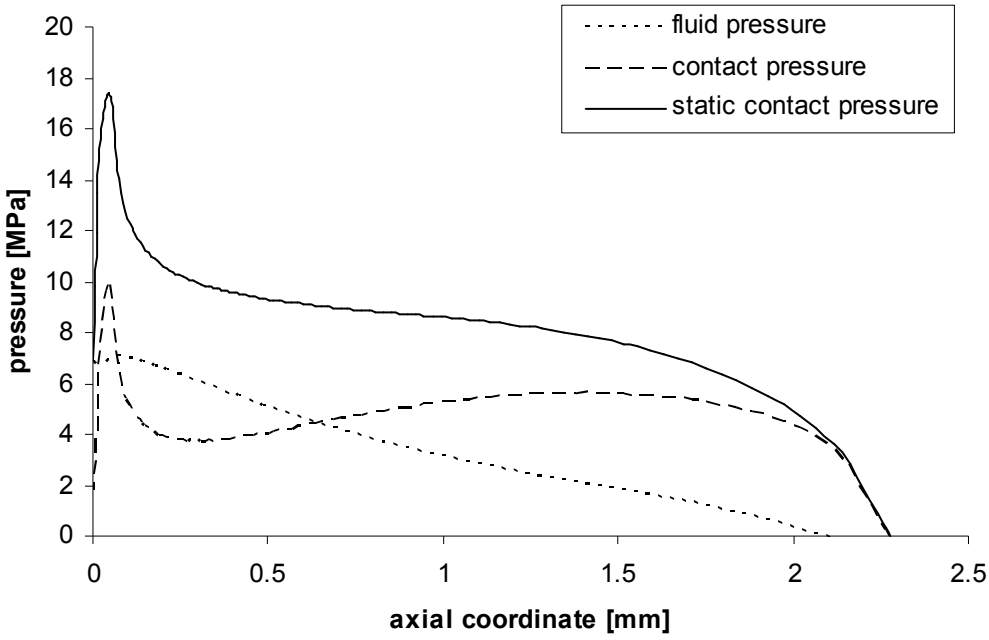

Figure 4.41: Pressure distributions - inner seal, instroke, 1.6 μm roughness.

The above film thickness and pressure distributions pertain to the inner seal of the tandem arrangement. Corresponding distributions for the outer seal are contained in Figure 4.42 to Figure 4.47, for both the non-leaking case with a seal roughness of 0.8 μm and the leaking case with a roughness of 1.6 μm.

Comparing Figure 4.42 with Figure 4.43 shows that the film thickness during the instroke is larger than that during the outstroke at proportional locations along the length of the sealing zone for the non-leaking case, while the outstroke and instroke thicknesses are about the same for the leaking case. Also, the film thicknesses are smaller, and the length of the sealing zone during the outstroke is larger for the non-leaking case than for the leaking case. These results are similar to those for the inner seal.

Figure 4.44 and Figure 4.46 show that the cavitation occurring in the sealing zone during the outstroke in the non-leaking case is substantially reduced in the leaking case, similar to the results for the inner seal. However, for the inner seal the cavitation is essentially eliminated in the leaking case, while for the outer seal it is still present, though diminished. From Figure 4.45 and Figure 4.47, it is seen that no cavitation occurs during the instroke for the outer seal in both the non-leaking and leaking cases, similar to the results for the inner seal.

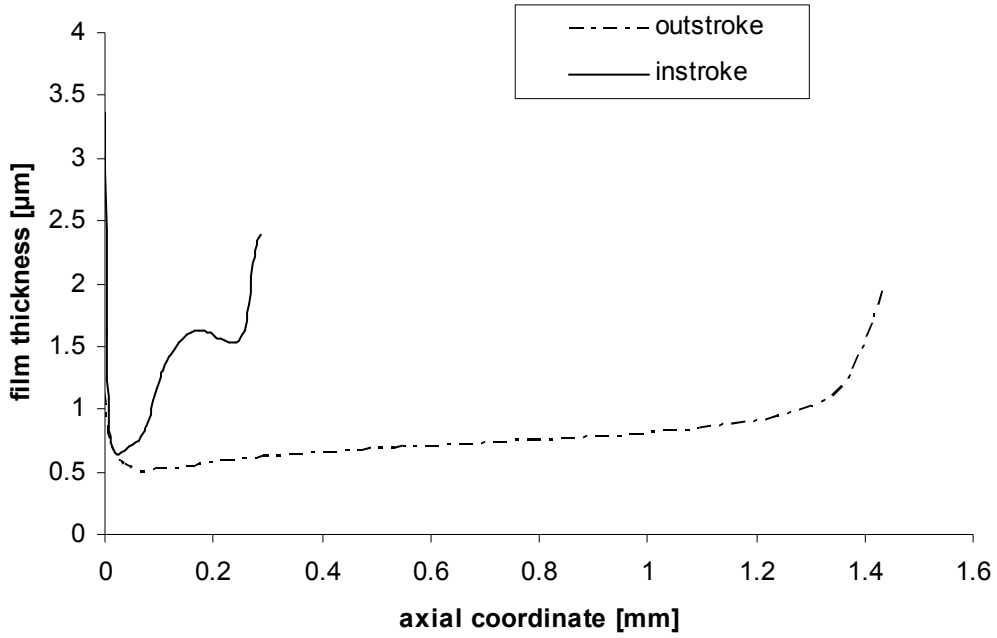

Figure 4.42: Film thickness distributions - outer seal, 0.8 µm roughness.

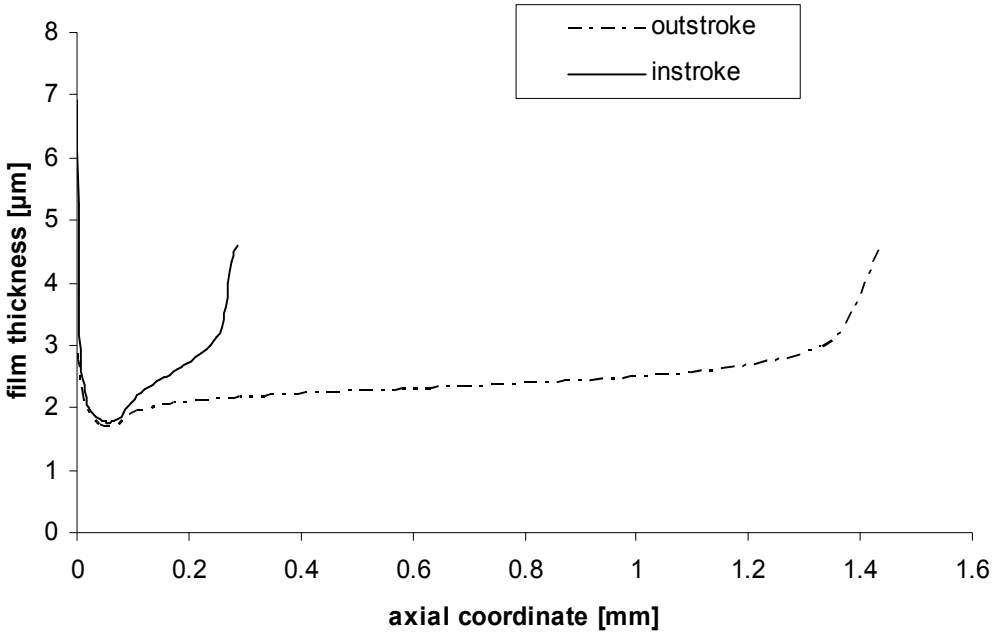

Figure 4.43: Film thickness distributions - outer seal, 1.6 µm roughness.

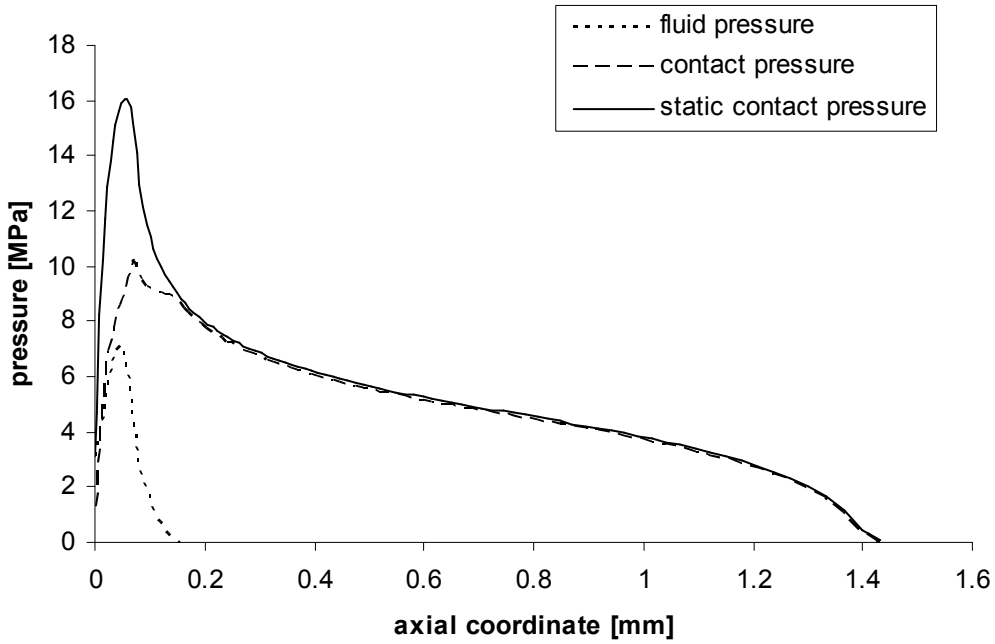

Figure 4.44: Pressure distributions - outer seal, outstroke, 0.8 µm roughness.

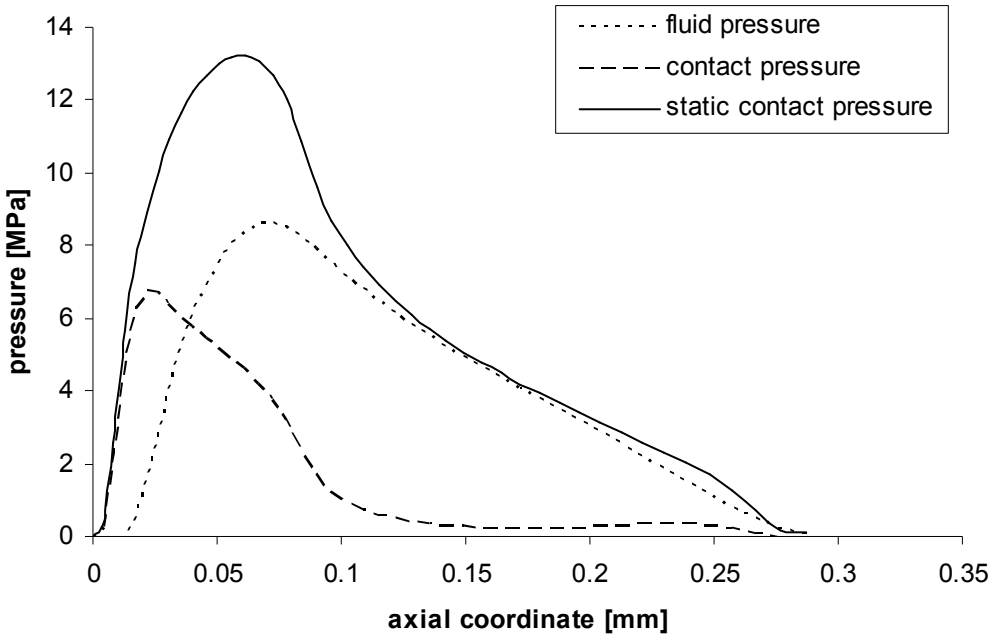

Figure 4.45: Pressure distributions - outer seal, instroke, 0.8 μm roughness.

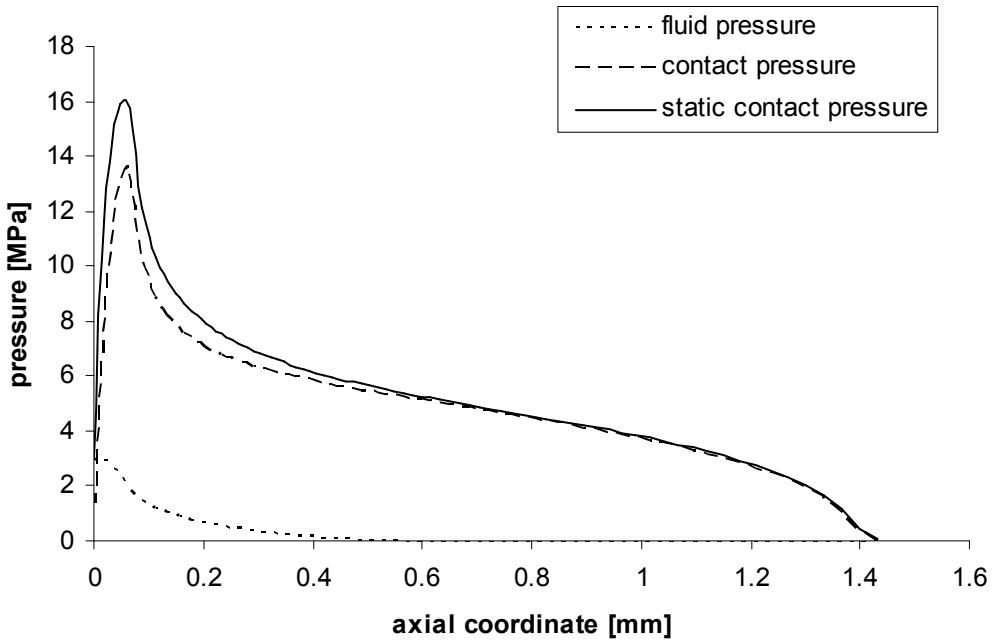

Figure 4.46: Pressure distributions - outer seal, outstroke, 1.6 μm roughness.

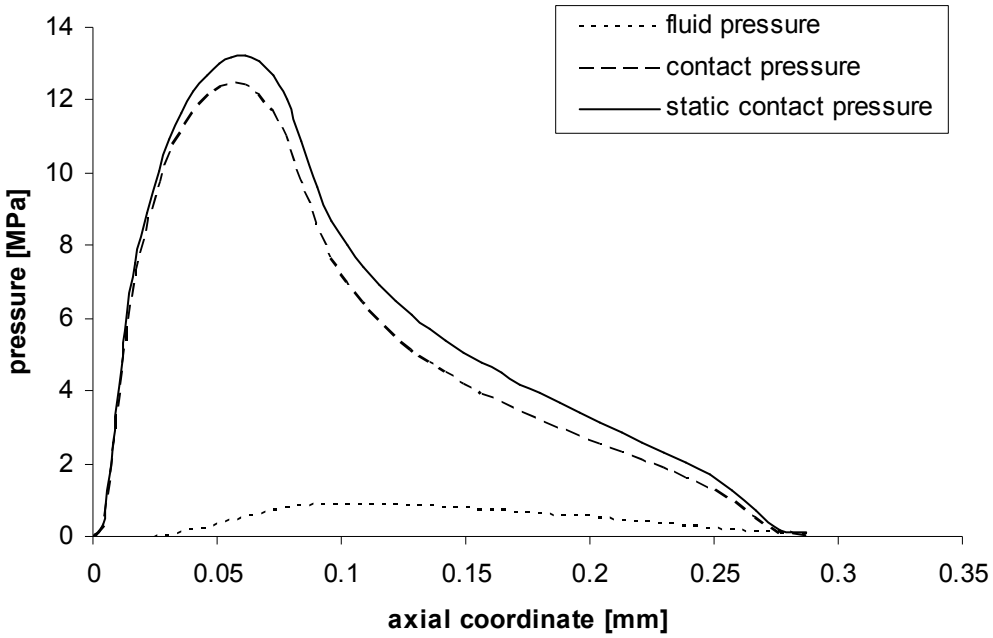

Figure 4.47: Pressure distributions - outer seal, instroke, 1.6 μm roughness.

4.7.3 Conclusions

The results of this study indicate that the typical tandem hydraulic rod seal operates with mixed lubrication, like the previously studied single lip and double lip seals. Its behavior is very dependent on the seal surface roughness, and is characterized by a critical roughness below which there is zero net leakage. This critical roughness is higher than that of a comparable double lip seal and almost as high as that of a comparable single lip seal. The friction force produced by the tandem seal on the rod is somewhat higher than that produced by the single lip seal but lower than that produced by the double lip seal.

As with the single and double lip seals, the following characteristics have been found to promote zero or reduced leakage:

- small seal surface roughness
- small lubricating film thickness
- thicker film during instroke than during outstroke
- cavitation in film during outstroke
- structural decoupling of multiple lips

CHAPTER 5

STEP SEAL

5.1 Introduction

The numerical analyses of U-cup seals of the previous chapters, using a soft EHL model, has revealed that such seals operate with mixed lubrication in the sealing zone (interface between the rod and the seal) and seal roughness plays an important role in determining seal behavior. A similar model is used to investigate the behavior of a step seal and compare its performance to that of a U-cup seal [88]-[89].

5.2 Seal Configuration

A typical step seal, mounted and pressurized, is shown in Figure 5.1. The lower sealing element, adjacent to the rod, is PTFE, while the upper O-ring actuator is nitrile rubber.

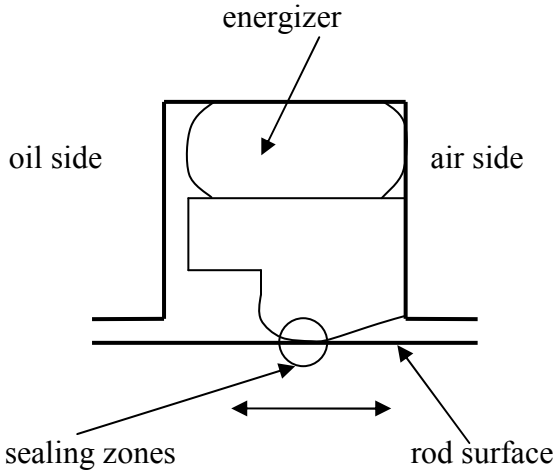

Figure 5.1: Typical step seal.

5.3 Analysis

The analysis of step seal is very similar to the analysis of single lip seal. The model consists of a fluid mechanics analysis, a contact mechanics analysis, a deformation analysis, a thermal analysis and an iterative computational procedure. The primary difference between the analyses of the U-cup seal and step seal, which complicates the step seal model, is the complex material property of PTFE. The secondary difference is the presence of the energizer.

As described before in the background introduction, for the PTFE like composite material, it's very hard to derive a suitable material model. So, the experimental stress strain curve obtained from tests is used to describe the material property. In the finite element software, the multilinear option is selected and all the data are input through a table. Another difference between the PTFE based composite material and the rubber like elastomers is the compressibility. Rubber normally is treated as incompressible and the Poisson's ratio defined as 0.499. While for the PTFE based composite material, it is compressible and the compressibility varies with the compound and manufacture process. Its Poisson's ratio must be obtained experimentally.

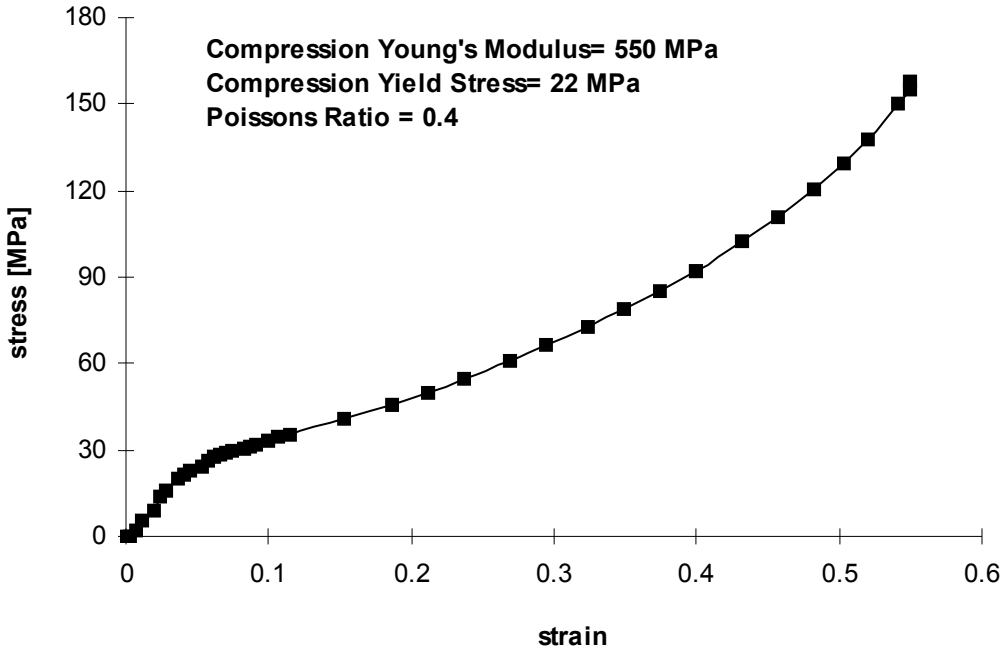

Figure 5.2: Measured stress-strain curve during compression.

During the deformation analysis, since the previous chosen element type PLANE183 is incapable of handling the multilinear option, it only applies to the rod, housing and energizer. PLANE82 is applied for the PTFE sealing element, which is also an 8 nodes 2D high order element. Also for the contact algorithm, the option for Contact stiffness update should be "Each iteration based on current mean stress of underlying elements (individual element based)" to ensure the smoothness of the static contact pressure.

Elements CONTA172 and TARGE169 are still used for the contact analysis. As shown in Figure 5.3, there are four contact pairs are defined in this analysis: 1. the contact between the PTFE contact element and the rod; 2. the contact between the PTFE contact element and the housing; 3. the contact between the rubber energizer and the

housing; 4. the contact between the PTFE contact element and the rubber energizer. In general, any time a soft material comes in contact with a hard material, the problem may be assumed to be rigid-to-flexible. For this analysis, since the stiffness of the materials have the following relation:

$$E_{steel} \gg E_{PTFE} \gg E_{rubber} \tag{5.1}$$

all of the contacts still falls into rigid-to-flexible category. In rigid-to-flexible contact problems, if a contacting surface has a much higher stiffness relative to the deformable body it contacts, it is treated as rigid and the other deformable body is treated as contact. For contact pair 1, the rod is the target surface and the PTFE sealing element is the contact surface; for contact pair 2, the housing is the target surface and the PTFE sealing element is the contact surface; for contact pair 3, the housing is the target surface and the rubber energizer is the contact surface; for contact pair 4, the PTFE sealing element is the target surface and the rubber energizer is the contact surface. PTFE, most well known by the DuPont brand name *Teflon*, is noted for its low friction. The dry contact coefficient is less than 0.1, which is much smaller than that of polyurethane.

Figure 5.3 shows the applied boundary conditions. The red curves indicate the region of added surface load from oil pressure, and there are 3 boundary nodes need to be identified. The procedure of determining the boundary nodes is described in Chapter 3.

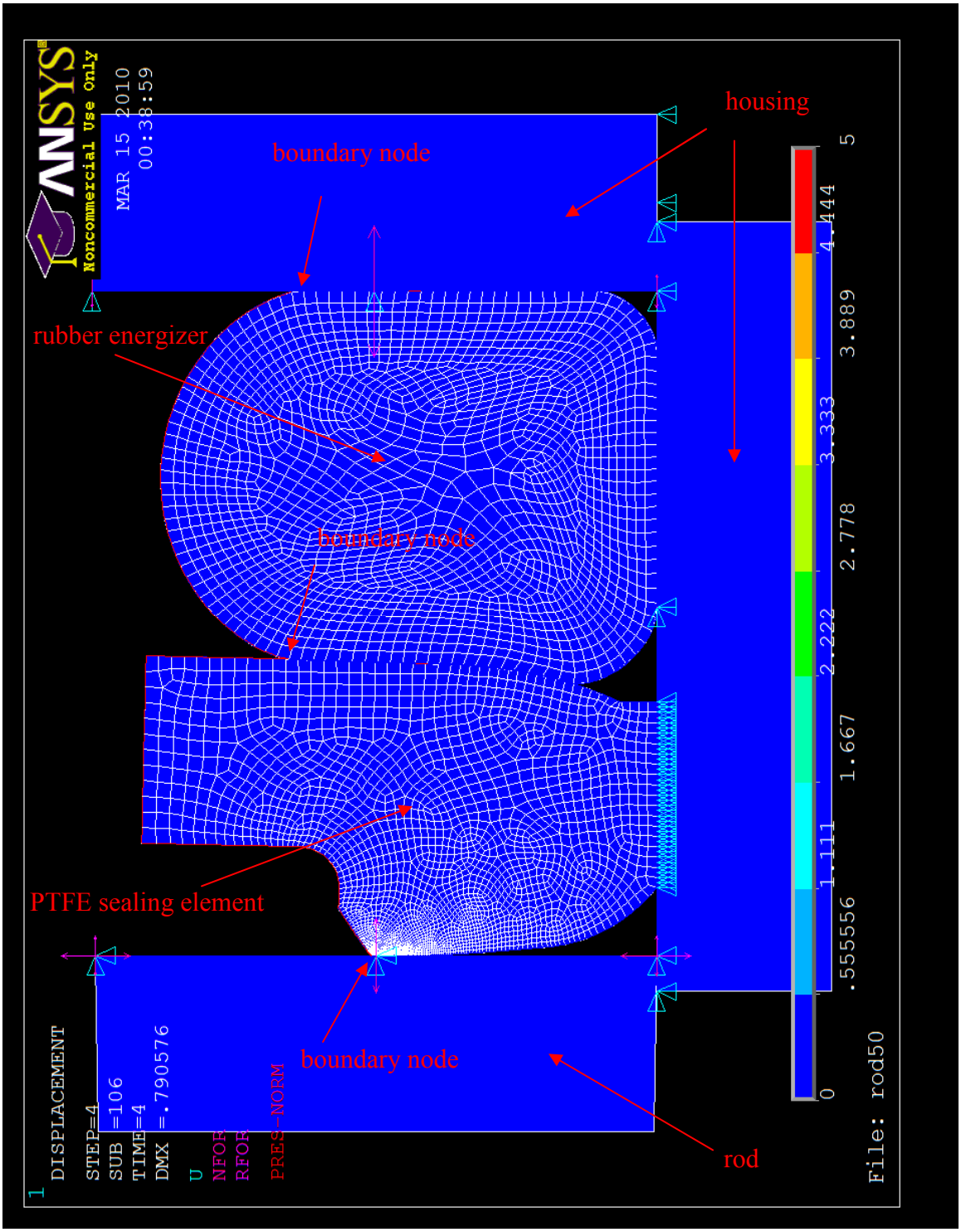

Figure 5.3: Boundary conditions of step seal.

Figure 5.4 shows the static pressure distributions for a sealed pressure of 5MPa, which are derived by using the linear elastic incompressible model, the linear elastic compressible model, and the multilinear compressible model respectively. For the linear models, the initial Young's Modulus of 550 MPa is used. It is noted that the maximum static contact pressures have a range from 90 MPa to 210 MPa and the curves are totally different. So it is very important to select a proper material model depending on the strain range.

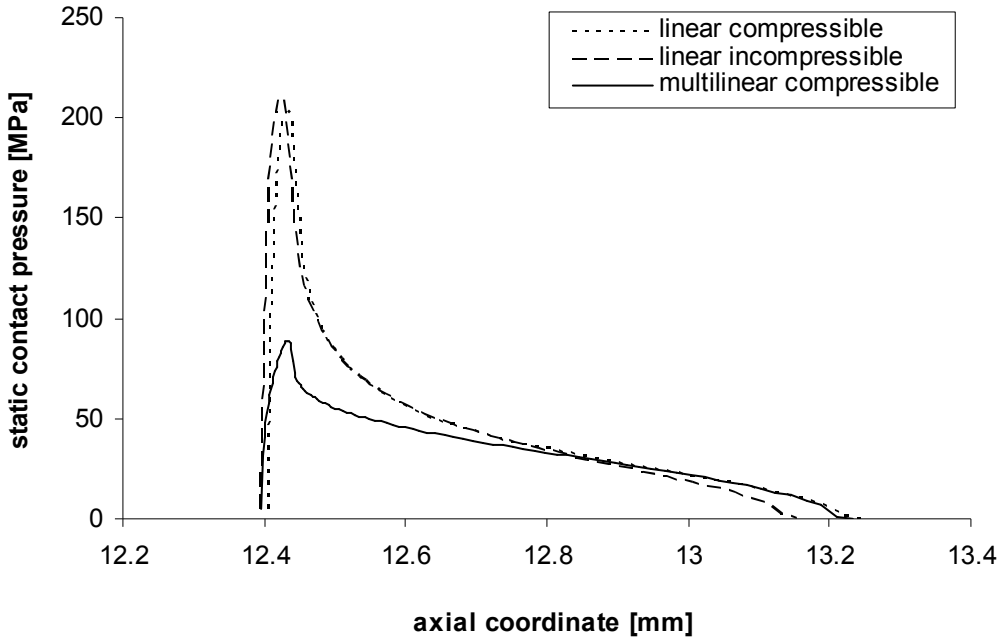

Figure 5.4: Static pressure distributions derived by various material models.

5.3.1 Roughness Measurement

Figure 5.5 shows the image of the surface of seal lip taken by a microscope. The yellow copper reinforcement can be observed.

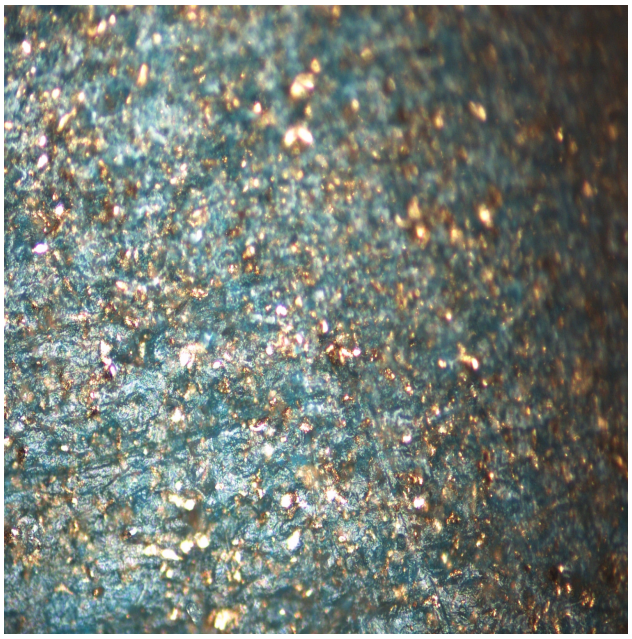

Figure 5.5: Surface image of PTFE sealing element.

The surface characteristics are measured experimentally. Figure 5.6 shows the surface measurements from a *ZYGO* optical profilemeter.

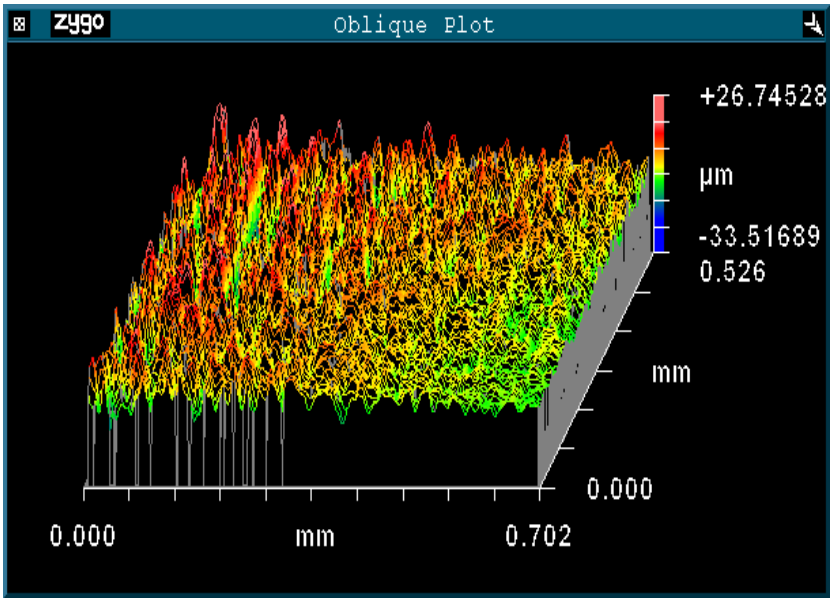

Figure 5.6: Surface map measurements from a *ZYGO* optical profilemeter.

Four groups of samples are measured. In average, the *RMS* roughness is estimated at 4 μm and the autocorrelation length is estimated at 30 μm and asperity density is estimated at $5\times10^{9}\ m^{-2}$.

5.4 Results

Computations have been performed for a typical step seal shown in Figure 5.1 and a double lip U-cup seal. The type of the double lip U-cup seal is the same as the one analyzed before but the diameter is half of that, which approximately equals that of the step seal. The base parameters are given in Table 5.1.

Table 5.1: Base parameters of the U-cup seal and the step seal.

	U-cup seal	Step seal
Seal type	Hallite type 605 U-cup seal	Trelleborg type RSK300500 step seal
Young's modulus	43 MPa	550 MPa
Poisson's ratio	0.499	0.4
Rod diameter	44.45 mm (1.75 in)	50 mm (1.97 in)
"Dry" friction factor	0.25	0.1
Aspect ratio, γ	1	
Sealed pressure - outstroke	0.1 MPa	
Sealed pressure - instroke	various	
Rod speed	various	
Sealed fluid	Mobil DTE 25 oil	
Viscosity	0.0387 Pa-s at 40 ^{o}C 0.0167 Pa-s at 66.5 ^{o}C 0.0058 Pa-s at 100 ^{o}C	
Reference viscosity	0.043 Pa-s	
Pressure viscosity index	20×10^{-9} Pa^{-1}	
Stroke length	228.6 mm (9 in)	

5.4.1 Leakage and Friction

Figure 5.7 shows plot of fluid transport vs. rod speed during the outstroke and instroke for the step seal. The sealed pressure is 20.7 MPa during the instroke and 0.1 MPa during outstroke. The RMS seal roughness is 4 μm. There exists a critical speed, below which the fluid transport during the outstroke is larger than the potential transport during the instroke, and there is net leakage. Conversely, above the critical speed there is no net leakage. Critical speed is a measurement of the effectiveness of the seal. The smaller the critical speed is, the more effective the seal. From Figure 5.7 the critical speed for the given condition is 0.036 m/s.

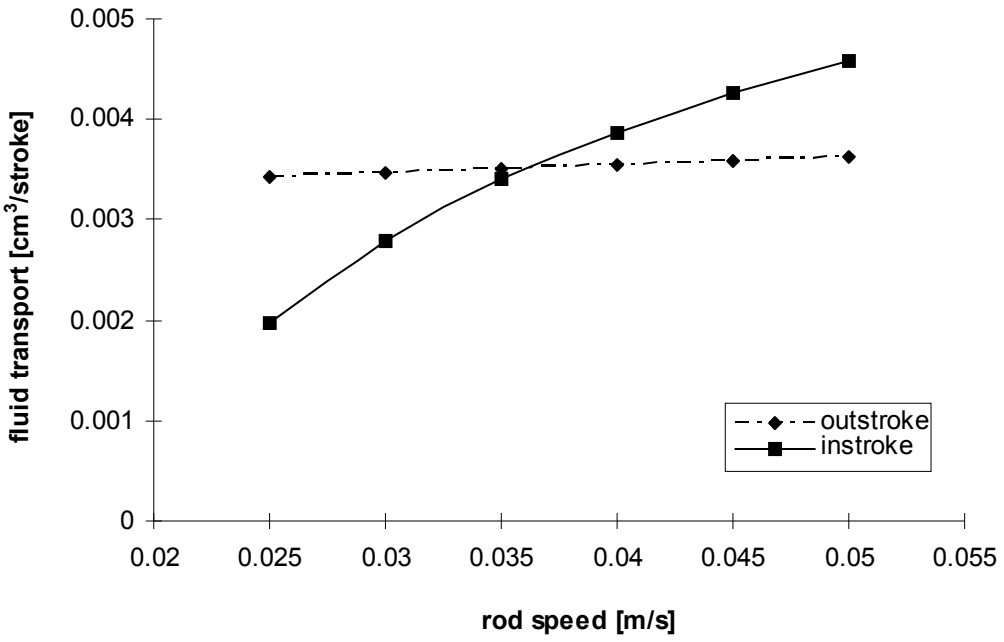

Figure 5.7: Fluid transport/stroke vs. rod speed, step seal, 20.7 MPa, 4 μm roughness.

Figure 5.8 shows the corresponding plot of fluid transport vs. rod speed during the outstroke and instroke for the U-cup seal. The critical speed, which is 0.075 m/s, is much

larger that that of the step seal. So from the critical speed point of view, at this operation condition, the step seal is superior to the double lip U-cup seal.

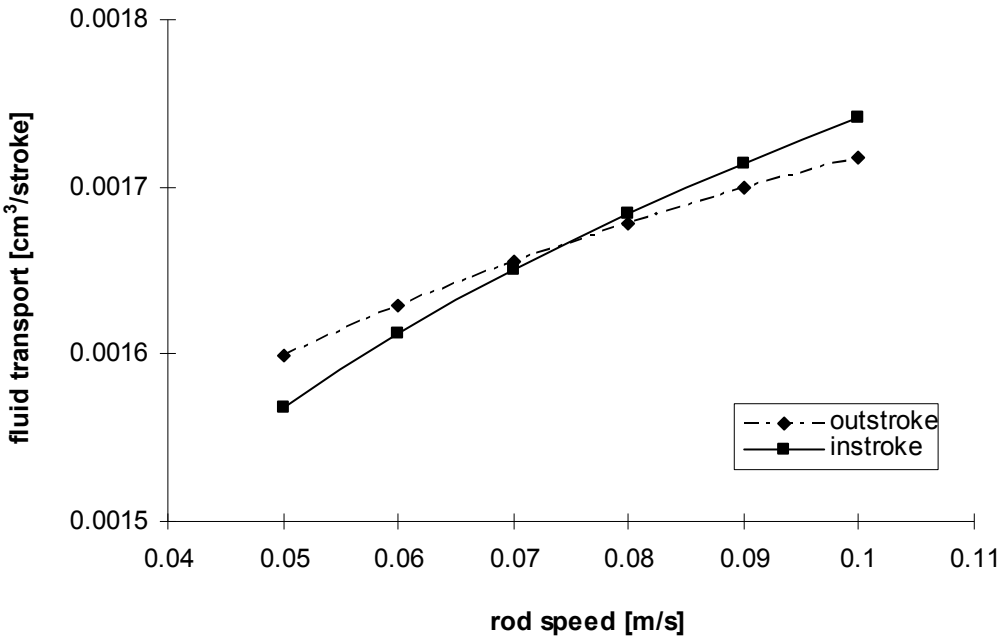

Figure 5.8: Fluid transport/stroke vs. rod speed, U-cup seal, 20.7 MPa, 0.8 μm roughness.

While leakage is of prime interest to the fluid power industry, the friction force on the rod can also be important. The friction force on the rod as a function of rod speed is shown in Figure 5.9 and Figure 5.10 respectively for the step seal and double lip U-cup seal. It is surprising that the friction force of the step seal is larger that of the double lip seal. The reason is although the friction coefficient of PTFE is much smaller than that of polyurethane; its static contact pressure is also much larger, because PTFE is more rigid than polyurethane. Combining these two effects, the frictional resistance of the two seals is comparable and the double lip U-cup seal is a little bit better.

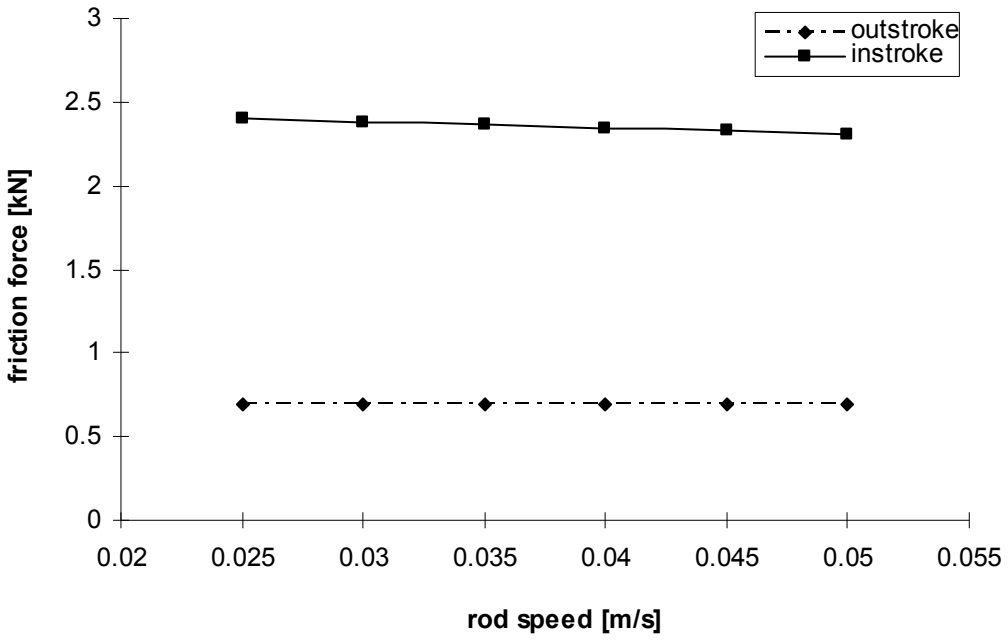

Figure 5.9: Friction force vs. roughness, step seal, 20.7 MPa, 4 μm roughness.

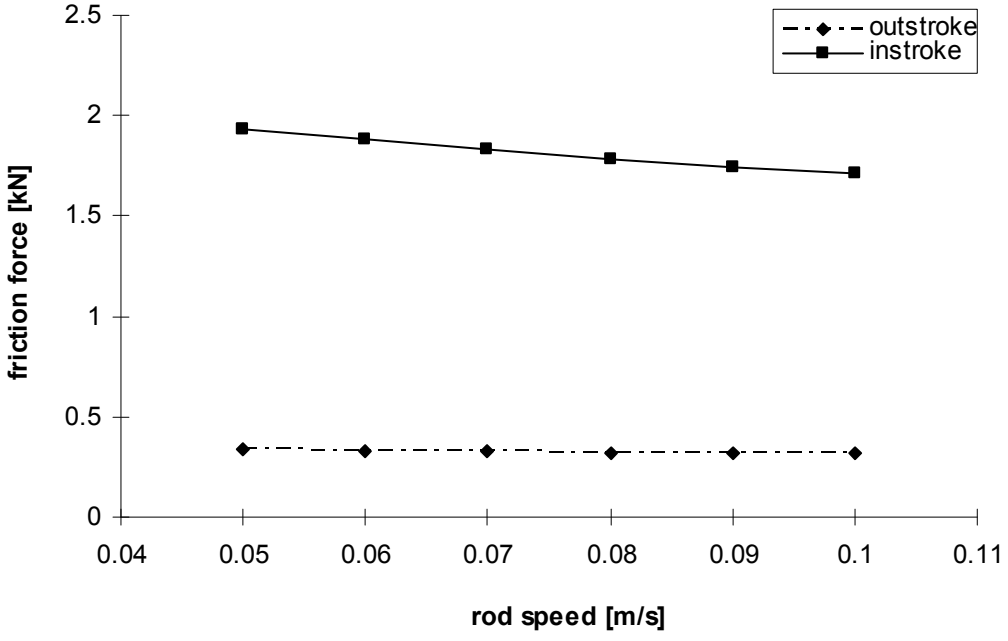

Figure 5.10: Friction force vs. roughness, U-cup seal, 20.7 MPa, 0.8 μm roughness.

Figure 5.11 and Figure 5.12 show plots of the computed net leakage per cycle vs. rod speed, for various sealed pressures (fixed stroke length). The behaviors of the two types of seals are similar, although the magnitudes of the leakage are higher for the U-cup seal. As rod speed increases, the leakage decreases until the critical speed is reached, above which the net leakage is zero. At a rod speed below the critical value, the higher the sealed pressure, the higher the leakage.

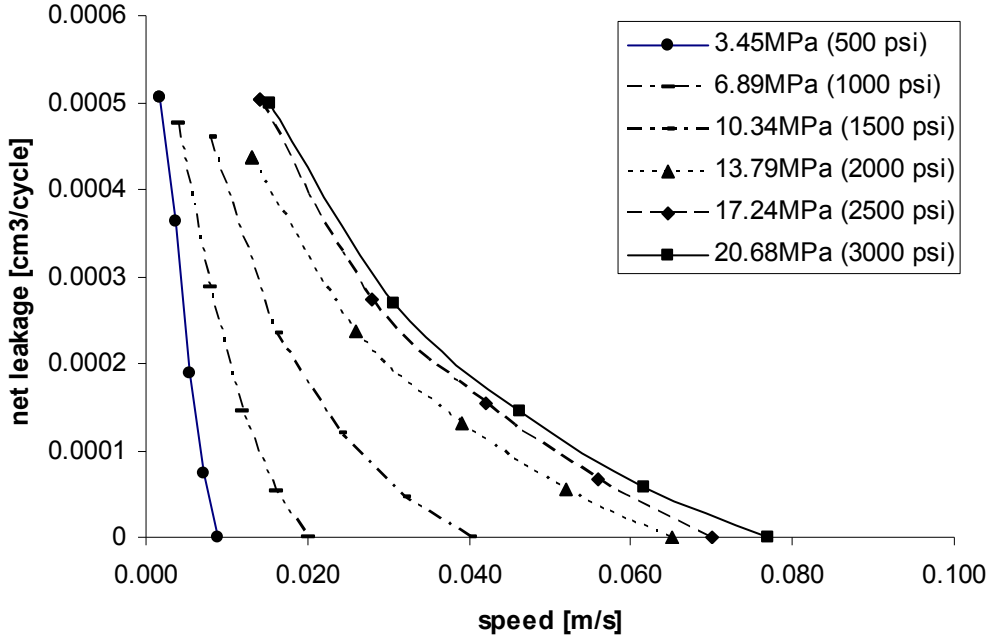

Figure 5.11: Net leakage/cycle vs. rod speed, U-cup seal, 0.8 μm roughness.

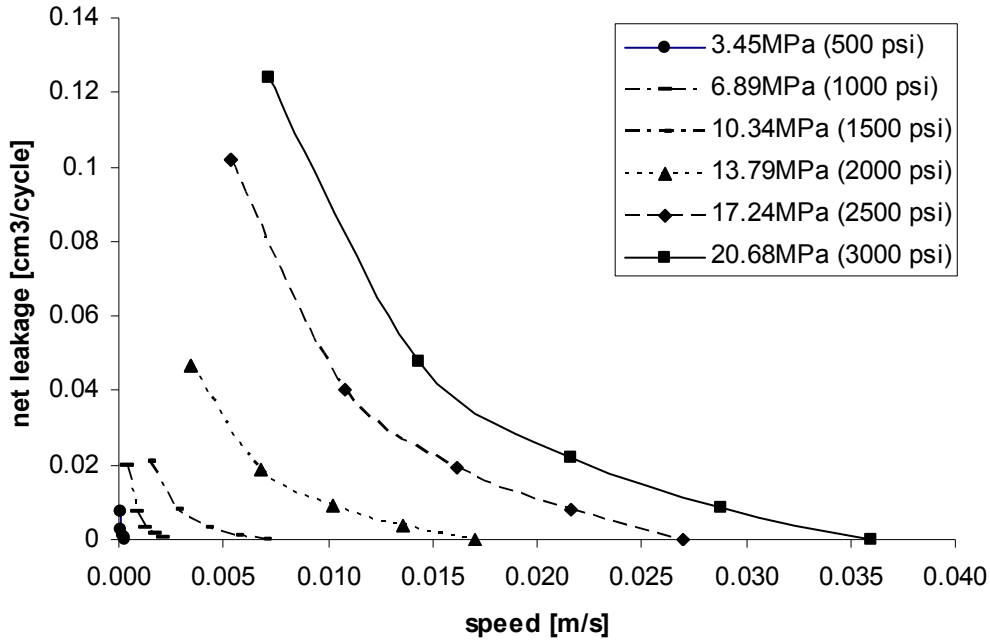

Figure 5.12: Net leakage/cycle vs. rod speed, step seal, 4 μm roughness.

Similar plots for various seal roughnesses are shown in Figure 5.13 and Figure 5.14. At a rod speed below the critical value, the higher the seal roughness, the higher the leakage.

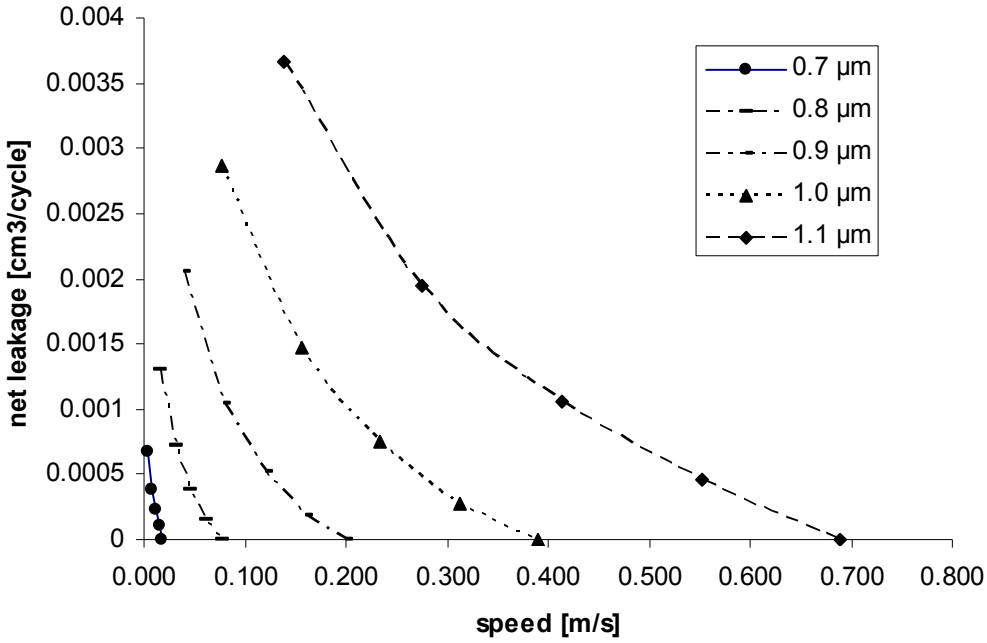

Figure 5.13: Net leakage/cycle vs. rod speed, U-cup seal, 20.7 MPa.

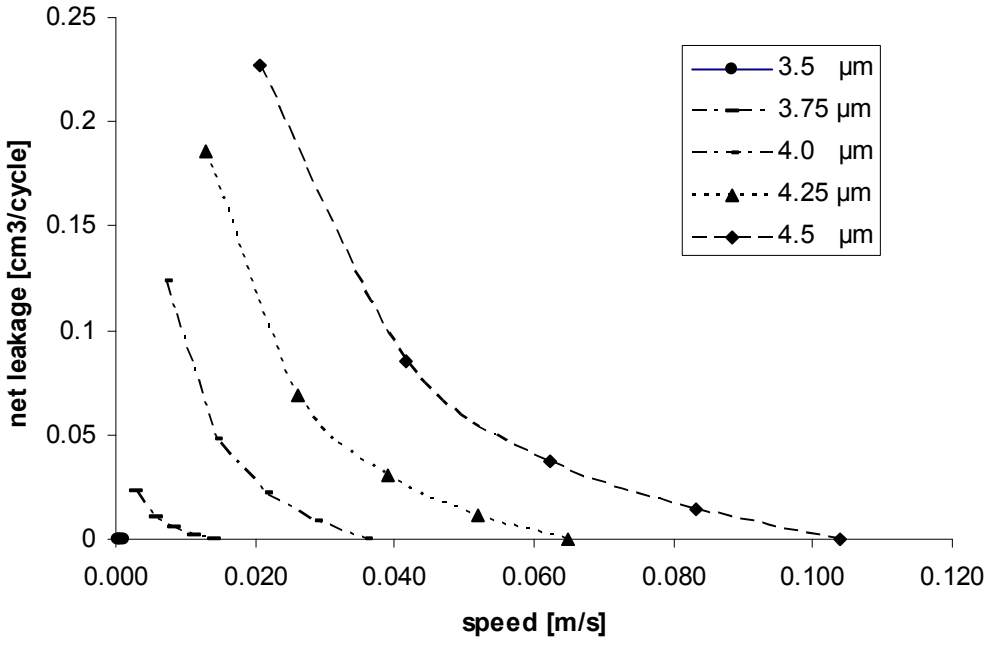

Figure 5.14: Net leakage/cycle vs. rod speed, step seal, 20.7 MPa

Figure 5.15 and Figure 5.16 show plots of the critical rod speed vs. seal roughness for various sealed pressures. As would be expected from Figure 5.11 - Figure 5.14, the critical rod speed increases with roughness and sealed pressure. From Figure 5.15 and Figure 5.16 it is seen that the critical speed for the U-cup seal is significantly higher than that of the step seal, especially for high pressures. From this point of view, the step seal is superior to the U-cup seal at the higher pressures (although the U-cup seal may have other advantages). This is consistent with the fact that the manufacturer's maximum pressure rating for the step seal, 40 MPa, is significantly higher than that for the U-cup seal, 20 MPa.

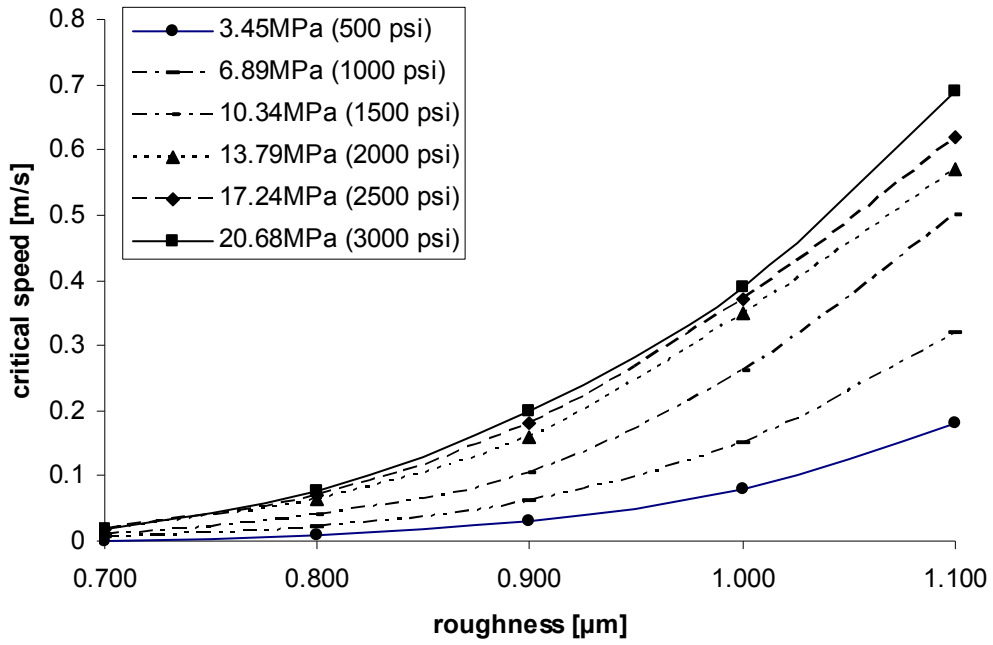

Figure 5.15: Critical rod speed vs. seal roughness, U-cup seal.

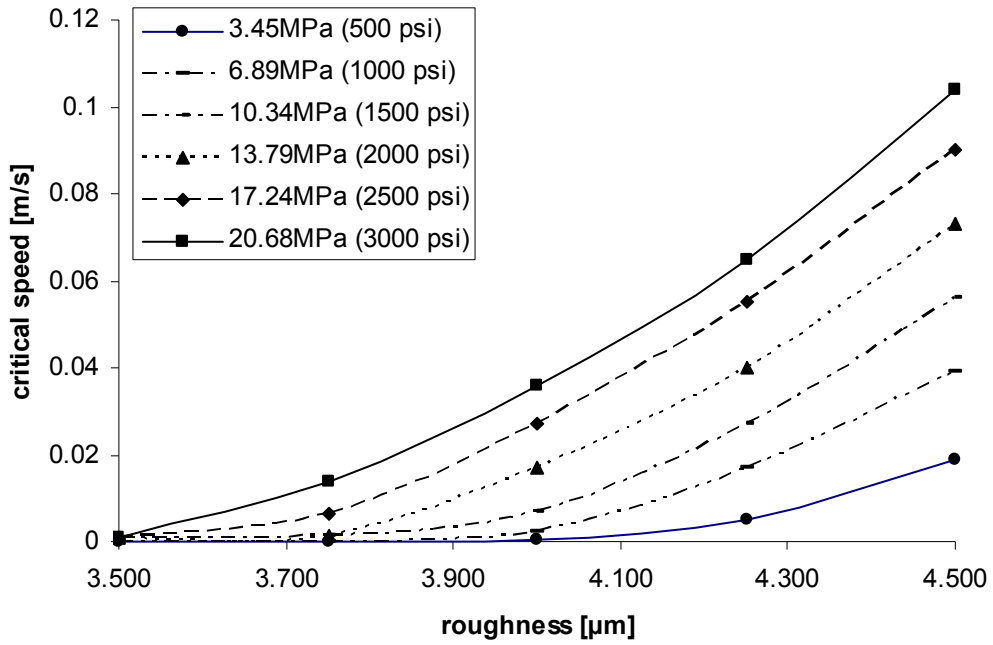

Figure 5.16: Critical rod speed vs. seal roughness, step seal.

5.4.2 Details of Sealing

To understand why the step seal exhibits superior performance at the higher pressures, the operation of the two seals at the same sealed pressure, 20.7 MPa, and the same rod speed, 0.05 m/s are compared. This operating point corresponds to zero net leakage for the step seal, but positive net leakage for the U-cup seal.

Figure 5.17 shows the non-dimensional film thickness distribution, for the step seal. The film is thicker during the instroke than during the outstroke. This is a favorable characteristic because a thicker film allows more fluid to be drawn into the cylinder during the instroke, thereby reducing the possibility of leakage. The corresponding film thickness distribution for the U-cup seal is shown in Figure 5.18. During the outstroke (zero sealed pressure) the two lips are distinct, while during the instroke (20.7 MPa

sealed pressure) the two lips are merged. For this seal, on the average the film thickness is smaller during the instroke than during the outstroke. This is an unfavorable characteristic. The magnitudes of the film thicknesses indicate that both seals operate with mixed lubrication.

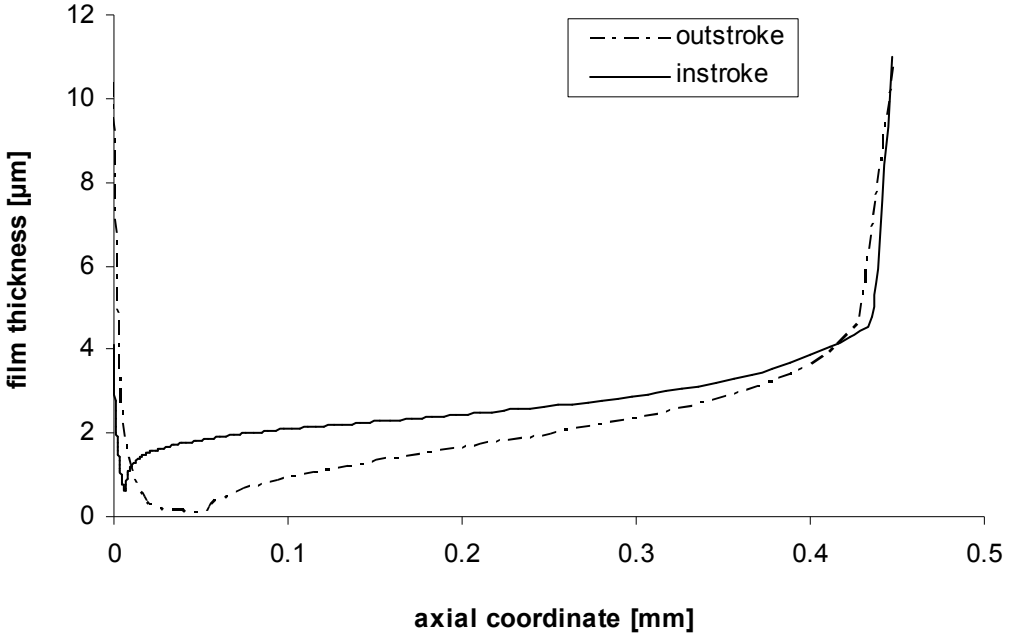

Figure 5.17: Film thickness distributions, step seal, 20.7 MPa, 4 µm roughness.

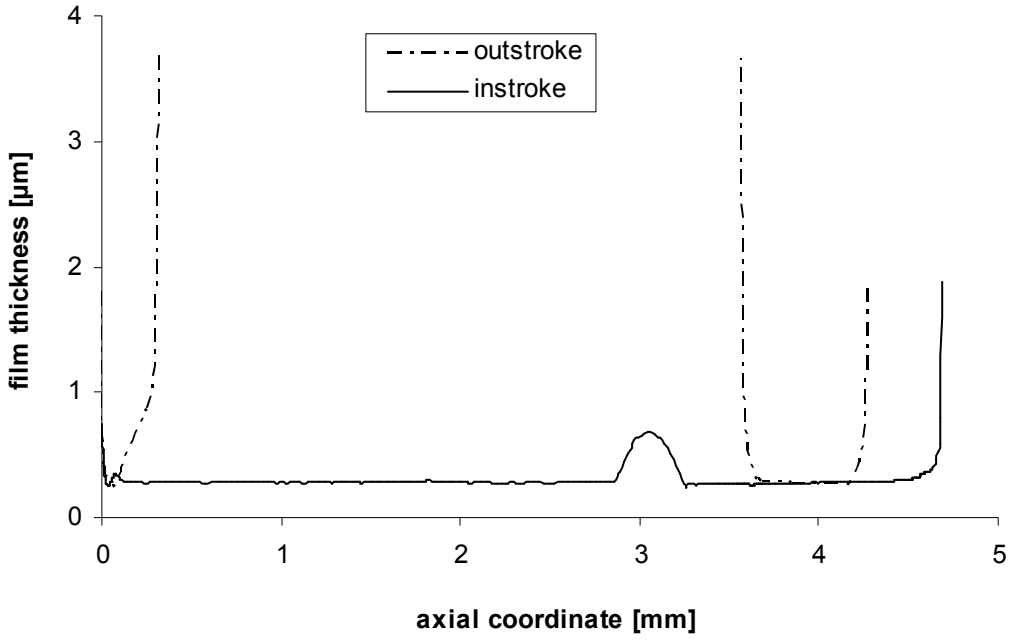

Figure 5.18: Film thickness distributions, U-cup seal, 20.7 MPa, 0.8 µm roughness.

Figure 5.19 and Figure 5.20 show the pressure distributions in the sealing zone for the two seals during the outstroke. The contact pressures are much higher for the step seal than for the U-cup seal. From the fluid pressure curves it is seen that the flow is cavitated over almost the entire sealing zone for the step seal. There is also a great deal of cavitation for the U-cup seal; however the entire film under the secondary lip and a portion of the film under the primary lip are uncavitated. Since cavitation is a favorable characteristic during the outstroke, restricting the flow of fluid out of the cylinder, the step seal is somewhat superior in this regard.

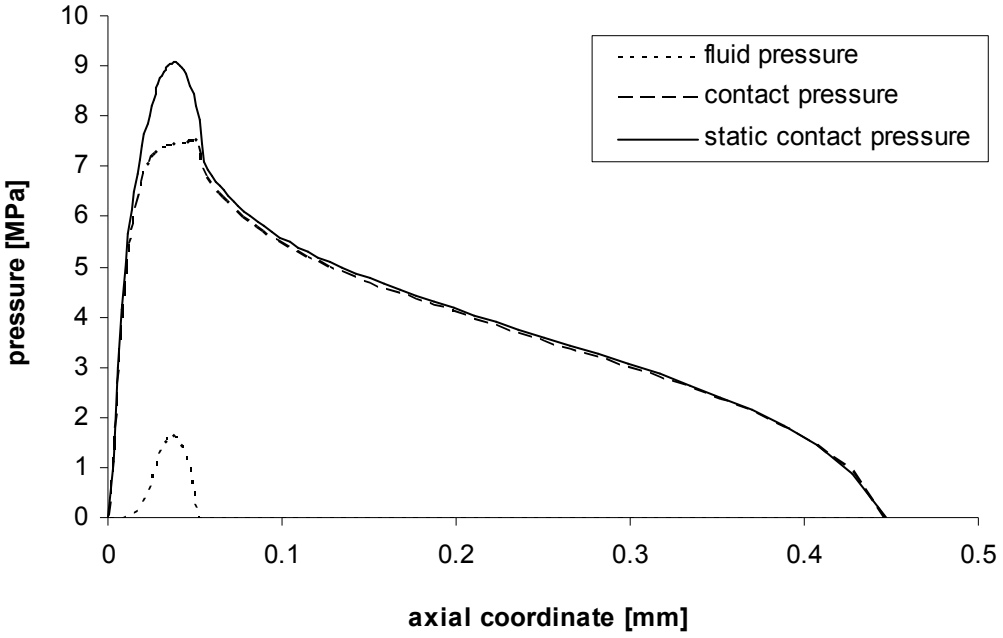

Figure 5.19: Pressure distributions, outstroke, step seal, 20.7 MPa, 4 μm roughness.

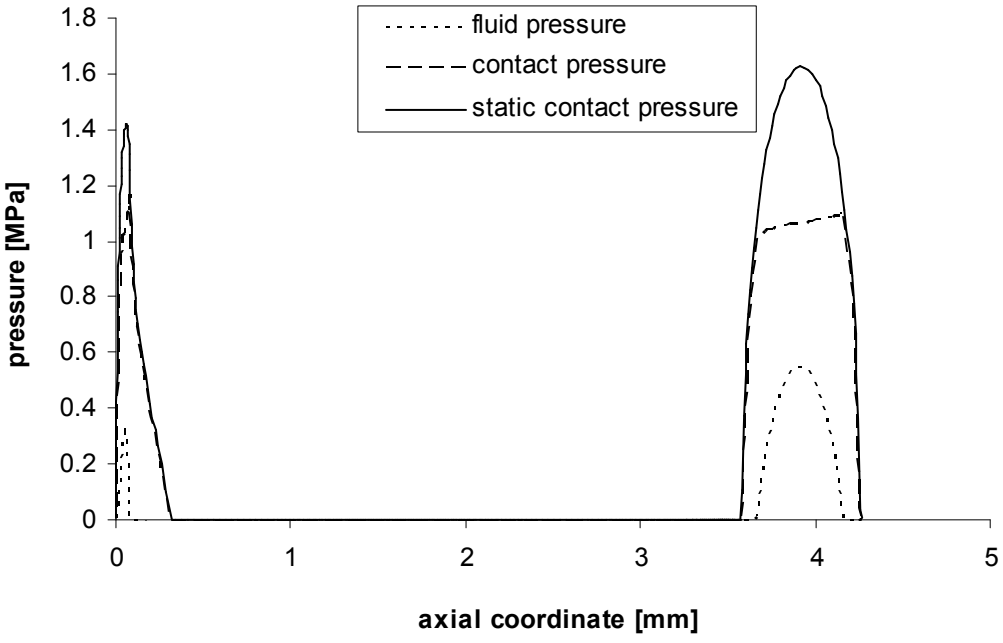

Figure 5.20: Pressure distributions, outstroke, U-cup seal, 20.7 MPa, 0.8 μm roughness.

Figure 5.21 and Figure 5.22 show the pressure distributions for both seals during the instroke. No cavitation occurs for the step seal while a portion of the film of the U-cup seal is cavitated (where the two lips have merged). Since cavitation during the instroke is unfavorable, restricting the flow of fluid back into the cylinder, the step seal again is superior in this regard.

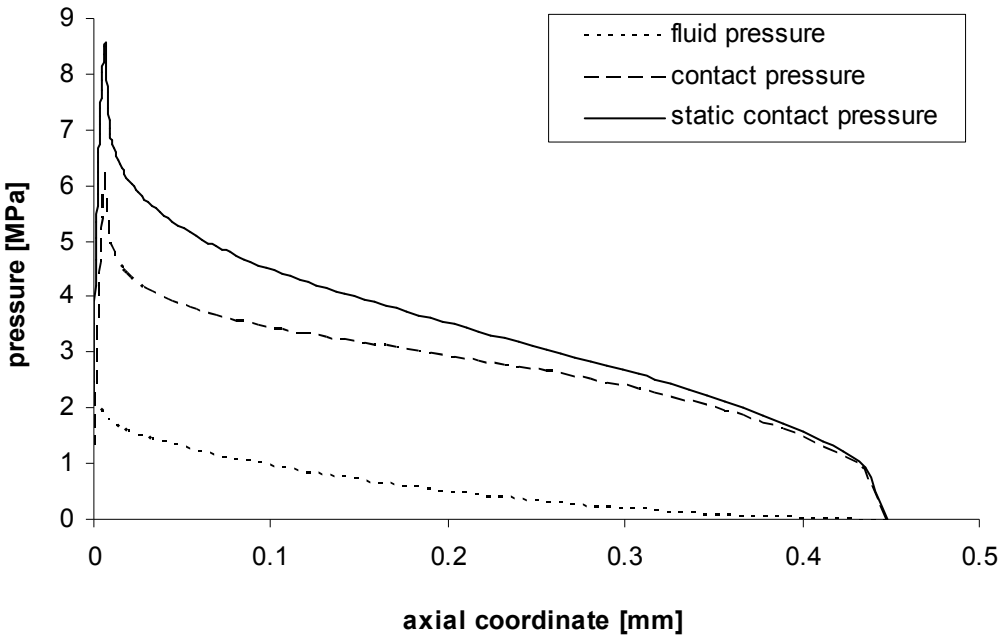

Figure 5.21: Pressure distributions, instroke, step seal, 20.7 MPa, 4 μm roughness.

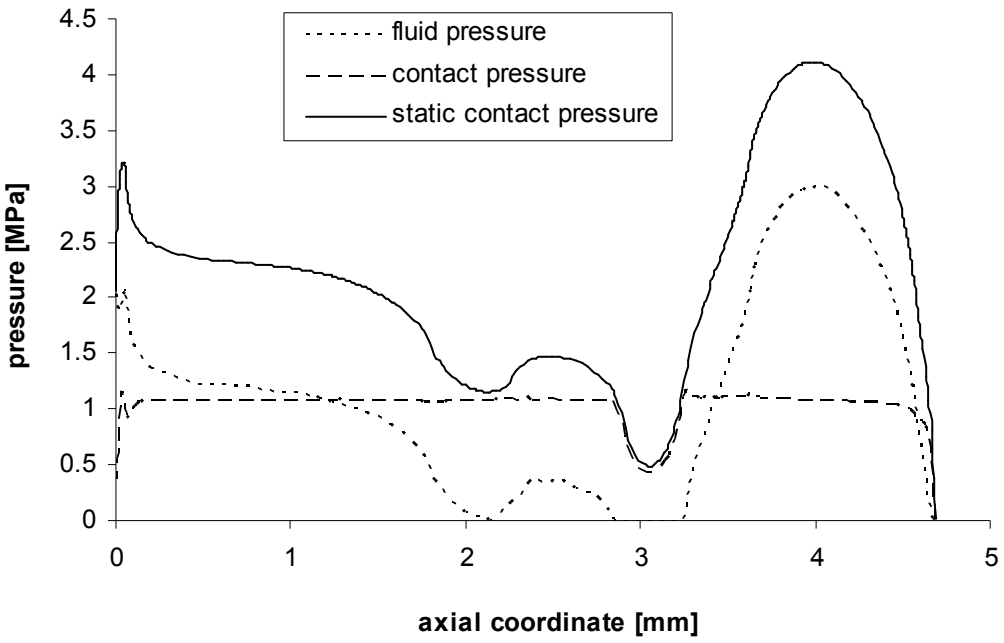

Figure 5.22: Pressure distributions, instroke, U-cup seal, 20.7 MPa, 0.8 μm roughness.

5.5 Conclusions

The results of this study indicate that rod seal leakage is strongly dependent on the rod speed, the sealed pressure and the seal roughness, for a given seal design and stroke length. There exists a critical rod speed, below which the seal will leak, while above which there will be zero net leakage. The critical rod speed depends on the seal design, the sealed pressure and the seal roughness. Comparison of a double lip U-cup seal with a similar size step seal indicates the step seal has a lower critical rod speed.

This study also confirms the conclusions of earlier studies that rod seals generally operate with mixed lubrication, and that the following characteristics promote reduced or zero net leakage:

- thicker lubricating film during instroke than during outstroke,

- cavitation in film during outstroke,
- reduced cavitation in film during instroke.

5.6 Validation

The model is validated through comparisons of model predictions with experimental measurements and observations by industry partners.

5.6.1 Leakage Measurement of Double Lip U-cup Seal

The measurements are conducted at our industry partner Eaton Hydraulics Company. The test bed is designed to measure the net leakage of hydraulic cylinder rod sealing systems under varying operating conditions, specifically the rod speed and sealed pressure. There are three basic components included in the design: driving cylinders, test fixtures and related hydraulic system, which are shown on the Figure 5.23. Figure 5.24 shows how the leaked oil is collected then weighed.

The test fixtures consist of foot mount, double end cylinders that are designed without pistons. The driving cylinders cycle the piston rods back and forth within the test fixtures and the velocities are controlled with valves. The test fixtures are alternately pressurized and vented by the Seal Test Power Unit. This pressure cycle is synchronized with the piston rod movement so that the seals being tested are pressurized to the designed test pressure while the test rods are traveling in one direction and vented to tank while traveling in the opposite direction.

The hydraulic system includes Driving Cylinder Power Unit and Seal Test Power Unit, which consists of motor, pump, reservoir and related hardware. The Driving Cylinder Power Unit provides the hydraulic power needed to operate the driving

cylinders and the Seal Test Power Unit provides the hydraulic test fluid and power needed to operate the test fixtures.

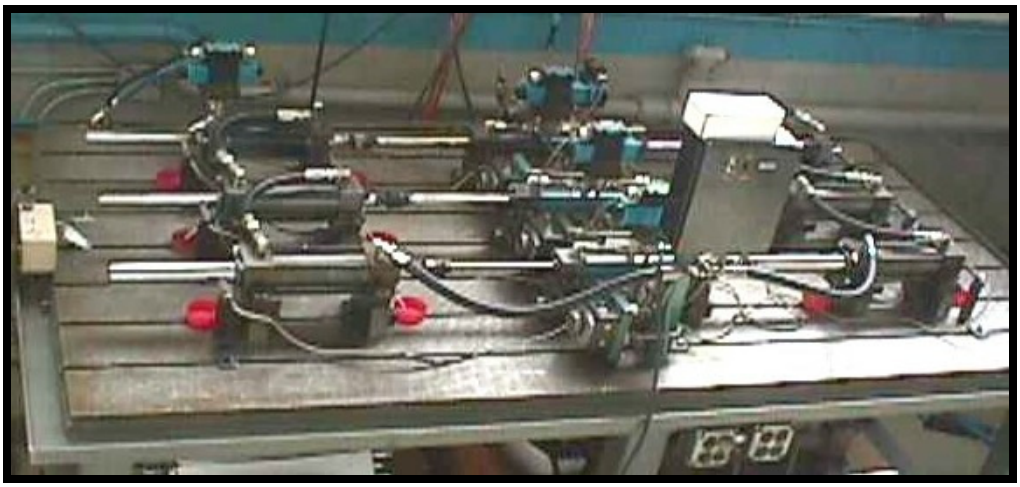

Figure 5.23: Test bed in Eaton.

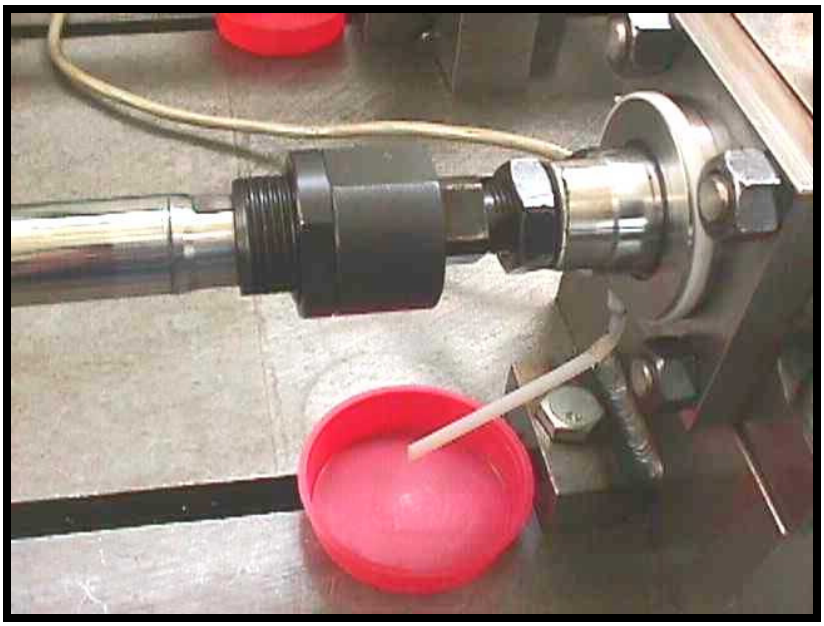

Figure 5.24: Leaked oil collection.

Tests have been performed with parameters given in Table 5.2.

Table 5.2: Test operation parameters.

Seal	Hallite type 605 U-cup
Sealed pressure - outstroke	0
Sealed pressure - instroke	1000 psi
Rod speed	1 in/s – 32 in/s
Rod diameter	44.45 mm (1.75 in)
Stroke length	228.6 mm (9 in)

Test procedure:

1. 24 hour run-in at 1000 psi and 10 in/s.
2. 24 hour run at 1000 psi and 1 in/s, 2 in/s, 3 in/s, 4 in/s, 5 in/s, 6 in/s, 8 in/s 16 in/s, 32 in/s.
3. After each 24 hour run, measure leakage.
4. The seals are removed from the test fixtures and examined by microscope. The test fixtures are disassembled and cleaned.

Summary of Results:

Three series of tests have been performed; the measured total leakage rates are listed in Table 5.3.

Table 5.3: Leakage measurements of the U-cup seal.

	Seal #1	Seal #2	Seal #3	Seal #4
Test series 1	79.833 g	6.103 g	18.115 g	0.853 g
Test series 2	0.000 g	0.203 g	0.000 g	0.416 g
Test series 3	0.052 g	0.793 g	0.287 g	0.161 g

5.6.2 Comparison with Model Prediction of Double Lip U-cup Seal

For test series 1, there is a strong variation of leakage with speed for seal #1, #2 and #3. Figure 5.25 shows the measured accumulate leakage versus time. Profilometer measurements indicated defects in lips of these seals; these may results from the debris in test fixture. For test series 2 and 3, after 240 hours running, the leakages are less than 1g, which means effectively no leakage.

Figure 5.26 shows the model predicted fluid transport vs. rod speed for the given seal. It's found that the critical speed is 0.89 in/s for this seal. For the test speeds from 1 in/s to 32 in/s, the seal should have no leakage. This is consistent with the experimental finding.

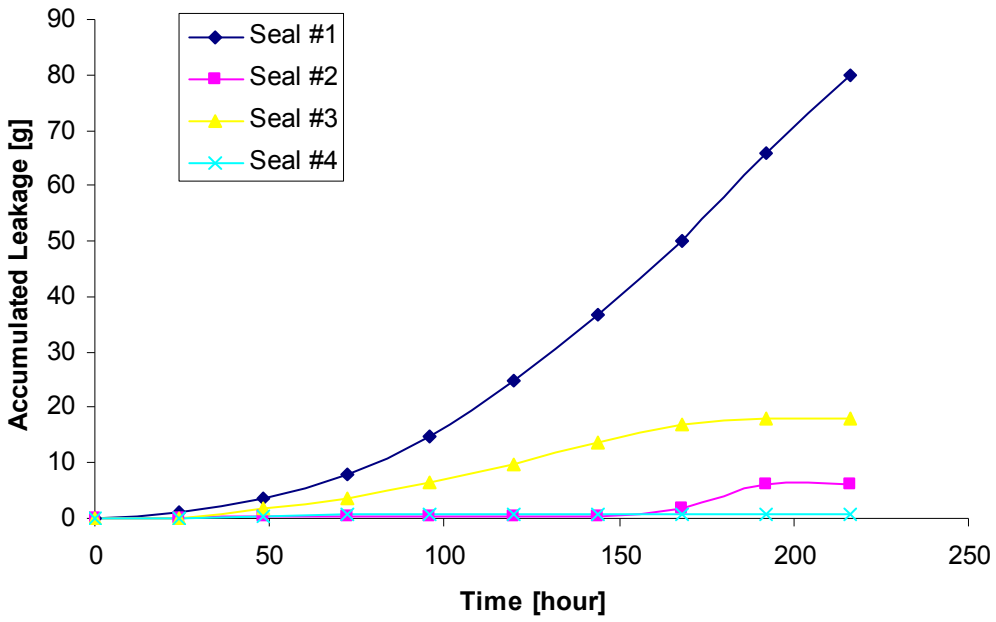

Figure 5.25: Accumulated leakage vs. time.

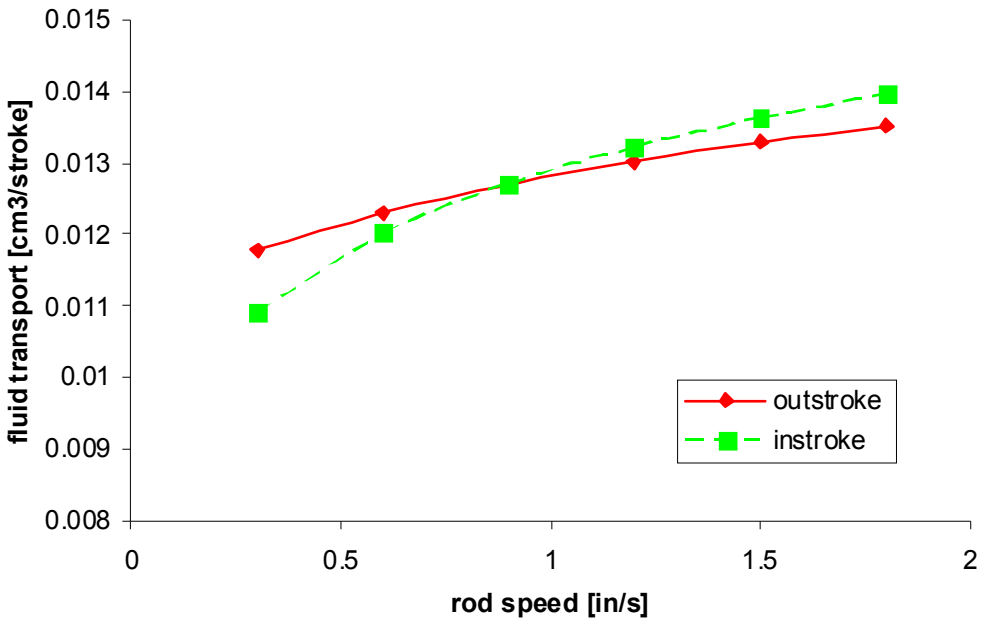

Figure 5.26: Fluid transport vs. rod speed.

5.6.3 Leakage Measurement of Step Seal

The measurements of the step seal is done by the seal manufacture Trelleborg Sealing Solutions Company. The test bed is similar to the previous test bed in Eaton, which is shown in the Figure 5.27.

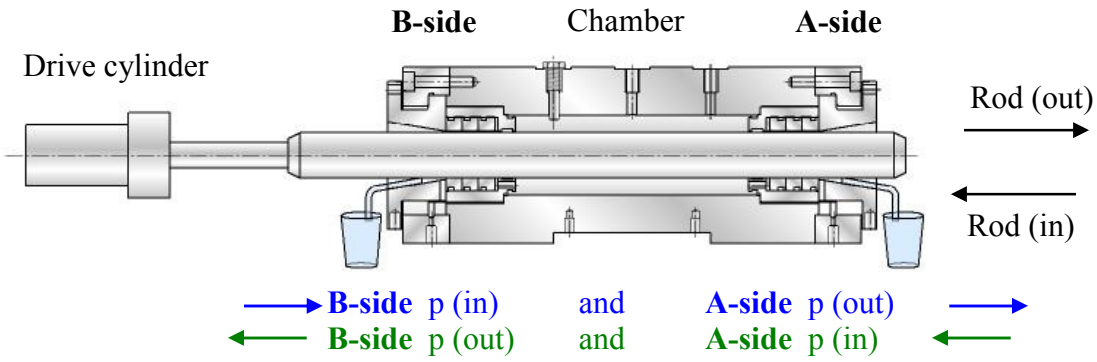

Figure 5.27: Test bed in Trelleborg.

Tests have been performed with base parameters given in Table 5.4.

Table 5.4: Leakage measurements of the step seal.

Seal	Trelleborg type RSK300500 step seal
Sealed pressure - outstroke	0
Sealed pressure - instroke	10 MPa – 30MPa
Rod speed	0.05 m/s – 0. 5 m/s (1.969 in/s– 19.69 in/s)
Rod diameter	50 mm (1.75 in)
Stroke length	228.6 mm (9 in)

Test procedure:

1. 110,000 cycles at 20 MPa, 0.2 m/s for run in.
2. 10,000 cycles at 10 MPa: 0.05 m/s, 0.2 m/s, 0.5 m/s.
3. 10,000 cycles at 20 MPa: 0.05 m/s, 0.2 m/s, 0.5 m/s.
4. 10,000 cycles at 30 MPa: 0.05 m/s, 0.2 m/s, 0.5 m/s.
5. Each time when pressure or speed changes, measure leakage.

Summary of Results:

Six seals have been tested; the measured accumulate leakage are shown in Figure 5.28 and the measured friction forces are shown in Figure 5.29.

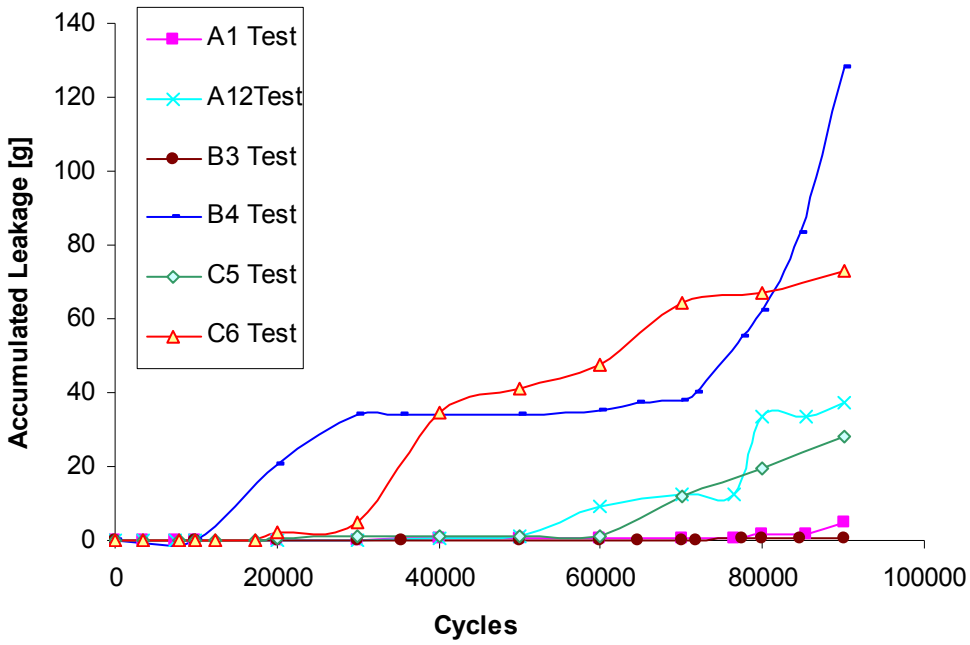

Figure 5.28: Accumulated leakage vs. cycles.

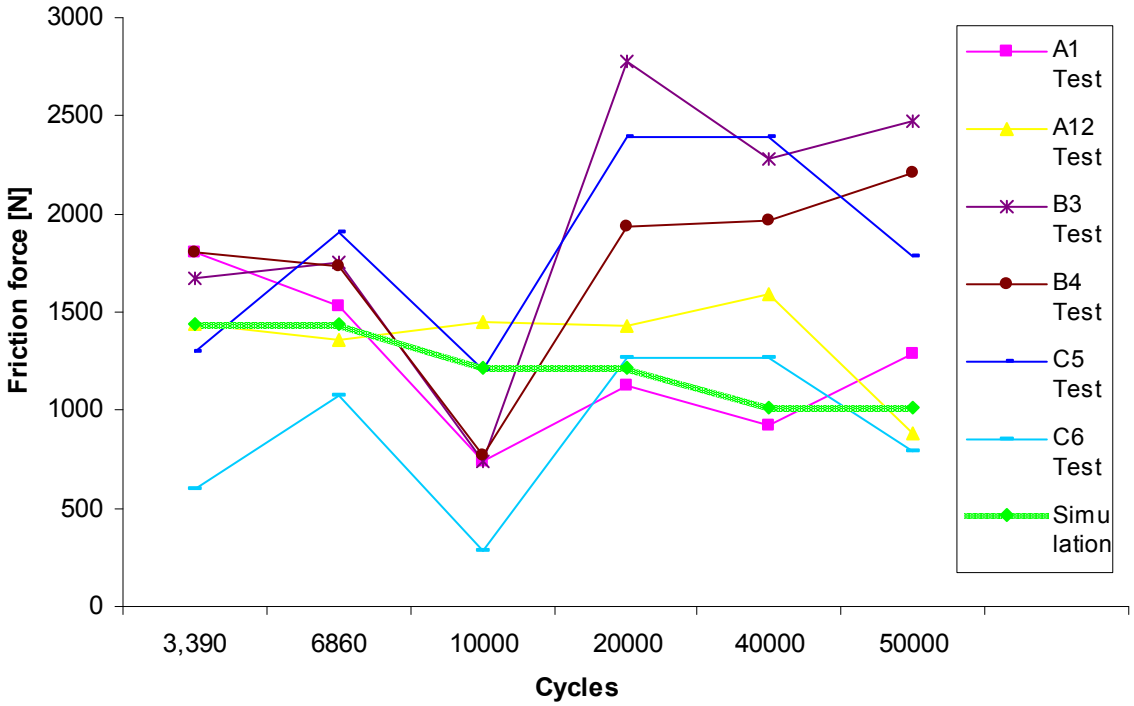

Figure 5.29: Friction force vs. cycles.

5.6.4 Comparison with Model Prediction of Step Seal

For seal A12, B4, C5, C6, leakage accumulates as the test proceeds. Profilometer measurements indicated various defects in the lips of these seals. Figure 5.30 shows a dent in the lip. For seal A1 and B3, which have no detected defects, after 80000 cycles, the leakages are less than 1g, which means effectively no leakage.

Figure 5.30: Damaged Part of the Seal.

Figure 5.31 shows the model predicted critical speed vs. sealed pressure for the given seal. For sealed pressure up to 30 MPa, the critical speed is less than 0.05 m/s, which is smaller than the given test speeds (0.05 m/s to 0.5 m/s). The seal should have no leakage. This is consistent with the experimental finding.

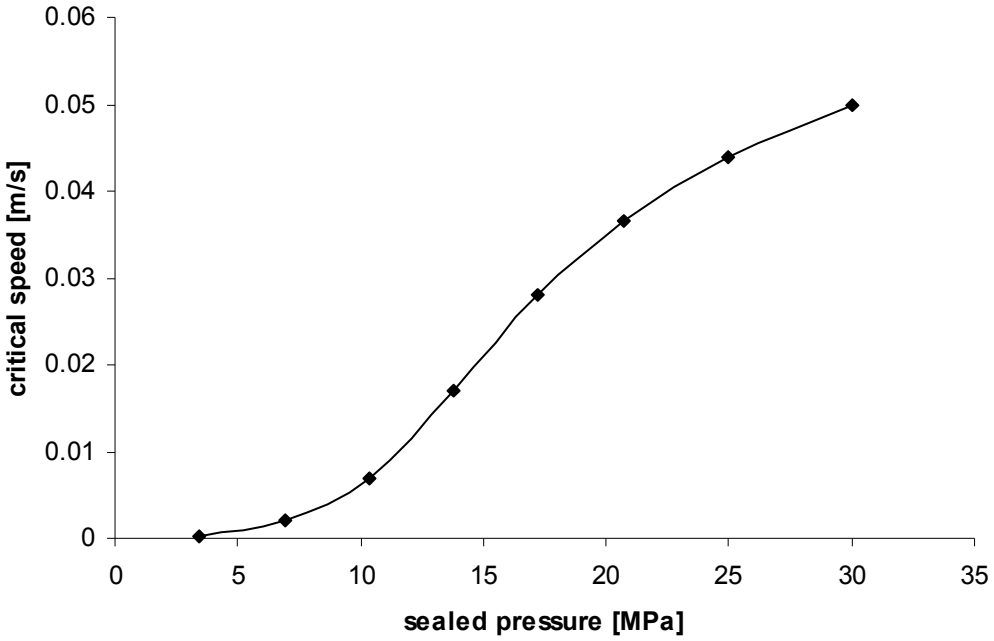

Figure 5.31: Critical speed vs. sealed pressure.

Figure 5.29 shows the friction force vs. cycles, one can see, that the model prediction is in accordance with measurement in scale.

CHAPTER 6

SEALS WITH SURFACE PATTERN

6.1 Introduction

To improve the effectiveness of reciprocating hydraulic rod seals, it is proposed that a micro-scale surface pattern be engineered into the seal surface in the sealing zone. A properly designed pattern would inhibit the fluid transport during the outstroke and augment the transport during the instroke.

The simulations of previous chapters have shown that these seals operate with mixed lubrication, there exists both a lubricating fluid film and asperity contact in the sealing zone, and seal roughness plays an important role in seal behavior. For a given seal design and set of operating conditions, there exists a critical roughness, above which the fluid transport during outstroke exceeds that during instroke and the seal will leak, while below which the transport during outstroke is less than that during instroke and the seal will be leakless. This roughness is a measure of the effectiveness of the seal. The lower the critical roughness, the more effective is the seal. For a given seal design, sealed pressure and seal roughness, there also exist a critical rod speed, below which the fluid transport during outstroke exceeds that during instroke and the seal will leak, while above which the transport during outstroke is less than that during instroke and the seal will be leakless. Therefore, the critical speed is also a measure of the effectiveness of the seal. In this analysis, we would like to design a pattern that has the minimum critical speed.

6.2 Seal Configuration

Figure 3.1 shows a schematic of a U-cup seal, the most common type of hydraulic rod seal, which is picked up as an example to show how the micro-scale surface pattern works.

Figure 6.1 shows the original concept of a sawtooth micro-pattern, to be placed on the lip surface in the sealing zone. The original rationale behind the use of the sawtooth micro-pattern was, referring to Figure 6.1, the thought that during the outstroke when the rod is moving from left to right, the steep slope of line 1-2 on the picture would retard the outflow of fluid, while during the instroke, the more gradual slope of line 2-3, would allow inflow with less resistance.

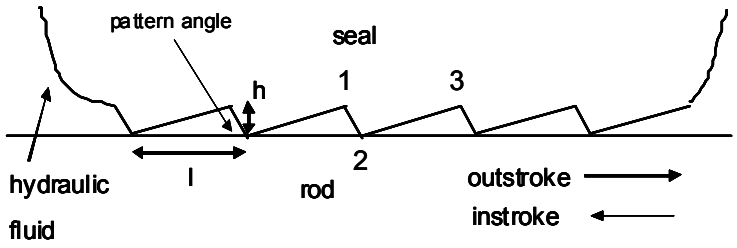

Figure 6.1: Sawtooth surface pattern, large pattern angle.

6.3 Analysis

A seal with the sawtooth pattern of Figure 6.1 has been simulated using the seal model and analysis described in detail in the previous chapters. Note for the double lip seal (see Chapter 4), the film thickness in the interlip region is on millimeter scale, which is comparable with the dimension in axial direction, so the interlip region is treated as an

oil reservoir and the analysis of the two lips are solved separately. Here, however, since the pattern depth is still on micrometer scale, which is much smaller than the pattern length, the Reynolds equation is valid for the entire sealing zone.

6.4 Results

The seal that has been simulated experiences ambient pressure during the outstroke and 6.9 MPa sealed pressure during the instroke. The sliding speed is the same during outstroke and instroke. Other parameters are the same as those defined in the analysis of the single lip seal, as shown in Table 3.1.

6.4.1 Leakage and Friction

Figure 6.2 is a plot of fluid transport vs. rod speed for both the outstroke and instroke of a seal with the micro-patterned seal surface and a corresponding seal without the micro-pattern. The pattern has a depth h of 20 μm, a pattern angle of 45^{o} and a pattern length l = 0.1 mm.

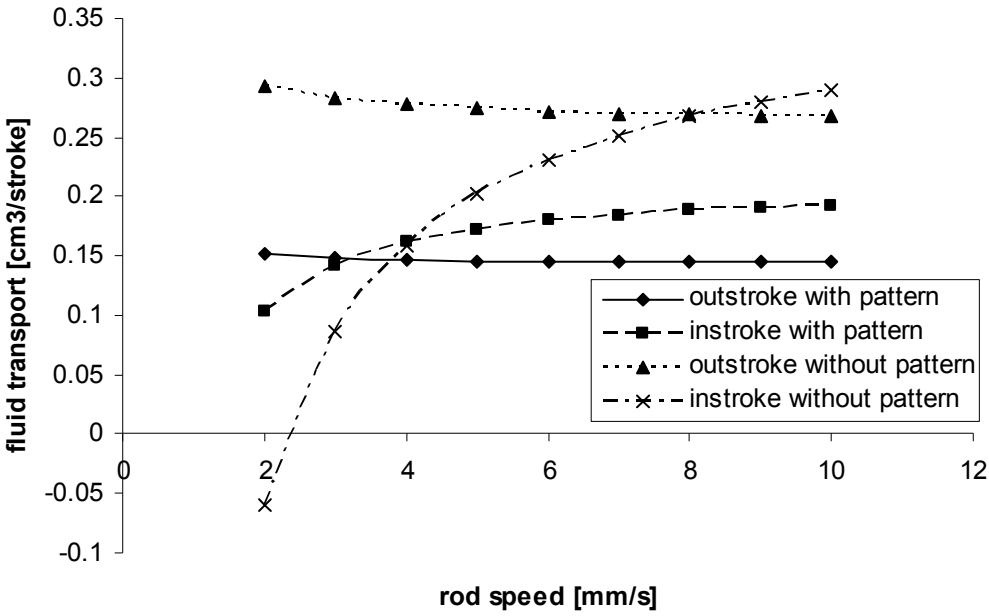

Figure 6.2: Fluid transport vs. rod speed

From the curves for the seal without the pattern, it is seen that for rod speeds above the critical rod speed of 8.12 mm/s, the fluid transport during the instroke exceeds that during the outstroke, indicating zero net leakage per cycle. For speeds below the critical speed, the seal leaks. Thus, as discussed earlier, the critical speed is a measure of seal effectiveness; the lower the critical speed, the more effective the seal. Comparing the curves in Figure 6.2, with and without the sawtooth pattern, shows that the pattern significantly reduces the critical speed from 8.12 mm/s to 3.16 mm/s. This is a substantial improvement in the effectiveness of the seal.

Figure 6.3 is a plot of critical speed vs. pattern depth h. The pattern angle is 45^{o} and the other two angles, going clockwise, are fixed at 14^{o} and 121^{o}. As the depth is increased from zero (no pattern), the critical speed decreases from 8 mm/s until at a depth

of approximately 20 μm it reaches a minimum of 3.16 mm/s, less than half of the value without the pattern. A further increase in depth results in an increase in the critical speed. Thus it is clear that the pattern depth must be on the micron-scale; a macroscopic pattern would not be effective.

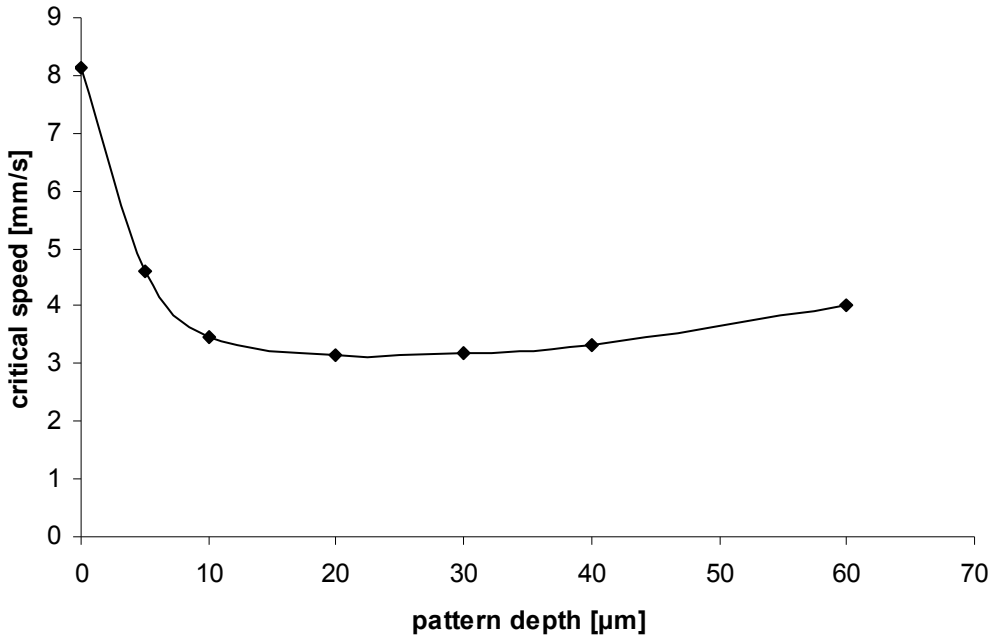

Figure 6.3: Critical speed vs. pattern depth.

The effect of the pattern angle on the critical speed is shown in Figure 6.4. The pattern depth is 20 μm and length l = 0.1 mm, from which, it can be derived that the pattern is symmetric when the pattern angle equals 22^o, The patterns with the pattern angle larger than 22^o has a shape like the one shown in Figure 6.1; the patterns with the pattern angle smaller than 22^o is illustrated in Figure 6.5.

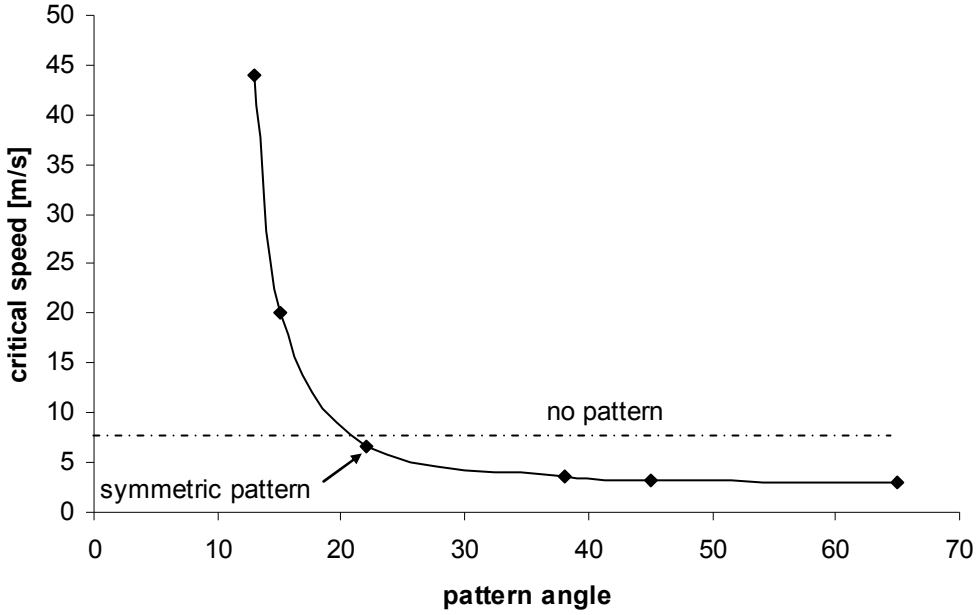

Figure 6.4: Critical speed vs. pattern angle.

From Figure 6.4 it is seen that the critical speed varies strongly with pattern angle, which is consistent with our prediction. In fact, a seal with the small pattern angle, such as that shown in Figure 6.5, is even worse than one without pattern. Combining Figure 6.4 and Figure 6.5, it can be found that the optimum pattern has a depth of 20 μm and an angle of 65^{o}.

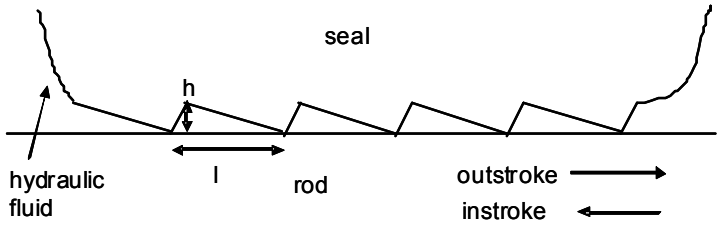

Figure 6.5: Sawtooth surface pattern, small pattern angle.

The effect of the sawtooth pattern on the friction force is seen in Figure 6.6 and Figure 6.7. The sliding speed is 5 mm/s. It is seen that the pattern produces a minimal change in friction force.

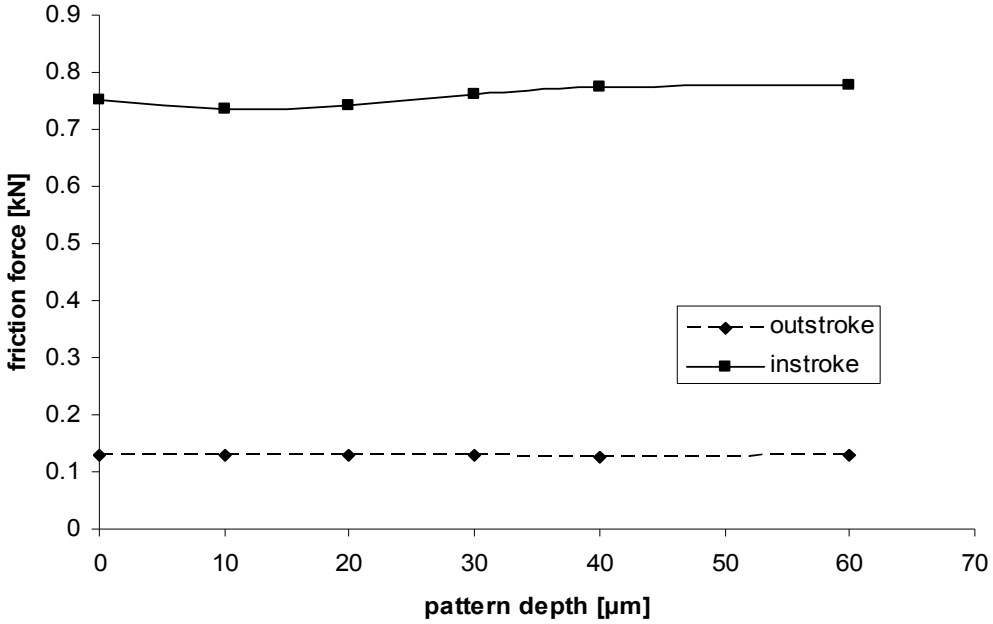

Figure 6.6: Friction force vs. pattern depth, 45^{o} pattern angle.

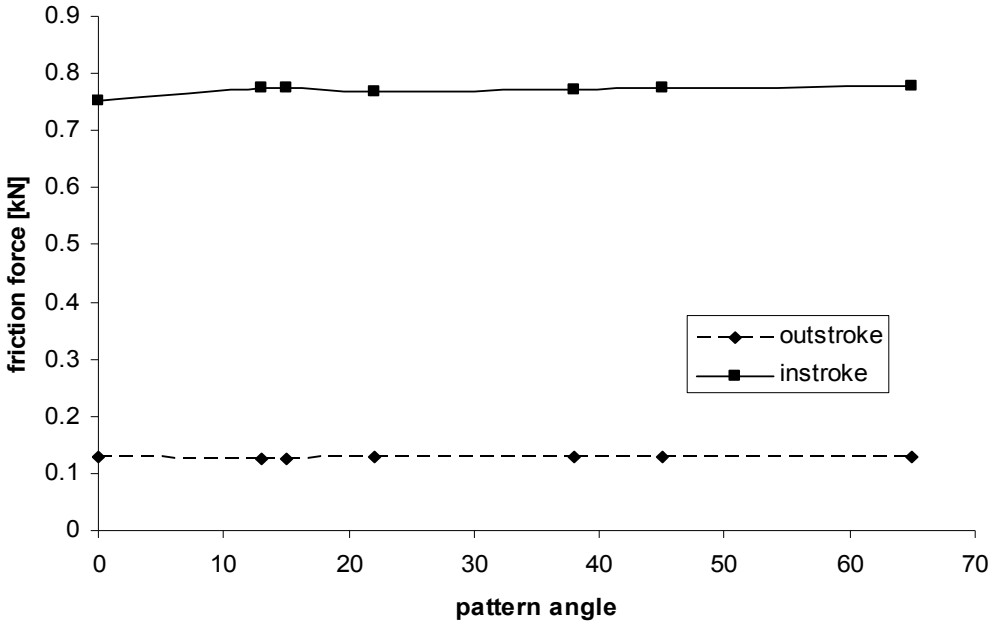

Figure 6.7: Friction force vs. pattern angle, 20 μm pattern depth

6.4.2 Details of Sealing

To understand how the pattern helped to reduce leakage, the details of the conditions in the sealing zone of a seal with optimum pattern is compared to that of the conventional seal without the pattern. The sliding speed is 5 mm/s, at which the conventional seal is leaking and the seal with pattern is non-leaking.

Figure 6.8 and Figure 6.9 show the contact pressure distributions (note that horizontal scales of the two figures are different). During the outstroke only four of the sawteeth are in the sealing zone, while during the instroke twenty-five are. For the patterned seal, there are sharp peaks at the tooth tips. During the outstroke, the peak

contact pressures at the tips are almost double the peak contact pressure for the conventional seal.

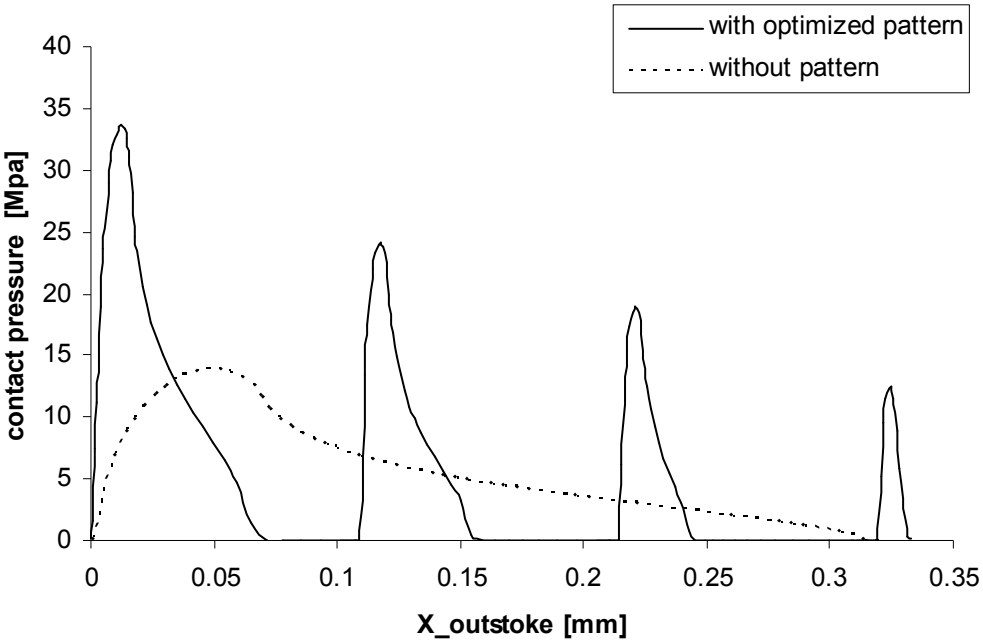

Figure 6.8: Contact pressure distribution, outstroke, 0.005 m/s.

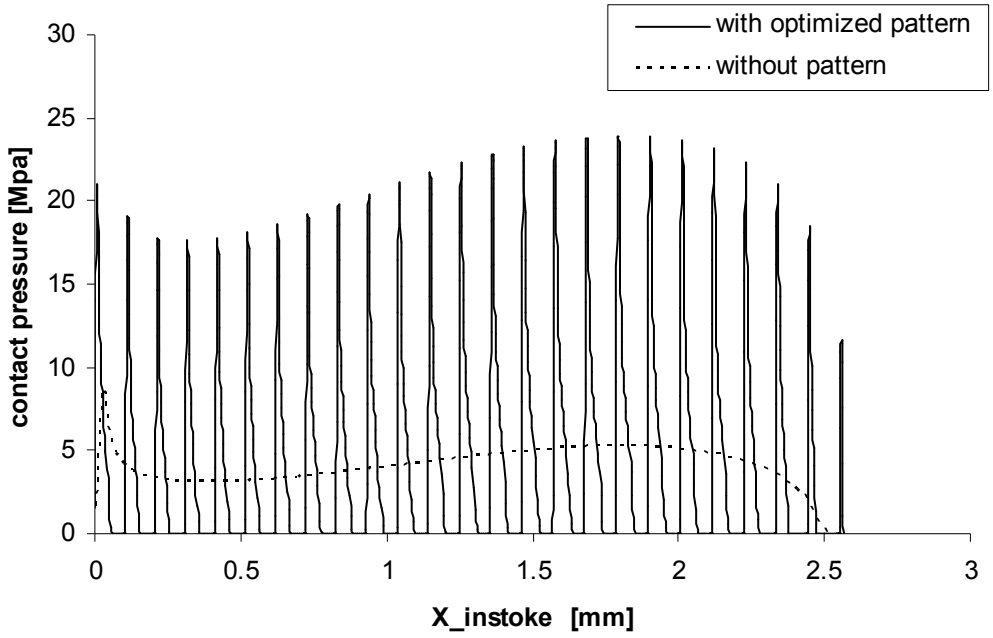

Figure 6.9: Contact pressure distribution, instroke, 0.005 m/s.

The fluid pressure distributions are shown in Figure 6.10 and Figure 6.11. During the outstroke, the pressure goes to zero over most of the sealing zone, both for the conventional seal as well as for the patterned seal. The fluid is cavitating in these regions.

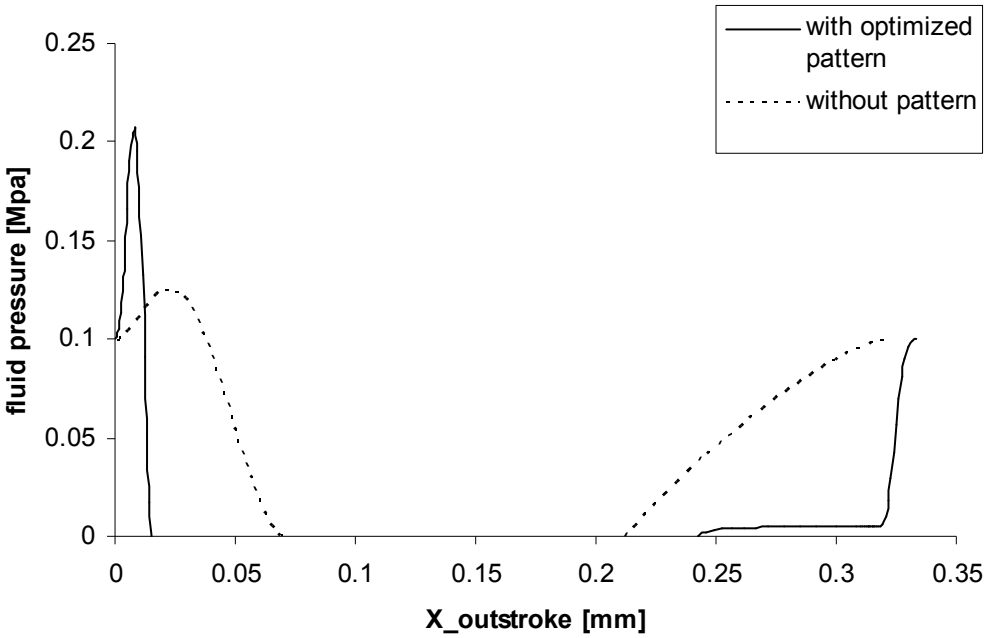

Figure 6.10: Fluid pressure distribution, outstroke, 0.005 m/s.

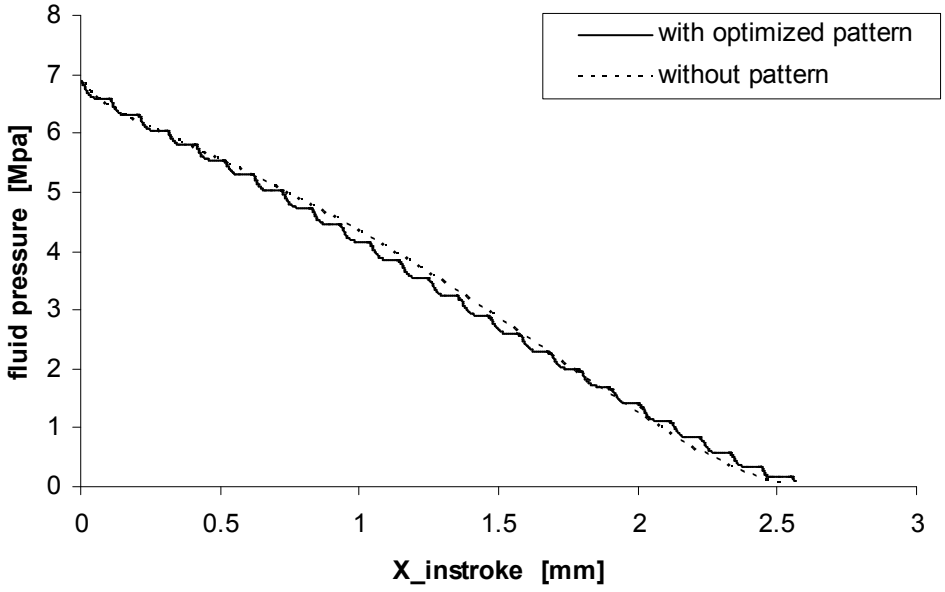

Figure 6.11: Fluid pressure distribution, instroke, 0.005 m/s.

Figure 6.12 shows this cavitating region in more detail. The dimensionless density is on the average lower with the patterned seal due to more intense cavitation. This is why the fluid transport during outstroke is lowered by the patterning, as shown earlier.

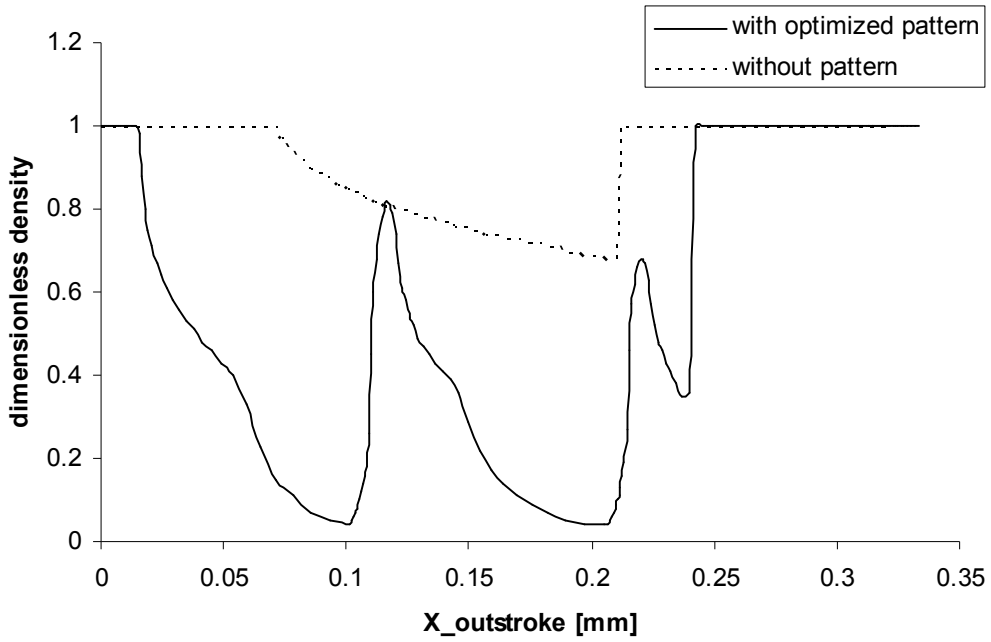

Figure 6.12: Dimensionless density distribution, outstroke, 0.005 m/s.

Figure 6.13 and Figure 6.14 show the film thickness distributions during outstroke and instroke respectively. As can be seen, during instroke the minimum film thickness, at the tooth tips, is substantially reduced from the conventional seal value. This is what reduces the Poiseuille flow in the outward direction and increases the net flow in the inward direction.

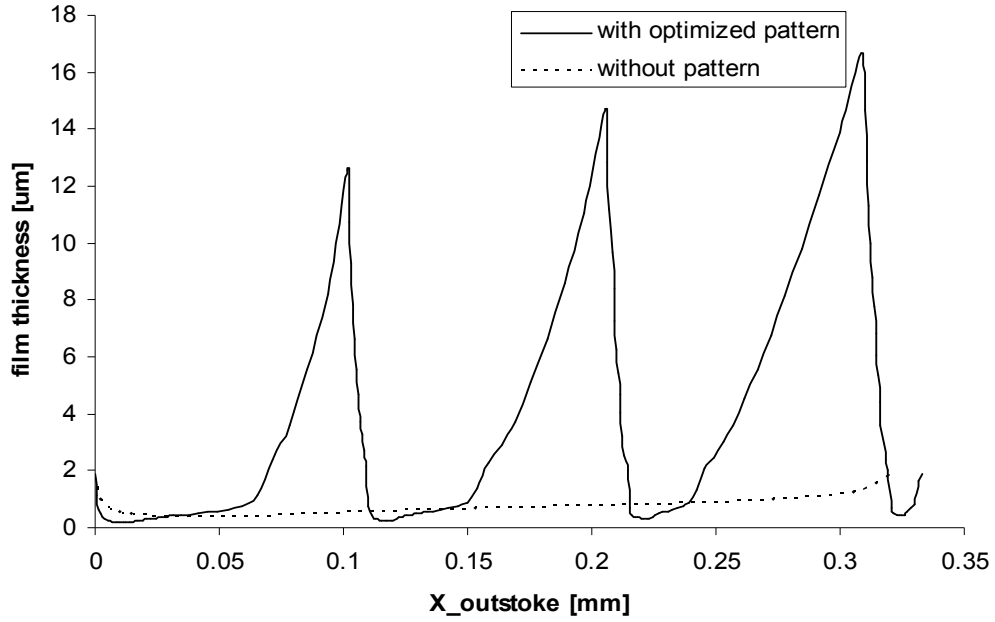

Figure 6.13: Film thickness distribution, outstroke, 0.005 m/s.

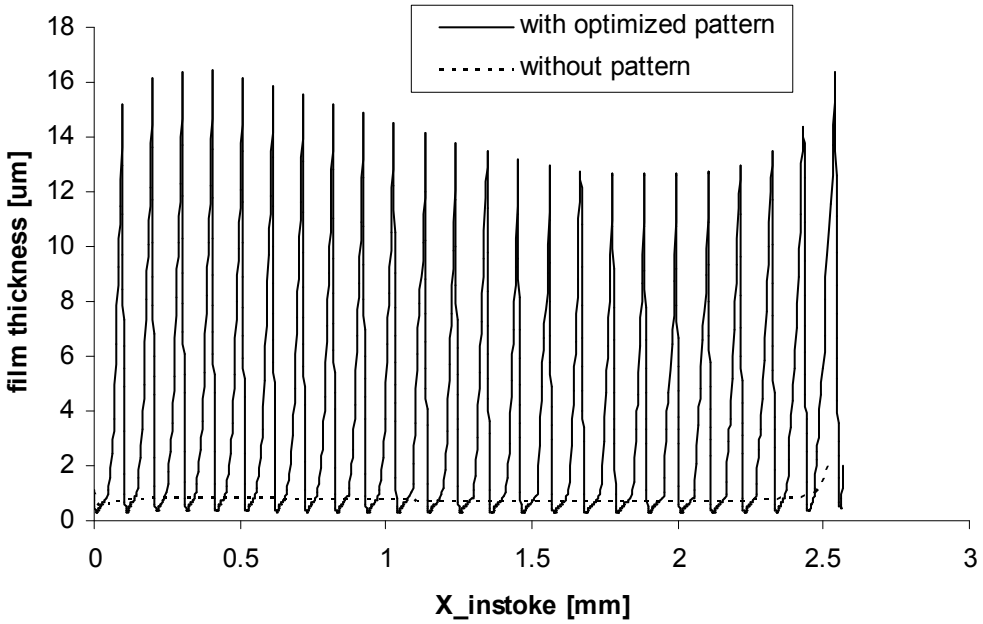

Figure 6.14: Film thickness distribution, instroke, 0.005 m/s.

6.5 Conclusions

The results of this study indicate that the inclusion of a micro-pattern on the sealing surface of a reciprocating rod seal can improve the sealing characteristics of the seal, without significantly affecting the friction force. However, it should be noted that the magnitude of the improvement will depend on the detailed surface characteristics (asperity size and density) of the seal. Furthermore, there may be practical problems that must be overcome, such as the effects of wear, incursion of contaminants, as well as manufacturing considerations.

CHAPTER 7

COMPARISON OF O-RING AND U-CUP HYDRAULIC SEALS

7.1 Introduction

This chapter describes the use of a simulation in the selection of the rod seal for a specific application, the hydraulic actuator of an orthosis. The initial choice was an O-ring seal. That and an alternative U-cup seal have been simulated using the model described before.

7.2 Seal Configuration

Figure 7.1 shows the cross-sections of the O-ring and U-cup seals of interest, which are assumed to be axisymmetric.

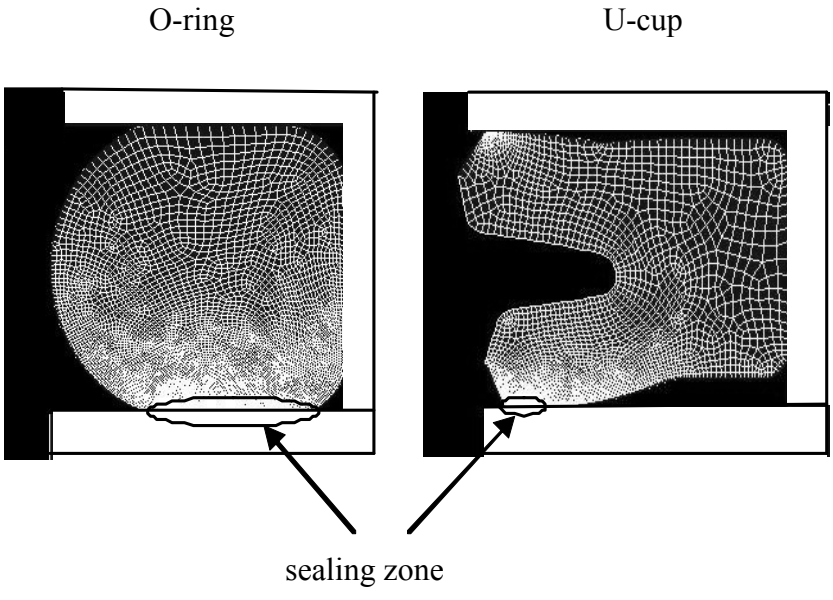

Figure 7.1: O-ring and U-cup Seals.

7.3 Results

As mentioned earlier, both an O-ring and a U-cup seal have been simulated. The material properties are the same as those in the analysis of the single lip seal, which are described in Table 3.1. Other relevant parameters are given in Table 7.1.

Table 7.1: Base Parameters of the O-ring and the U-cup seal.

sealed pressure - outstroke	0
sealed pressure - instroke	1 MPa-10 MPa
rod speed	0.01 m/s-0.1 m/s
rod diameter	3.5 mm
stroke length	200 mm
seal width – U-cup	1.0 mm
seal diameter – O-ring	1.0 mm

7.3.1 Leakage and Friction

Figure 7.2 shows the computed net leakage rate per cycle (outstroke plus instroke) for the rod speeds at the two extreme values of interest, 0.01 m/s and 0.1 m/s. At 0.01 m/s both seals leak, and with about twice as much leakage for the U-cup seal as for the O-ring for sealed pressure above 5MPa. At 0.1 m/s there is no leakage for the U-cup seal, while the O-ring continues to leak.

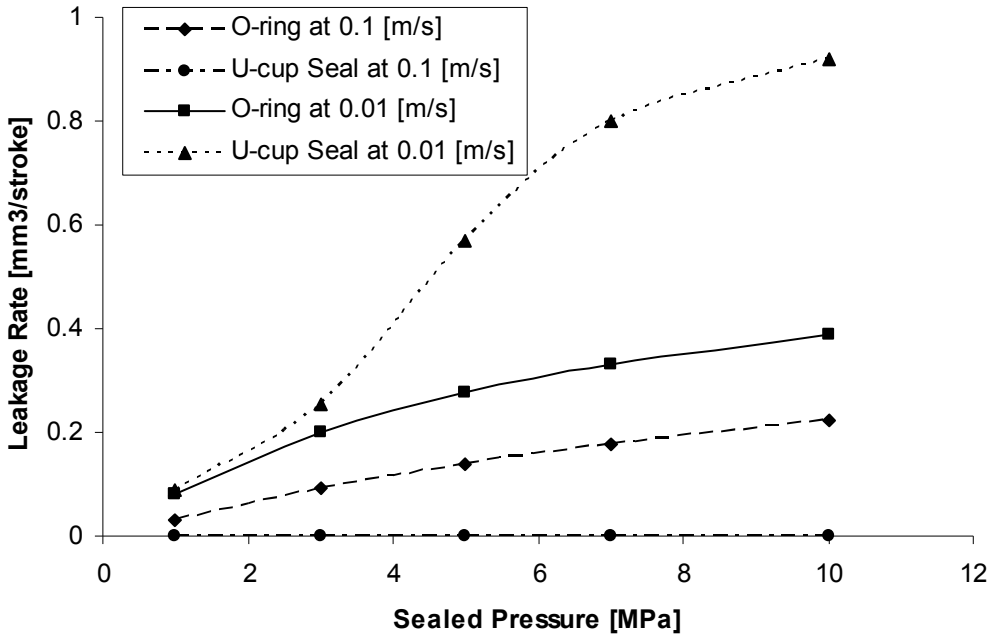

Figure 7.2: Leakage Rate vs. Sealed Pressure.

The leakage characteristics are further illustrated in Figure 7.3, which shows the fluid transport per stroke for both the outstroke and instroke, for the O-ring and U-cup seals at a sealed pressure of 10 MPa. To achieve zero net leakage, the instroke fluid transport must equal or exceed the outstroke transport. This does not occur for the O-ring seal; the outstroke transport always exceeds the instroke transport and the seal leaks. A similar result is found for the other sealed pressures of interest.

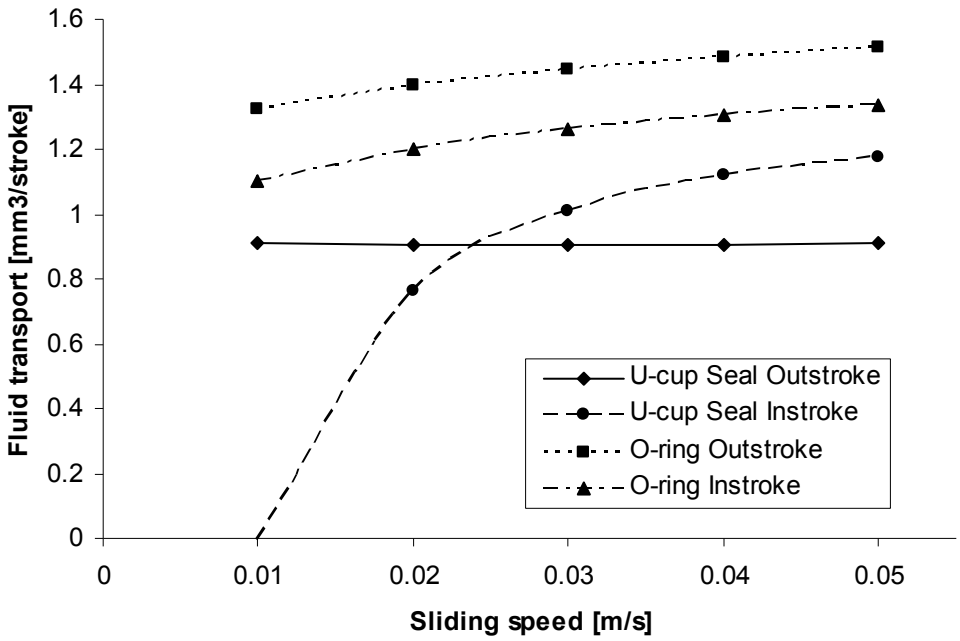

Figure 7.3: Fluid Transport vs. Rod Speed.

Conversely, the two fluid transport curves for the U-cup seal intersect, and for speeds above the critical speed of 0.023 m/s, the instroke transport exceeds the outstroke transport, indicating zero leakage. In general for the U-cup seal, if the rod speed exceeds a certain critical speed, the leakage will be zero (see Chapter 5). That critical speed is shown as a function of sealed pressure in Figure 7.4.

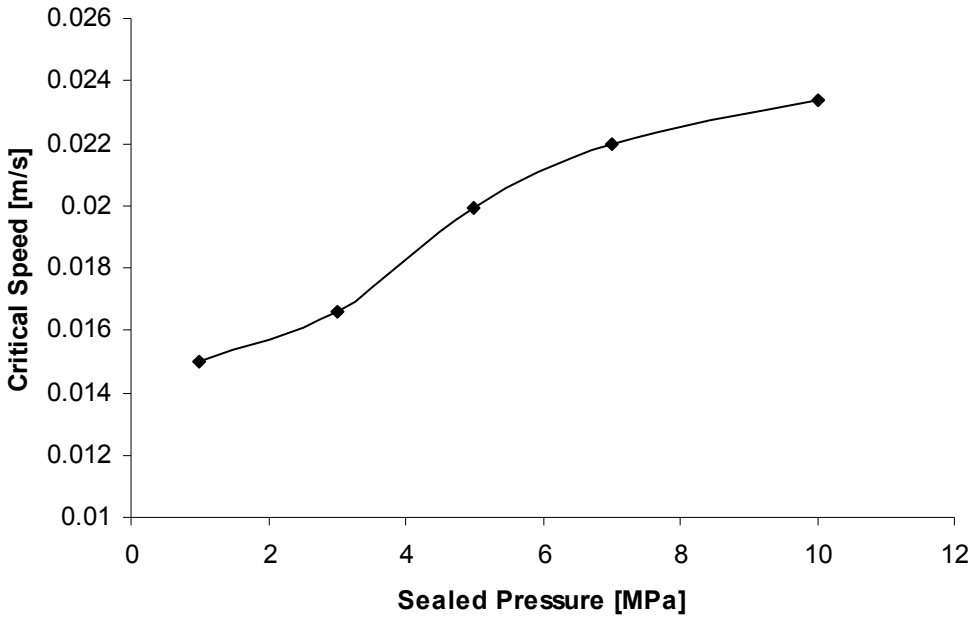

Figure 7.4: Critical Speed vs. Sealed Pressure, U-cup Seal.

From Figure 7.4 it is seen that over almost the entire operating range of the U-cup seal (except at the lowest speeds) there will be zero net leakage. It should be noted that there is no comparable critical speed plot for the O-ring seal, since that seal always leaks. Thus, from a leakage point of view, the U-cup seal is superior to the O-ring.

The friction force is also of concern in this application. Figure 7.5 shows the average friction force (averaged over the outstroke and instroke) as a function of sealed pressure.

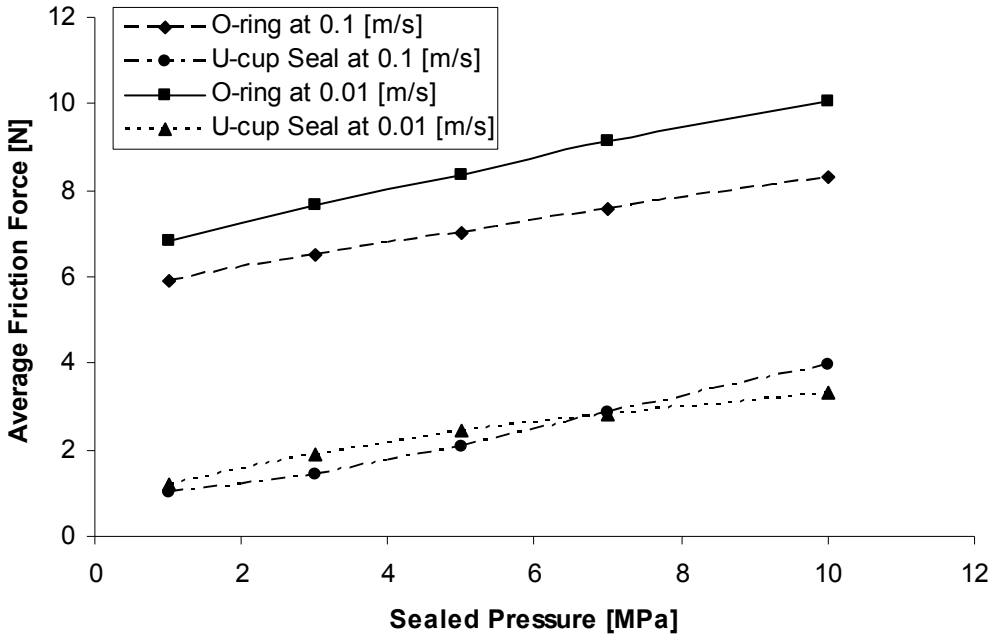

Figure 7.5: Average Friction Force vs. Sealed Pressure.

It is seen that the friction force for the O-ring greatly exceeds that for the U-cup. Thus from the friction point of view, the U-cup seal is again superior to the O-ring.

7.3.2 Details of Sealing

To understand the above leakage and friction results, it is useful to examine the details of the sealing zone. Figure 7.6 and Figure 7.7 show the film thickness distributions for the O-ring and U-cup seals at a sealed pressure of 10 MPa and rod speed of 0.1 m/s.

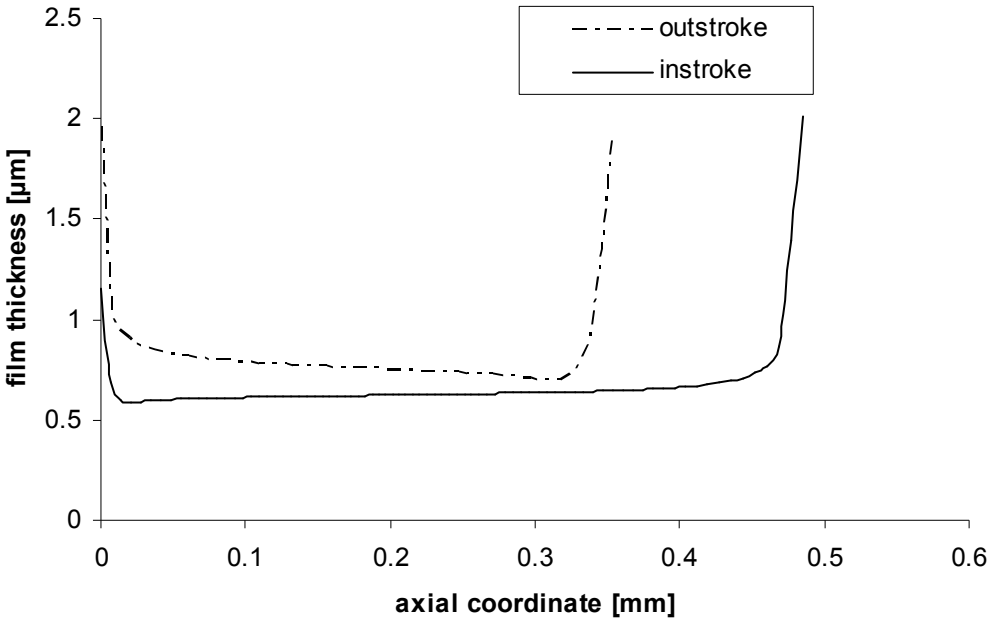

Figure 7.6: Film Thickness Distribution, O-ring, 10 MPa, 0.1 m/s.

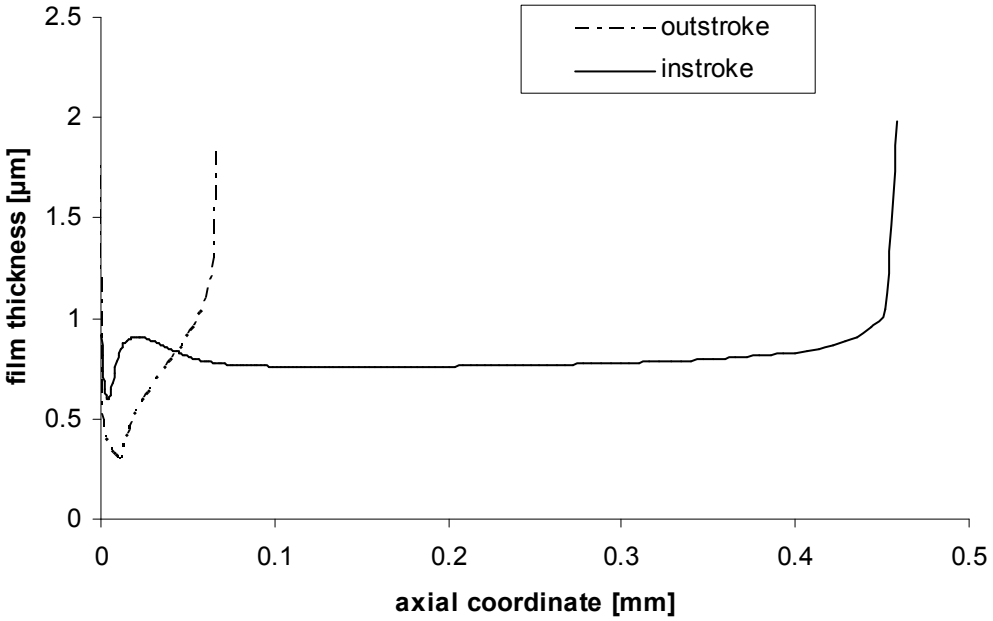

Figure 7.7: Film Thickness Distribution, U-cup, 10 MPa, 0.1 m/s.

For both seals the film thickness is less than three times the RMS roughness, indicating mixed lubrication in the sealing zone. For the O-ring the film thickness is lower during instroke than during outstroke, at proportional locations along the sealing zone. For the U-cup seal the opposite is true over half of the zone. This latter condition is more favorable for the prevention of leakage since a thicker film during the instroke allows a larger amount of fluid to be drawn back into the cylinder than is drawn out during the outstroke.

It is also seen from Figure 7.6 and Figure 7.7 that the length of the sealing zone is larger during the instroke than during the outstroke (due to the increased sealed pressure) for both seals. However, while the instroke lengths are about the same for both seals, the outstroke length is much shorter for the U-cup seal than for the O-ring. This has implications for the friction force, as discussed below.

The friction force on the rod is equal to the shear stress on the rod surface integrated over the length of the sealing zone. That shear stress is shown in Figure 7.8 and Figure 7.9 for both seals. It is seen that the magnitude of the shear stress for the O-ring exceeds that for the U-cup seal, during the instroke. That, together with the fact that the outstroke sealing zone length for the O-ring substantially exceeds that for the U-cup seal, as discussed above, is the reason why the average friction force is higher for the O-ring than for the U-cup seal, as shown in Figure 7.5 and discussed earlier.

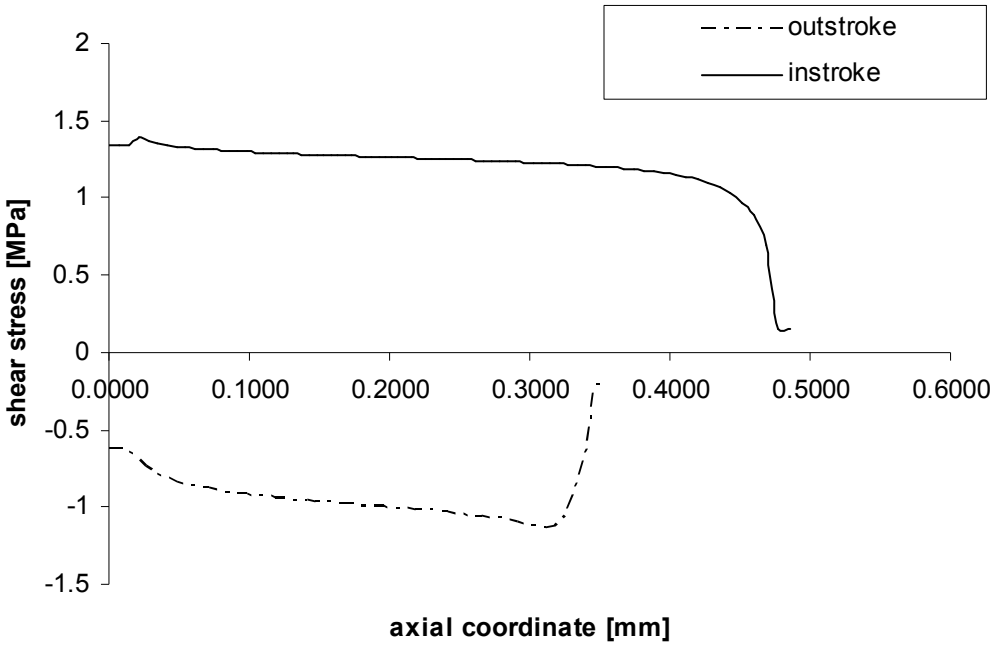

Figure 7.8: Shear Stress Distribution, O-ring, 10 MPa, 0.1 m/s.

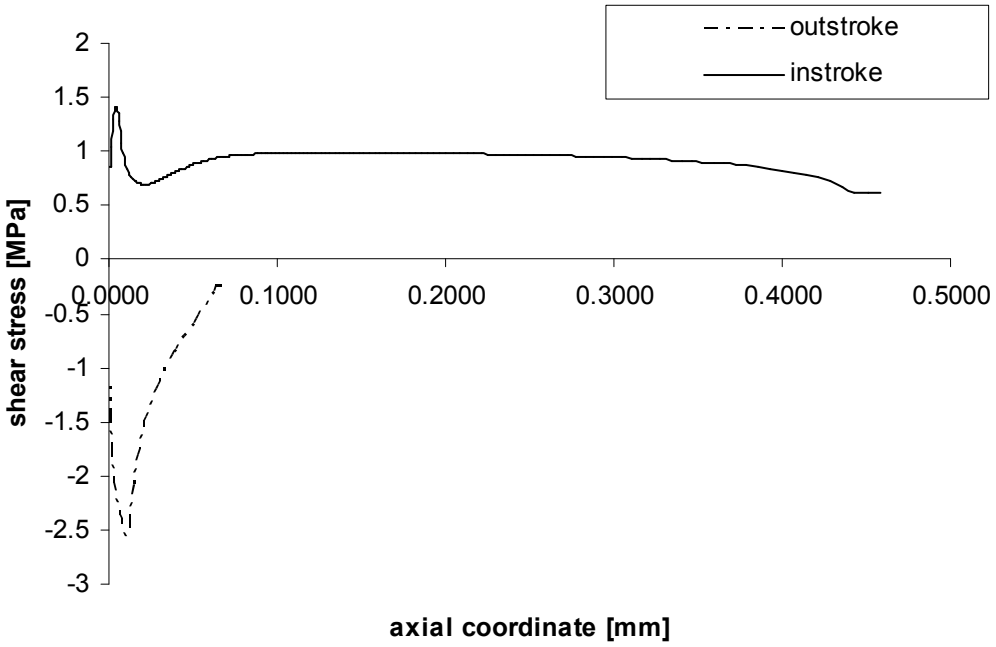

Figure 7.9: Shear Stress Distribution, U-cup, 10 MPa, 0.1 m/s.

Figure 7.10 and Figure 7.11 show the various pressure distributions in the sealing zone during the outstroke for the O-ring and U-cup seals.

During the outstroke, the static contact pressure distribution is very symmetric for the O-ring, but contains a peak closer to the liquid side of the seal for the U-cup seal. The latter shape is characteristic of successful rod seals

For both seals the fluid pressure goes to zero over portions of the sealing zone, indicating cavitation. However, the cavitated fraction of the sealing zone is much larger for the U-cup seal than for the O-ring. The more cavitation during the outstroke, the better, since cavitation restricts the flow of fluid through the sealing zone and inhibits leakage.

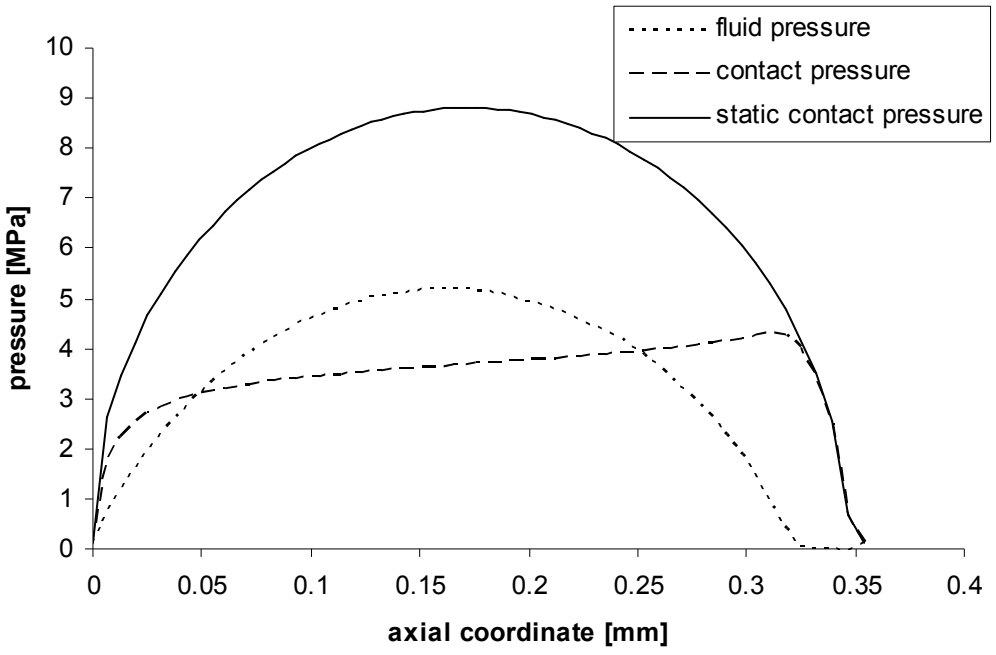

Figure 7.10: Pressure Distributions, Outstroke, O-ring, 10 MPa, 0.1 m/s.

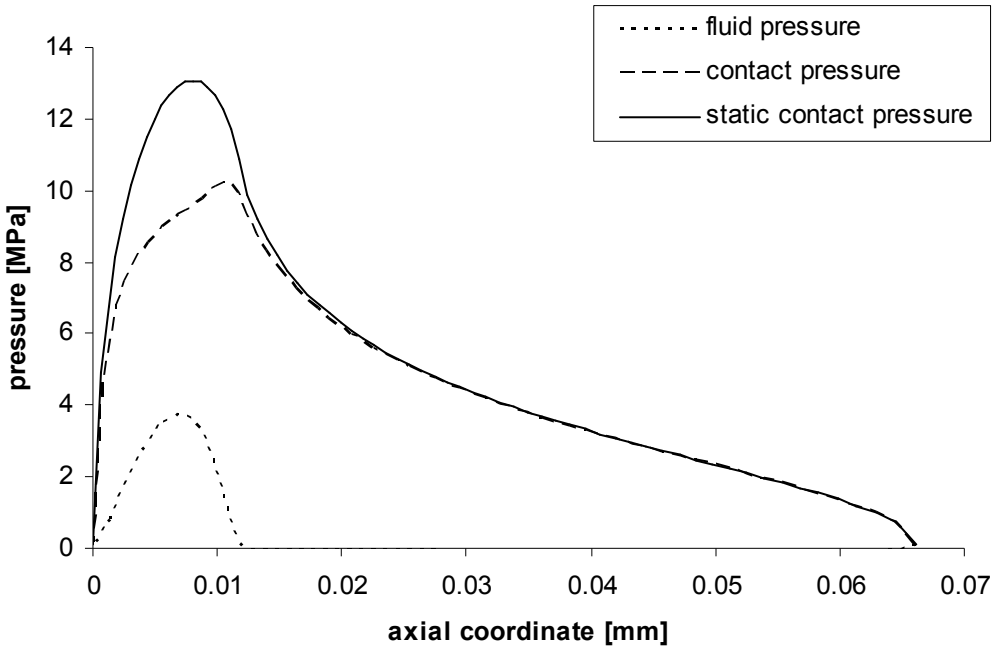

Figure 7.11: Pressure Distributions, Outstroke, U-cup, 10 MPa, 0.1 m/s.

The pressure distributions during the instroke are shown in Figure 7.12 and Figure 7.13. From these it is seen that all of the pressure distributions are considerably altered, primarily due to the increased sealed pressure. It is also seen that the cavitation has been eliminated for both seals.

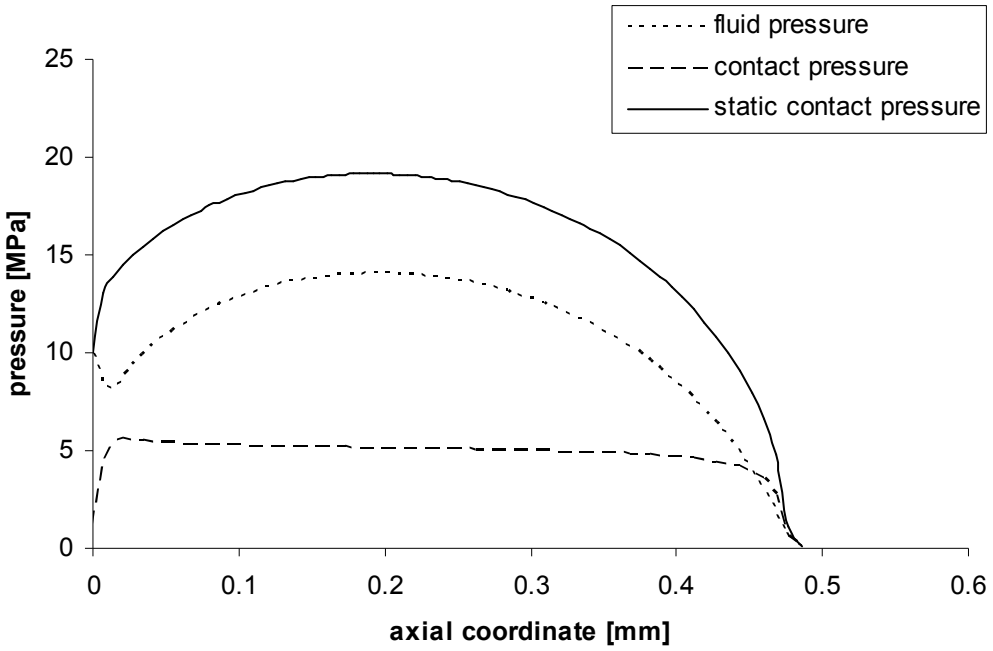

Figure 7.12: Pressure Distributions, Instroke, O-ring, 10 MPa, 0.1 m/s.

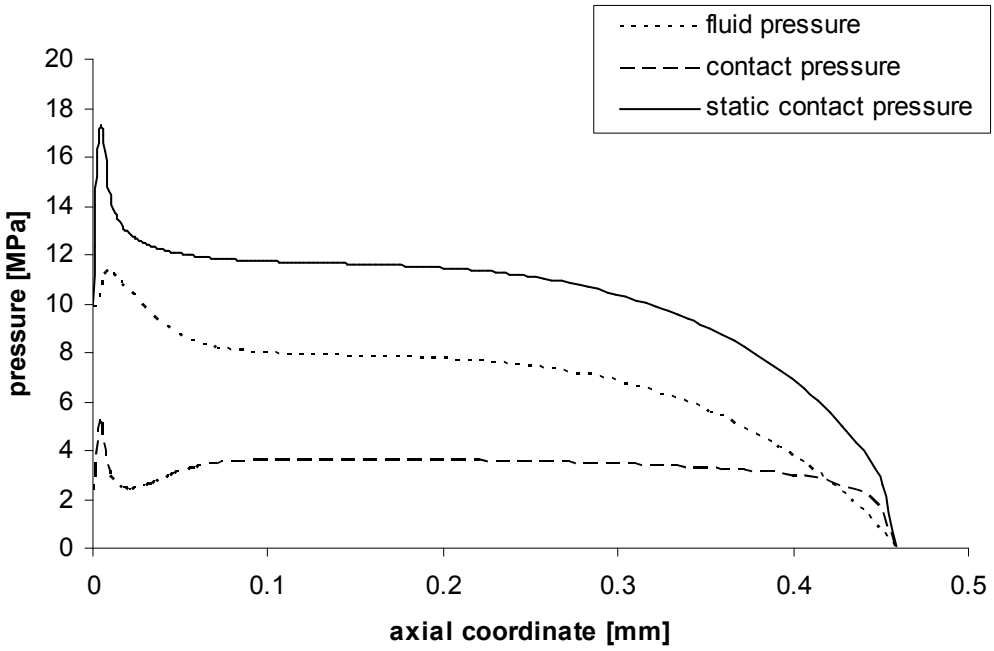

Figure 7.13: Pressure Distributions, Instroke, U-cup, 10 MPa, 0.1 m/s.

7.4 Conclusions

This study demonstrates the usefulness of simulation in the selection of reciprocating seals. Numerical predictions show that the performance of the original choice of an O-ring is inferior to that of a U-cup seal. The O-ring seal will leak over the entire desired operating range, while the U-cup will seal over 94% of the speed range at the highest sealed pressure. Furthermore the friction force of the O-ring will be more than twice that of the U-cup seal.

CHAPTER 8

CONCLUSIONS

Previous experiments have shown the neglect of roughness and the assumption of full film lubrication of the previous theoretical models to be unrealistic and have led to erroneous predictions. In the present research, an elastohydrodynamic model that takes account of both mixed lubrication and surface roughness effects is successfully developed. This model is capable of predicting the key seal performance characteristics, especially seal leakage and friction, and serve as design tools. The critical roughness and critical speed, the most important measurements of seal performance, have been defined and determined using this model. Also as this model has been developed, the basic physics of seal operation has been clarified, which stimulates the development of innovative seal concepts, such as seals with engineered sealing surfaces.

The results of this study indicate that the rod seal operates with mixed lubrication in the sealing zone, and seal roughness plays an important role in determining its behavior. There is a critical seal roughness, below which the seal will be non-leaking, above which the seal will leak. A larger film thickness during instroke compared to that during outstroke promotes non-leaking. Cavitation during outstroke also promotes non-leaking.

The results of this study also show that the behavior of a reciprocating hydraulic rod seal with a double lip or two seals in tandem arrangement can be very different from that of a similar seal with a single lip. For the double lip seal, the secondary lip can

strongly affect the behavior of the primary lip by producing an elevated pressure in the interlip region. The same seal characteristics that promote effective sealing in a single lip seal and, in addition structural decoupling of multiple lips, are found to promote effective sealing in a multiple lip seal.

The model reveals seal leakage is strongly dependent on the rod speed, the sealed pressure and the seal roughness, for a given seal design and stroke length. There exists a critical rod speed, below which the seal will leak, while above which there will be zero net leakage. The critical rod speed depends on the seal design, the sealed pressure and the seal roughness. Comparison of a double lip U-cup seal with a similar size step seal indicates the step seal has a lower critical rod speed.

The model is validated through comparisons of model predictions with experimental measurements and observations by industry partners. The results have shown the predicted leakage and friction force for various seal and operation conditions are consistent with the measurements.

The results of this study indicate that the inclusion of a micro-pattern on the sealing surface of a reciprocating rod seal can improve the sealing characteristics of the seal, without significantly affecting the friction force. However, it should be noted that the magnitude of the improvement will depend on the detailed surface characteristics (asperity size and density) of the seal. Furthermore, there may be practically problems that must be overcome, such as the effects of wear, incursion of contaminants, as well as manufacturing considerations.

This study also demonstrates the selection of the rod seal for a specific application using this analytical model. The best design can be picked up before a prototype being built.

In summary, this analytical model provides an effective tool for the designer to predict and optimize the performance of a seal design under various operating conditions. However, it is still necessary to combine this analytical model with experimental studies to take into account the real world factors in practice.

REFERENCES

1. Claus, R. G., "Development of a High Performance, Heavy Duty Piston Seal," Proc. 49th National Conference on Fluid Power, NFPA, 2002, 383-389.
2. Peng, S., Sun, S. and Albertson, K, "FEA-Assisted Design of Low-Friction U-Cup as Spool Valve Seals," Proc. 47th National Conference on Fluid Power, NFPA, 175-182.
3. Naderi, A., Albertson, K. and Peng, S., "Finite Element Analysis of a Hydraulic Seal: BS U-Cup," Proc. 46th National Conference on Fluid Power, NFPA, 1994, 99-105.
4. Weiss, H., "New Generation of Hydraulic Seals Supports Progress for Hydraulic Cylinders," Proc. 47th National Conference on Fluid Power, NFPA, 1996, 153-163.
5. Field, G. J., and Nau, B. S., "Film Thickness and Friction Measurements during Reciprocation of a Rectangular Section Rubber Seal Ring," Proc. 6th BHRA International Conference on Fluid Sealing, 1973.
6. Kawahara, Y., Ohtake, Y., and Hirabayashi, H., "Oil film formation of oil seals for reciprocating motion", Proceedings of the 9th International Conference on Fluid sealing, 1981, 73–85 (BHRA).
7. Kanters, A. F. C. and Visscher, M., "Lubrication of Reciprocating Seals: Experiments on the Influence of Surface Roughness on Friction and Leakage," Proc. 15th Leeds-Lyon Symposium on Tribology, 1988, 69-77.

8. Müller, H. K. and Nau, B. S., “Fluid Sealing Technology”, Marcel Dekker, New York, 1998.
9. Nikas, G. K., “Elastohydrodynamics and Mechanics of Rectangular Elastomeric Seals for Reciprocating Piston Rods,” J. of Tribology, 2003, 125, 60-69.
10. Nikas, G. K, “Transient Elastohydrodynamic Lubrication of Rectangular Elastomeric Seals for Linear Hydraulic Actuators,” J. of Engineering Tribology, 2003, 217, 461-473.
11. Nikas, G. K. and Sayles, R. S., “Nonlinear Elasticity of Rectangular Elastomeric Seals and its Effect on Elastohydrodynamic Numerical Analysis,” Tribology International, 2004, 37, 651-660.
12. Nikas, G. K., “Eighty years of research on hydraulic reciprocating seals: review of tribological studies and related topics since the 1930s,” Proceedings of the Institution of Mechanical Engineers, Part J: Journal of Engineering Tribology, 2010, 214(1), 1-23.
13. Ishiwata, H. and Kambayashi, H., “A study of oil seal for reciprocating motion,” Proc. 2nd BHRA International Conference on Fluid Sealing, 1964, B3.
14. White, C. M. and Denny, D. F. “The sealing mechanism of flexible packings”, Scientific and Technical Memorandum No. 3/47, UK Ministry of Supply, 1947.
15. Müller, H. K., “Leakage and friction of flexible packings at reciprocating motion with special consideration of hydrodynamic film formation”, Proceedings of the 2nd International Conference on Fluid sealing, 1964, 13–28 (BHRA).

16. Field, G. J. and Nau, B. S., “An experimental study of reciprocating rubber seals”, Proceedings of the IMechE Symposium on Elastohydrodynamic Lubrication, Leeds, UK, 1972, 29–36.
17. Hirano, F. and Kaneta, M., “Theoretical Investigation of Friction and Sealing Characteristics of Flexible Seals for Reciprocating Motion,” Proc. 5th BHRA International Conference on Fluid Sealing, 1971, G2.
18. Field, G. J., “The elastohydrodynamic lubrication of rectangular section rubber seals under conditions of reciprocating motion”, PhD Thesis, City University London, England, 1973.
19. Iwanami, S. and Tikamori, N., “Oil leakage from an O-ring packing”, Proceedings of the 1st International Conference on Fluid sealing, 1961, paper B2 (BHRA).
20. Kaneta, M., “Sealing characteristics of double reciprocating seals”, J. Jpn. Soc. Lubr. Eng., 1985, 30(3), 194–200.
21. Kambayashi, H. and Ishiwata, H., “A study of oil seals for reciprocating motion”, Proceedings of the 2nd Inter-national Conference on Fluid sealing, 1964, 29–40 (BHRA).
22. Kanters, A. F. C., “On the calculation of leakage and friction of reciprocating elastomeric seals”, PhD Thesis, Eindhoven University of Technology, the Netherlands, 1990.
23. Visscher, M. and Kanters, A. F. C., “Literature review and discussion on measurements of leakage, lubricant film thickness and friction of reciprocating elastomeric seals”, STLE Lubr. Eng., 1990, 46(12), 785–791.

24. Visscher, M., “The measurement of the film thickness and roughness deformation of lubricated elastomers”, PhD Thesis, Eindhoven University of Technology, the Netherlands, 1992.
25. Denny, D. F., “The friction of rubber sealing rings”, British Hydromechanics Research Association, Res. report No. 458, Harlow, UK, 1953.
26. Cheyney, L. E., Mueller, W. J., and Duval, R. E., “Frictional characteristics of O-rings with a typical hydraulic fluid”, Trans. ASME, 1950, 72(4), 291–297.
27. Lawrie, J. M. and O’Donoghue, J. P., “The mechanism of lubrication in a reciprocating seal”, Proceedings of the 2nd International Conference on Fluid sealing, 1964, 69–80 (BHRA).
28. Gawrys and Kollek, “The effect of operation conditions on the design of seals for reciprocating motion”, Proceedings of the 10th International Conference on Fluid sealing, 1984, 285–294 (BHRA).
29. Dowson, D. and Swales, P. D., “The development of elastohydrodynamic conditions in a reciprocating seal”, Proceedings of the 4th International Conference on Fluid sealing, 1969, 2–10 (BHRA).
30. Johannesson, H., “Calculation of the pressure distribution in an O-ring seal contact”, Proceedings of the 5th Leeds–Lyon Symposium on Tribology, 1978, 379–387.
31. May, E. M., “Pressure drop across a packing”, Appl. Hyd., 1957, 10(5), 110–114.
32. Olssen, E., “Friction forces and oil leakage of O-rings on axially moving shafts”, PhD Thesis, Chalmers University of Technology, Sweden, 1972.

33. Molari, P. G., “Stresses in O-ring gaskets”, Proceedings of the 6th International Conference on Fluid sealing, 1973, 15–31 (BHRA).
34. Austin, R. M., Flitney, R. K., and Nau, B. S., “Con-tact stress, friction and the lubricant film of hydraulic cylinder seals”, In Proceedings of the 8th International Conference on Fluid sealing, 1978, 11–20 (BHRA).
35. Kawahara, Y., Ohtake, Y., and Hirabayashi, H., “Oil film formation of oil seals for reciprocating motion”, Proceedings of the 9th International Conference on Fluid sealing, 1981, 73–85 (BHRA).
36. Strozzi, A., “Static stresses in an unpressurized, rounded, rectangular, elastomeric seal”, ASLE Trans., 1986, 29(4), 558–564.
37. Johannesson, H. L. and Kassfeldt, E., “Computer aided hydraulic cylinder seal design”, Proceedings of the 11th International Conference on Fluid sealing, 1987, 314–329 (BHRA).
38. Lindgren, H., “Pressure distribution in scraper ring contacts”, Wear, 1987, 115(1–2), 31–40.
39. Prati, E. and Strozzi, A., “A study on the elastohydrodynamic problem in rectangular, elastomeric seals”, ASME J. Tribol., 1984, 106(4), 505–512.
40. Blok, H. and Koens, H. J., “The breathing film between a flexible seal and a reciprocating rod”, Proc. Instn Mech. Engrs, 1965/66, 180(part 3B), 221–223.
41. Roberts, A. D. and Tabor, D., “Fluid film lubrication of rubber – an interferometric study”, Wear, 1968, 11(2), 163–166.

42. Kanzaki, Y., Kawahara, Y., and Kaneta, M., “Optical interferometric observations of oil film behaviour in reciprocating rubber seals”, Trans. Jpn. Soc. Mech. Eng. C, 1996, 62(600), 3229–3236.
43. Kanzaki, Y., Kawahara, Y., and Kaneta, M., “Oil film behaviour and friction characteristics in reciprocating rubber seals. Part 1: single contact”, Proceedings of the 15th International Conference on Fluid sealing, 1997, 79–95 (BHRA).
44. Kaneta, M., Todoroki, H., Nishikawa, H., Kanzaki, Y., and Kawahara, Y., “Tribology of flexible seals for reciprocating motion”, ASME J. Tribol., 2000, 122(4), 787–795.
45. Rana, A. S., “A tribological study of elastomeric reciprocating seals for hydraulic actuators”, PhD Thesis, Imperial College London, Mechanical Engineering Department, 2005.
46. Schrader, K. Beitrage, “zur klaerung des abdichtvor-ganges gummielastischer abdichtungen axial verschieb-barer hydrostatischer bauteile”, PhD Thesis, Dresden University of Technology, Germany, 1978.
47. Rana, A., Sayles, R. S., Nikas, G. K., and Jalisi, I., “An experimental technique for investigating the sealing principles of reciprocating elastomeric seals for use in linear hydraulic actuator assemblies”, Proceedings of the 2nd World Tribology Congress, Vienna, Austria, 2001.
48. Rana, A. S. and Sayles, R. S., “An experimental study on the friction behaviour of aircraft hydraulic actuator elastomeric reciprocating seals”, Proceedings of the 31st Leeds–Lyon Symposium on Tribology, 2004.

49. Chadwick, P., “Thermo-mechanics of rubber like materials”, Philos. Trans. R. Soc. Lond. A, 1974, 276(1260), 371–403.
50. Price, C., “Thermodynamics of rubber elasticity”, Proc. R. Soc. Lond. A., 1976, 351(1666), 331–350.
51. Chadwick, P. and Creasy, C. F. M., “Modified entropic elasticity of rubber like materials”, J. Mech. Phys. Solids, 1984, 32(5), 337–357.
52. Ogden, R. W., “Large deformation isotropic elasticity – on the correlation of theory and experiment for incompressible rubberlike solids”, Proc. R. Soc. Lond. A., 1972, 326(1567), 565–584.
53. Ogden, R. W., “Elastic deformations of rubberlike solids”, Mechanics of solids, 1982, the Rodney Hill 60th anniversary volume, 499–537.
54. Ogden, R. W., “Non-linear elastic deformations”, Dover Publications, New York, USA, 1997.
55. Treloar, L. R. G, “The mechanics of rubber elasticity”. Proc. R. Soc. Lond. A., 1976, 351(1666), 301–330.
56. Mooney, M., “A theory of large elastic deformation”, Appl. Phys., 1940, 11(9), 582–592.
57. Rivlin, R. S., “Large elastic deformations of isotropic materials. IV. Further developments of the general theory”, Philos. Trans. R. Soc. Lond. A., 1948, 241(835), 379–397.
58. Zhang, S. W., “State-of-the-art of polymer tribology”, Tribol. Int., 1998, 31(1–3), 49–60.

59. Duhring, B. and Iversen, G., “The application of plastics in dynamic seals”, Proc. IMechE, Part J: J. Engineering Tribology, 1999, 213(J3), 227–237.
60. Li, W. and Mays, S., “Analysis of PTFE material in rotary seals”, Proceedings of the 17th International Conference on Fluid sealing, 2003, 157–165 (BHRA).
61. Lee, N. J. and Jang, J., “The effect of fibre content gradient on the mechanical properties of glass-fibre-mat/polypropylene composites”, Compos. Sci. Technol., 2000, 60(2), 209–217.
62. Ganghoffer, J.F., Brillard, A., and De-Borst, R., “Description of the mechanical behaviour of micropolar adhesives”, Math. Comput. Model., 1998, 27(7), 23–49.
63. Caddock, B. D. and Evans, K. E., “Negative Poisson ratios and strain-dependent mechanical properties in arterial prostheses”, Biomaterials, 1995, 16(14), 1109–1115.
64. Kanters, A. F. C., Verest, J. F. M. And Visscher, M., “On Reciprocating Elastomeric Seals: Calculation of Film Thicknesses Using the Inverse Hydrodynamic Lubrication Theory”, Tribology Transactions, 1990, 33, 301-306.
65. Blok, H., “Inverse problems in hydrodynamic lubrication and design directives for lubricated flexible surfaces”, Proceedings of the International Symposium on Lubrication and Wear, Houston, Texas, USA, 1963, 7–79.
66. Gohar, R., “Elastohydrodynamics”, 2nd edition, Imperial College Press, London, UK, 2001.
67. Ruskell, L. E. C., “Reynolds equation and elastohydrodynamic lubrication in metal seals”, Proc. R. Soc. Lond. A, 1976, 349(1658), 383–396.

68. Hirano, F. and Kaneta, M., “Dynamic behaviour of flexible seals for reciprocating motion”, Proceedings of the 4th International Conference on Fluid sealing, 1969, 11–20 (BHRA).
69. Theyse, F. H., “The inverse hydrodynamic theory and its application in the design of controlled leakage seals between moving parts”, Proceedings of the 3rd International Conference on Fluid sealing, 1967, 17–32 (BHRA).
70. Nikas, G. K. and Sayles, R. S., “Study of leakage and friction of flexible seals for steady motion via a numerical approximation method”, Tribol. Int., 2006, 39(9), 921–936.
71. Field, G. J. and Nau, B. S., “A theoretical study of the elastohydrodynamic lubrication of reciprocating rubber seals”, ASLE Trans., 1975, 18(1), 48–54.
72. Ruskell, L. E. C., “A Rapidly Converging Theoretical Solution to the Elastohydrodynamic Problem for Rectangular Rubber Seals,” J. Mechanical Engineering Science, 1980, 22, 9-16.
73. Yang, Y. and Hughes, W. F., “An Elastohydrodynamic Analysis of Preloaded Sliding Seals,” ASLE Transactions, 1983, 27, 197-202.
74. Nikas, G. K. and Sayles, R. S., “Nonlinear elasticity of rectangular elastomeric seals and its effect on elastohydrodynamic numerical analysis”, Sealing Technology, 2005, 2005(3), 6–11.
75. Nikas, G. K. and Sayles, R. S., “Computational model of tandem rectangular elastomeric seals for reciprocating motion”, Tribol. Int., 2006, 39(7), 622–634.
76. Nikas, G. K., “Theoretical study of solid back-up rings for elastomeric seals in hydraulic actuators”, Tribol. Int., 2004, 37(9), 689–699.

77. Payvar, P. and Salant, R.F., "A Computational Method for Cavitation in a Wavy Mechanical Seal," Journal of Tribology-Transactions of the ASME, 1992, 114, 119-204.

78. Patir, N. and Cheng, H. S., "An Average Flow Model for Determining Effects of Three-Dimensional Roughness on Partial Hydrodynamic Lubrication," J. of Lubrication Technology, 1978, 100, 12-17.

79. Patir, N. and Cheng, H. S., "Application of Average Flow Model to Lubrication between Rough Sliding Surfaces," J. of Lubrication Technology, 1979, 101, 220-229.

80. Patankar, S.V., "Numerical heat transfer and fluid flow", Taylor & Francis, PA, USA, 1980.

81. Greenwood, J. A. and Williamson, J. B. P., "Contact of Nominally Flat Rough Surfaces," Proc. Royal Society (London), 1966, A295, 300-319.

82. Streator, J. L., "A Model of Mixed Lubrication with Capillary Effects," Proc. 15th Leeds-Lyon Symposium on Tribology, 2001, 121-128.

83. Bhushan, B., "Principles and Applications of Tribology", Wiley, New York, 1999.

84. Stachowiak, G.W. and Batchelor, A.W., "Engineering tribology", third edition, Elsevier Butterworth-Heinemann, USA, 2005.

85. Salant, R.F., Maser, N. and Yang, B. "Numerical model of a reciprocating hydraulic rod seal", Journal of Tribology-Transactions of the ASME, 2007, 129(1), 91-97.

86. Yang, B. and Salant, R.F. "A numerical model of a reciprocating rod seal with a secondary lip", Tribology Transactions, 2008, 51(2), 119-127.

87. Yang, B. and Salant, R.F. “Numerical model of a tandem reciprocating hydraulic rod seal”, Journal of Tribology-Transactions of the ASME, 2008, 130(3), 032201.

88. Yang, B. and Salant, R.F. “Numerical analysis compares the lubrication of U seal and step seal”, Sealing Technology, 2009, 2009(3), 7-11.

89. Yang, B. and Salant, R.F. “Soft EHL Simulations of U-Cup and Step Hydraulic Rod Seals”, Journal of Tribology-Transactions of the ASME, 2009, 131(2), 021501.

VITA

Bo Yang

Bo Yang was born in Qian County, Shaanxi Province, China in 1981. He received his BS and MS from Department of Thermal Engineering, Tsinghua University. As a master student, he worked in Tsinghua-BP Clean Energy Research Center on clean coal technology. His master's thesis dealt with numerical modeling of coal fired power plant thermal systems. Bo entered the Department of Mechanical Engineering in 2005 as a Ph.D student working with Prof. Richard F. Salant. His major research interest is the development of realistic numerical models of elastomer seals based on elastohydrodynamic lubrication theory.